Alma Mater Studiorum - Università di Bologna

School of Science
Department of Physics and Astronomy
Master Degree Programme in Astrophysics and Cosmology

A comparative study of companion galaxies around strong galaxy-galaxy lenses and non-lens galaxies: implications for dark matter halo masses

Graduation Thesis

July 17, 2026

Presented by:
Marco Callegari

Supervisor:
Prof. Robert Benton Metcalf

Academic year 2025-2026

Graduation date I

Abstract

Strong galaxy-galaxy lensing is a powerful tool that, mapping the distribution of matter in the universe, is used to address specific questions in cosmology and astrophysics. More specifically, the thesis investigates and quantifies possible differences in the local environments of lens and non-lens galaxies. This environmental information is then translated, within the HOD framework, into a mass ratio between the dark matter halos hosting these galaxies.

Contents

Chapter 1

Introduction to gravitational lensing

1.1 History

The deflection of light due to to gravity was long suspected, even before General Relativity described it quantitatively. This section is dedicated to a brief review of the history that led to the detection and characterisation of the gravitational lensing.

1.1.1 Theoretical predictions

Gravitational light deflection in the Newtonian context

In the context of the Newtonian theory of gravitation, several physicists thought that light could be influenced by gravity.

In 1784 John Mitchell considered that light rays, moving in the field of a spherical object with mass M, would be subjected to a deflection. The calculations of this deflection angle, performed by Cavendish and Soldner, led to the following formula

$$\hat{\alpha}_N = \frac{2GM}{c^2 \xi} \tag{1.1}$$

where G is universal gravitational constant ($G = 6.67 \times 10^{-11}\ Nm^{-2}kg^{-2}$), c is the speed of light ($c = 299792\ km\ s^{-1}$) and ξ is the impact parameter of the incoming rays. As a consequence, measuring how the speed of light would change due to a star's gravitational field could give an estimate of the star's mass. Therefore, from the beginning it was clear that this effect could be used to study the universe from a new perspective. Using the previous formula we can predict the deflection angle of light rays propagating near the surface of the Sun (figure 1.1): considering the Sun's radius ($\sim 695700\ km$) and mass ($\sim 1.989 \times 10^{30}\ kg$) the deflection angle is about 0.875 arcseconds.

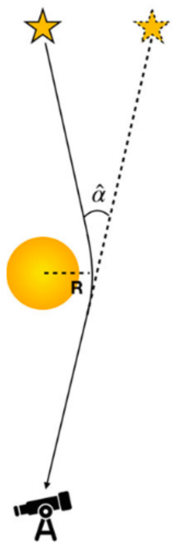

Figure 1.1: Qualitative representation of light deflection due to the Sun's gravity. As a consequence, we observe an apparent image of the source. [Meneghetti (2021)]

In 1795 Pierre-Simon Laplace introduced the idea that light could be trapped by the gravitational force of a really heavy body. The escape velocity from a spherical body, with a mass M and a radius R, would be equal to the speed of light. Now we know that this happens when R matches the Schwarzschild radius $R_S = \frac{2GM}{C^2}$. Instead, objects with $R < R_S$ are nowadays called black holes.

These results, based on the principles of classical mechanics, were obtained with the assumption that light could be treated as a massive particle and therefore they were incorrect.

Gravitational light deflection in the Relativistic context

The turning point, in the interpretation of this phenomenon, is represented by the formulation of the General Relativity by Albert Einstein in 1915. The effects of gravity are considered indistinguishable from those of an acceleration, he also enunciated the principle of equivalence that sustained the coincidence between inertial and gravitational mass. Therefore, assuming the speed of light is constant, light must be influenced by gravity; more specifically gravity should be able to bend the light trajectory. Using this new theory, which considers gravity as assemblies of mass and energy capable of curving the space-time , the computation of the deflection angle gives a different result

$$\hat{\alpha} = \frac{4GM}{c^2\xi} \tag{1.2}$$

which is twice the Newtonian prediction. Therefore, a light ray would be deflected by about 1.75 arcsecond due to the Sun' gravity.

These theoretical results needed to be tested and the idea was to take advantage of a total solar eclipse: making a comparison, before and during the event, of the positions of stars projected near the Solar surface. Several attempts were made during solar eclipses but they were limited by the outbreak of World War I and bad weather. In 1919, two expeditions organised by Sir Arthur Eddington (figure 1.2), led to a measurement of the light deflection consistent with the relativistic prediction. This was an historic result, even if this theory had already explained Mercury's perihelion shift, since it represented an important confirmation of the General Relativity.

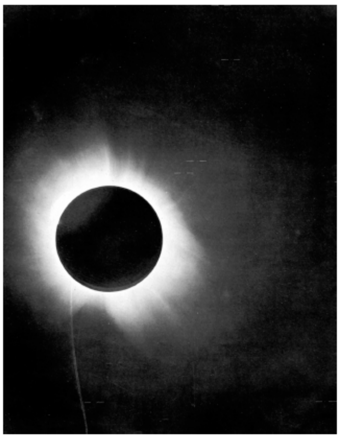

Figure 1.2: Picture of the solar eclipse of the 1919. [Dyson et al. (1920)]

In the same year Lodge introduced for the first time the term *lens* to describe this phenomenon.

In 1936 Einstein, on the suggestion of the engineer Rudi Mandl, considered the lensing effect produced by massive bodies in the universe: more specifically, Mandl thought that in a lens system made of two stars the distant one would appear brighter. The author of the General Relativity was pessimistic about a possible detection of the phenomenon, stating that the angular separation between images would be too small to be resolved. This conclusion did not take into account that there are more massive gravitational lenses, than the stars, that can generate this effect.

In 1937 Fritz Zwicky introduced the idea that also galaxies and clusters of galaxies could produce lenses. In this case, due to the higher masses involved, the angular separation would be high enough to make pairs of images resolvable with telescopes. A possible detection of this kind of lensing events could be useful to enhance the galaxy observations at larger distances and to determine the mass distribution of the galaxies acting as lenses. Zwicky also sustained that the detection of a galaxy acting as a gravitational lens would be a matter of time, since from his calculations it was basically a certainty. The same American astronomer understood that galaxy clusters contained an important amount of invisible matter capable of defining strong gravitational fields; today this type of matter is referred to as *dark matter*. Therefore, in combination with other techniques, constraining the distribution of luminous matter, the gravitational lensing could be used to infer the distribution of the dark matter.

The reconsideration of the gravitational lensing

Gravitational lensing was reconsidered at the beginning of the 1960s thanks to Klimov, Liebes and Refsdal. Klimov took into account, for the first time, the lensing of galaxies by galaxies while Liebes supposed that a Milky Way's star could act as a lens for a star in the Andromeda galaxy (M31). Refsdal's contribution was equally important, introducing calculations about time delay between two images of a single source. According to him, measuring the image separation and the time delay it could be possible to determine the lens mass and the Hubble constant. This technique requires sources whose brightness varies with time, such as quasars and supernovae.

A further step forward was represented by the first quasars detection in 1963. These luminous, compact and distant sources proved to be useful for the detection of gravitational lenses. In figure 1.3 there is a representation of a gravitational lens system in which the background source is a quasar.

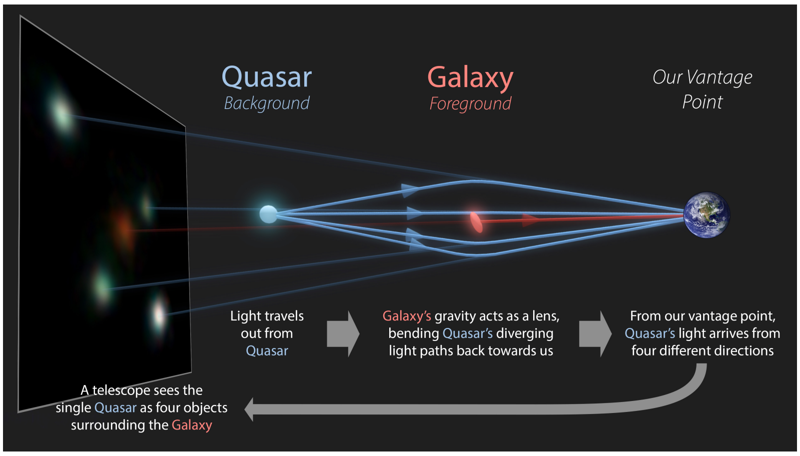

Figure 1.3: Diagram that illustrates how the image of a distant quasar is modified by the presence of a galaxy along the line of sight. [Hurt & The GraL Collaboration (2021)]

Nevertheless, only 15 years later the first lens was identified mainly due to the lack of adequate tools necessary to confirm these theoretical speculations.

1.1.2 Observational confirmations

First detection of multiple images

Thanks to the technological progress, represented by more powerful telescopes and Charged-Coupled-Devices (CCD), it was possible to observe multiple images of the same source. This crucial step determined the moment in which gravitational lensing had entered the field of observational science. In 1979 Walsh et al. discovered a pair of quasars, reported in figure 1.4, separated by 6 arcsecond and characterised by identical colours, redshifts ($z = 1.41$) and spectra, reported in figure 1.5. Further analysis using the radio interferometer VLA (Very Large Array) confirmed that both quasar images were compact radio sources and showed a similarity in the radio spectra. Later there was the detection of a galaxy, the brightest galaxy ($z = 0.36$) of a small cluster, in between the two quasars. Only with the advent of the VLBI (Very Long Baseline Interferometry) it was clear that this system, known as QSO 0957+561, could be identified as the first gravitational lens: the two quasars observed actually were two images of the same quasar.

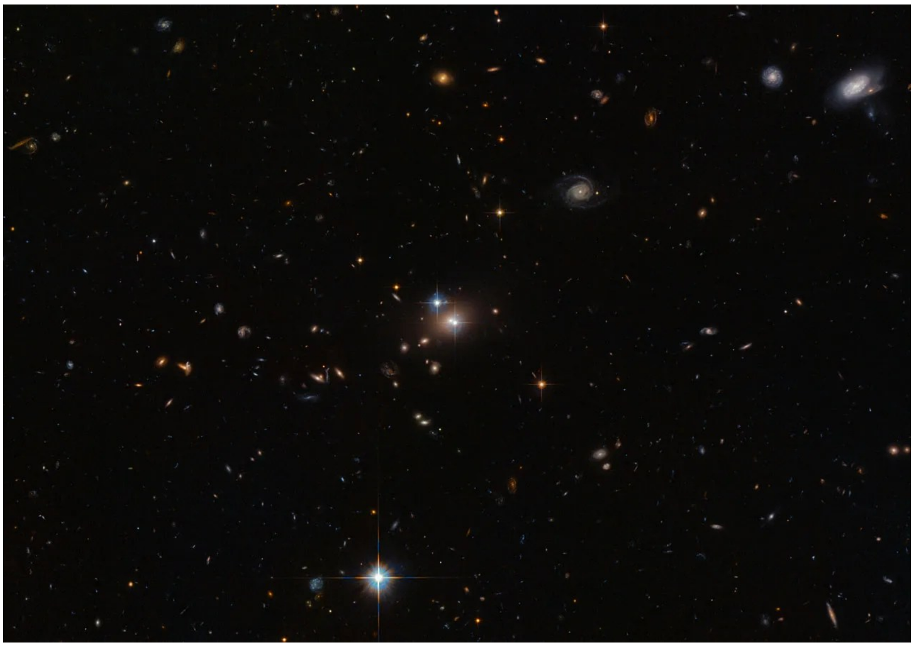

Figure 1.4: Observation, performed with the Hubble Space Telescope, of the system QSO 0957+561. Credit: ESA/Hubble and NASA. [Fox (2015)]

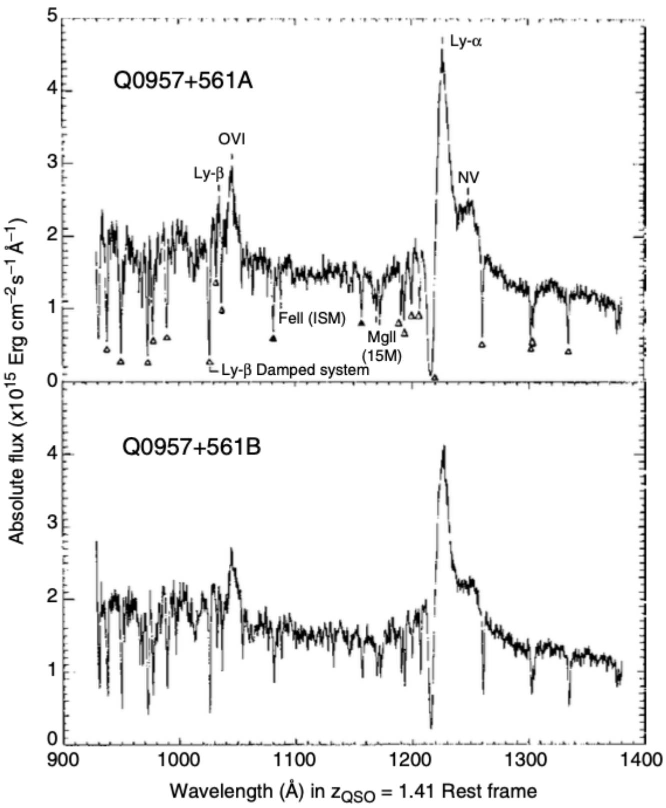

Figure 1.5: Spectra of the two quasar images of QSO 0957+561. These spectra, obtained with the Faint Object Spectrograph of the HST, highlight the fact that we see two images of the same object. [Schneider & Kochanek & Wambsganss (2006)]

Until 1990, more lenses have been detected thanks to systematic searches and serendipitous identifications.

Detection of giant luminous arcs

Gravitational arcs can be produced when an extended source undergoes the lensing, so the images distorted by the lens can also merge and generate these arcs. The problem is that these structures, visually striking, are not unambiguously identified. Two independently working groups (Lynds and Petrosian 1986; Soucail et al. 1987) detected elongated, giant luminous arcs curving around the center of the cluster Abell 370, reported in figure 1.6.

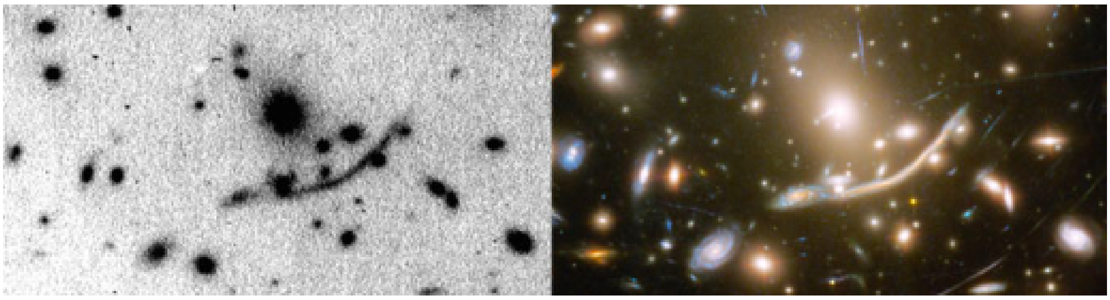

Figure 1.6: Gravitational arcs observed in Abell 370: in the left panel there is a I-band image (from the public Canada-France-Hawaii-Telescope archive) while in the right panel there is an image obtained with the HST. [Meneghetti (2021)]

After the measurement of the redshift of the giant arc, that results higher than the one of the cluster, it became clear that it was a lensing system. More specifically the arc was a distorted and magnified image of a higher redshift galaxy.

Detection of the Einstein rings

In 1912 Einstein considered that a source aligned with a foreground mass would appear as a ring, known as the *Einstein ring* and presented in figure 1.7, around the lens. Instead, without the alignment the source would be visible in the form of two images, on the opposite sides of the foreground mass.

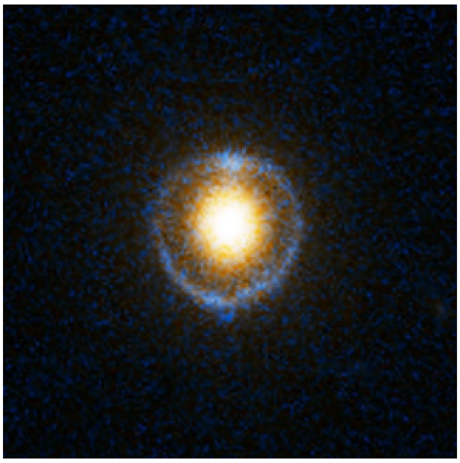

Figure 1.7: Image of the Einstein ring associated to the gravitational lens SDSS J162746.44-005357.5. The image was obtained using the HST. Credit: NASA, ESA, A. Bolton (Harvard-Smithsonian CfA) and the SLACS Team [Bolton (2005)]

In 1988 Hewitt et.al discovered a radio ring in the source MG 1131+0456 that could be modelled by a gravitational lens. Later thanks to HST high-resolution imaging, in the optical and the near-infrared, many Einstein rings in various multiply imaged quasars were revealed.

Detection of quasar microlensing

The distortion of a quasar's image, due to the presence of foreground galaxies, is variable as a function of the time. The result is a consequence of the relative movements of the lens components and manifests itself in a variation of the magnification with time. Even if this microlensing effect occurs on small angular scales it was successfully detected in 1989, observing the quasar QSO 2237+0305.

Detection of weak lensing

The weak gravitational lensing effect, that is the average light distortion caused by local ensembles of galaxies (figure 1.8), was first observed in 1990 looking at two clusters. Later, the advent of CCD cameras led to quantitative studies and in 2000 effects produced by the large-scale matter distribution in the Universe were detected.

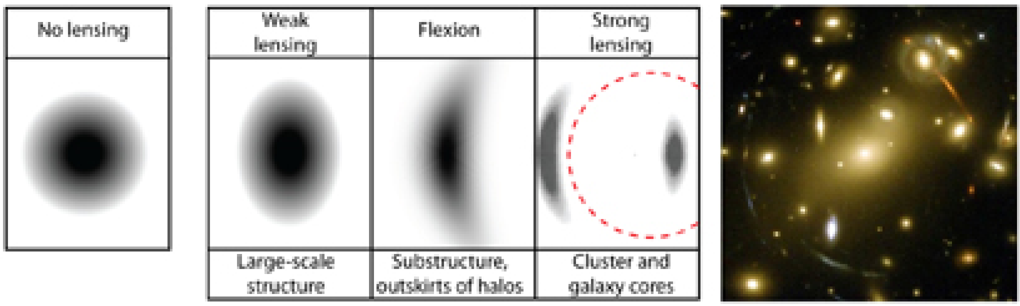

Figure 1.8: The right panel is an image of the galaxy cluster Abell 2218. In the left panel there is a brief explanation of the features that we can notice in the cluster, considering as a starting point a circularly symmetric image. [Euclid (2019)]

Detection of time delays

The possible application of time delays to determine the Hubble constant motivated the monitoring, in the optical and radio, of the light curves of QSO 0957+561. Using the light curves it was possible to estimate the time delay, eventually confirmed in 1996 as 417 ± 3 days. Even if further steps have been taken to improve the measure of time delays, they still lead to problematic results in the determination of the Hubble constant.

Detection of galactic microlensing

Considering that the light of extragalactic stars could be distorted by stars in the Milky Way, Paczynski suggested in 1986 to study the brightness variability of stars in the Large Magellanic Cloud (LMC). In 1993 a microlensing event of this kind was observed and a similar effect was also noticed toward the Galactic bulge.

1.2 Light deflection

This section is dedicated to a Relativistic description of light deflection in the presence of a gravitational field.

1.2.1 Light deflection by a point mass

Light deflection can be approached considering the field equations of General Relativity or treating it as a refraction problem. For the latter method the starting point is represented by the Fermat's principle that describes how the light path between two points is the one that minimises the travel time

$$t_{travel} = \int \frac{n}{c} dl \tag{1.3}$$

At the same time, the light path $\vec{x}(l)$ is consistent with

$$\delta \int_A^B n(\vec{x}(l))dl = 0 \tag{1.4}$$

First of all we need to determine the refractive index n, this computation is simplified with the following assumptions:

1. we are working with a *weak lens*, meaning that its Newtonian gravitational potential ϕ satisfies the following relation $\phi/c^2 << 1$
2. we are working in a *small region*, therefore the expansion of the universe is not considered

Due to the principle of equivalence we consider a locally inertial frame, with a flat space-time described by the Minkowski's metric, and look at how a weak lens is perturbing it:

unperturbed metric

$$\eta_{\mu\nu} = \begin{pmatrix} 1 & 0 & 0 & 0 \\ 0 & -1 & 0 & 0 \\ 0 & 0 & -1 & 0 \\ 0 & 0 & 0 & -1 \end{pmatrix}$$

perturbed metric

$$g_{\mu\nu} = \begin{pmatrix} 1+\frac{2\phi}{c^2} & 0 & 0 & 0 \\ 0 & -(1-\frac{2\phi}{c^2}) & 0 & 0 \\ 0 & 0 & -(1-\frac{2\phi}{c^2}) & 0 \\ 0 & 0 & 0 & -(1-\frac{2\phi}{c^2}) \end{pmatrix}$$

unperturbed line element

$$ds^2 = \eta_{\mu\nu} dx^\mu dx^\nu = c^2 dt^2 - (d\vec{x})^2$$

perturbed line element

$$ds^2 = g_{\mu\nu} dx^\mu dx^\nu = (1+\frac{2\phi}{c^2})c^2 dt^2 - (1-\frac{2\phi}{c^2})(d\vec{x})^2$$

Since we are analysing light $ds = 0$, this leads to

$$\left(1 + \frac{2\phi}{c^2}\right) c^2 dt^2 = \left(1 - \frac{2\phi}{c^2}\right) (d\vec{x})^2 \tag{1.5}$$

so, as a consequence, the speed of light in the gravitational field is

$$c' = c\sqrt{\frac{1 + \frac{2\phi}{c^2}}{1 - \frac{2\phi}{c^2}}} \approx c\left(1 + \frac{2\phi}{c^2}\right) \tag{1.6}$$

Finally, we can compute the refractive index

$$n = \frac{c}{c'} = \frac{1}{1 + \frac{2\phi}{c^2}} \approx 1 - \frac{2\phi}{c^2} \tag{1.7}$$

These approximated formulas have been obtained using ϕ/c^2. Observing the (1.6) relation it is clear that with $\phi \leq 0$ ($n \geq 1$) we get $c' < c$: the light speed in the gravitational field is smaller.

Now, solving the standard variational problem represented by the formulas (1.3) and (1.4) we get to the total deflection angle of the light:

$$\hat{\vec{\alpha}} = \frac{2}{c^2} \int_{\lambda_A}^{\lambda_B} \vec{\nabla}_{\perp} \phi d\lambda \tag{1.8}$$

this is the integral over the action of the gravitational potential that is perpendicular to the light trajectory. To avoid performing the integration over the actual light path, we assume $\phi/c^2 << 1$, therefore the deflection angle will be small and we can use the Born approximation. This consideration makes it possible to use the gravitational potential along the unperturbed trajectory instead of the one along the deflected trajectory. A representation of a general lens system is reported in figure 1.9.

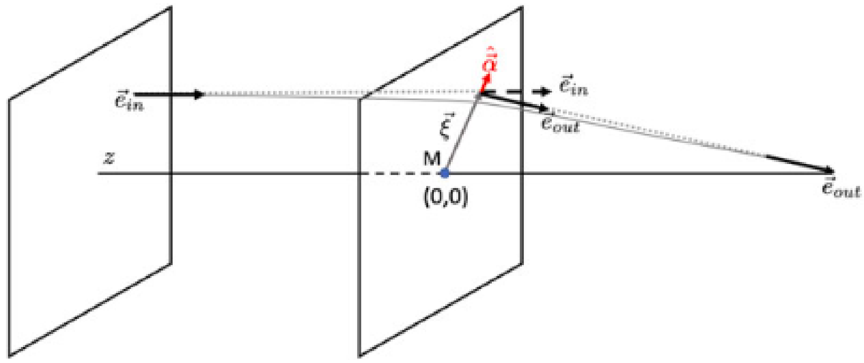

Figure 1.9: Representation of the lens system that we are analysing. More specifically the solid line represents the deflected trajectory of light while the dashed one is the normal trajectory. [Meneghetti (2021)]

Making a reference to figure 1.9, a light ray coming from the source plane (the one on the left side) and passing through a lens at $z = 0$, with a specific impact parameter ξ , will be deflected by the angle

$$\hat{\vec{\alpha}}(\xi) = \frac{2}{c^2} \int_{-\infty}^{+\infty} \vec{\nabla}_{\perp} \phi(\xi, z) dz \tag{1.9}$$

To compute the deflection angle for the case of a point mass we substitute $\phi = -GM\sqrt{\xi^2 + z^2}$ and obtain

$$\hat{\vec{\alpha}}(\xi) = \frac{4GM}{c^2 \xi^2} \vec{\xi} \tag{1.10}$$

1.2.2 Light deflection by multiple point masses

Computing the light deflection angle produced by multiple point masses is possible using the superposition principle: the final deflection angle is obtained summing the contributions of each single point mass.

Considering a plane with N $(1 \leq i \leq N)$ point masses with positions $\vec{\xi}_i$ and masses M_i; a light ray propagating through the plane at $\vec{\xi}$ will be deflected by the following angle

$$\hat{\vec{\alpha}}(\vec{\xi}) = \sum_i \hat{\vec{\alpha}}_i(\vec{\xi} - \vec{\xi}_i) = \frac{4G}{c^2} \sum_i M_i \frac{\vec{\xi} - \vec{\xi}_i}{\left|\vec{\xi} - \vec{\xi}_i\right|^2} \tag{1.11}$$

1.2.3 Light deflection by an extended distribution of mass

To describe more realistic lens systems it is necessary to consider extended, three-dimensional, distributions of matter; these objects are described using their surface mass density:

$$\Sigma(\vec{\xi}) = \int \rho(\vec{\xi}, z) dz \tag{1.12}$$

that is the projection of the mass density perpendicular to the light ray. The characterisation of these distributions is always possible with the thin screen approximation, meaning that the lens's size is really small compared to the distances between the components of the lens system. Therefore, considering all the contributions from the mass distribution, the total deflection angle is

$$\hat{\vec{\alpha}}(\vec{\xi}) = \frac{4G}{c^2} \int \frac{(\vec{\xi} - \vec{\xi'})\Sigma(\vec{\xi'})}{\left|\vec{\xi} - \vec{\xi'}\right|^2} d^2\xi' \tag{1.13}$$

1.3 General lens

This section is dedicated to a brief description of a general lens and the effects that this system is able to generate on the observed images.

1.3.1 Lens equation

To describe a general lens is important to have a clear visualisation of the system, represented in figure 1.10, where a mass concentration at a redshift z_L deflects light rays coming from a source at a redshift z_S.

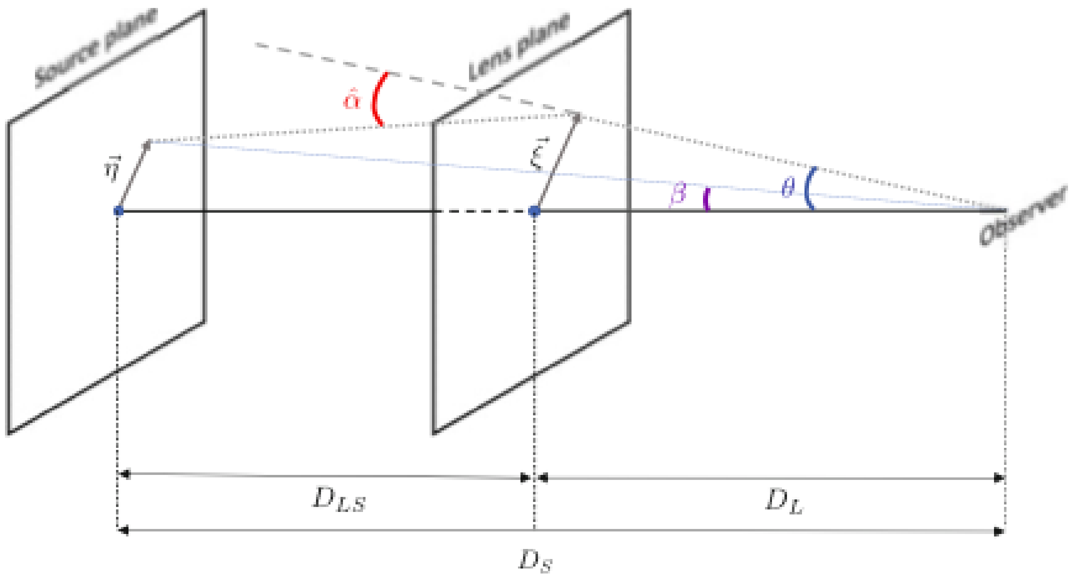

Figure 1.10: Representation of a general lens system that is characterised by: the source plane, the lens plane and the observer. To describe the positions of the source's images we use angles with respect to an axis, the optical axis, perpendicular to the planes: $\vec{\beta}$ describes the intrinsic position while $\vec{\theta}$ the apparent one. The third angle is $\hat{\vec{\alpha}}$ that represents the deflection of the light due to the presence of the lens. Below the sketch there are the angular diameter distances: D_L is the angular diameter distance between the lens and the observer, D_S is the angular diameter distance between the observer and the source and D_{LS} is the angular diameter distance between the lens and the source. [Meneghetti (2021)]

Considering the *thin screen approximation*, lens and source are approximated to planar distributions of mass and light, and for the small angles involved it is possible to introduce a relation known as the lens equation:

$$\vec{\theta} D_S = \vec{\beta} D_S + \hat{\vec{\alpha}} D_{LS} \tag{1.14}$$

that can be rewritten as

$$\vec{\beta} = \vec{\theta} - \hat{\vec{\alpha}}\frac{D_{LS}}{D_S} = \vec{\theta} - \vec{\alpha}(\vec{\theta}) \tag{1.15}$$

where $\vec{\alpha}(\vec{\theta})$ is the reduced deflection angle. The lens equation relates the intrinsic source position with its observed position on the sky. Therefore, with the source intrinsic position and the deflection angle we can obtain the positions of the images, but this approach is used only for lenses with simple mass distributions; in fact, usually the equation is non-linear and there can be multiple images. In addition, looking at a lens system the source intrinsic position is unknown so we need to reconstruct it using models for the mass distribution of the lens. In this case the equation is linear in $\vec{\beta}$.

The lens equation can also be expressed in a dimensionless form, so we need to define a length scale ξ_0 on the lens plane and compute the relative scale on the source plane $\eta_0 = \xi_0 D_S/D_L$. Therefore we obtain

$$\vec{y} = \vec{x} - \vec{\alpha}(\vec{x}) \tag{1.16}$$

where $\vec{x} = \vec{\xi}/\xi_0$ and $\vec{y} = \vec{\eta}/\eta_0$.

1.3.2 Lensing potential

Dealing with general lenses we need to characterised extended distributions of matter, this is possible introducing the lensing potential

$$\hat{\psi}(\vec{\theta}) = \frac{D_{LS}}{D_L D_S}\frac{2}{c^2}\int \phi(D_L\vec{\theta}, z)dz \tag{1.17}$$

that is obtained re-scaling the projection of the Newtonian potential onto the lens plane. The lensing potential has two important features:

1. its gradient is equal to the reduced deflection angle

$$\vec{\nabla}_\theta \hat{\psi}(\vec{\theta}) = \vec{\alpha}(\vec{\theta}) \tag{1.18}$$

2. its Laplacian is twice the convergence k

$$\triangle_\theta \hat{\psi}(\vec{\theta}) = 2k(\vec{\theta}) \tag{1.19}$$

with the convergence that is a dimensionless measure of the surface density defined using the critical surface density Σ_{cr}

$$k(\vec{\theta}) = \frac{\Sigma(\vec{\theta})}{\Sigma_{cr}} \quad \text{where} \quad \Sigma_{cr} = \frac{c^2}{4\pi G}\frac{D_S}{D_L D_{LS}} \tag{1.20}$$

The critical surface density is the characteristic value that divides weak and strong lenses. Integrating (1.19) we obtain the expressions of the lensing potential and the deflection angle as a function of the convergence

$$\psi(\vec{x}) = \frac{1}{\pi}\int_{\mathbb{R}^2} k(\vec{x}')\ln|\vec{x}-\vec{x}'|\, d^2x' \tag{1.21}$$

$$\vec{\alpha}(\vec{x}) = \frac{1}{\pi}\int_{\mathbb{R}^2} k(\vec{x}')\frac{\vec{x}-\vec{x}'}{|\vec{x}-\vec{x}'|} d^2x' \tag{1.22}$$

1.3.3 Lens map

Gravitational lensing is able to distort images, this effect is manifestly clear when is applied to extended sources. Solving the lens equation, across the entire extended source, we understand the shape of the images.

When the angular scale, over which the lens deflection angle field changes, is much bigger than the source, we can locally linearise the relation between source and image positions. Therefore we consider the *first order lens mapping*, that is visually represented in figure 1.11.

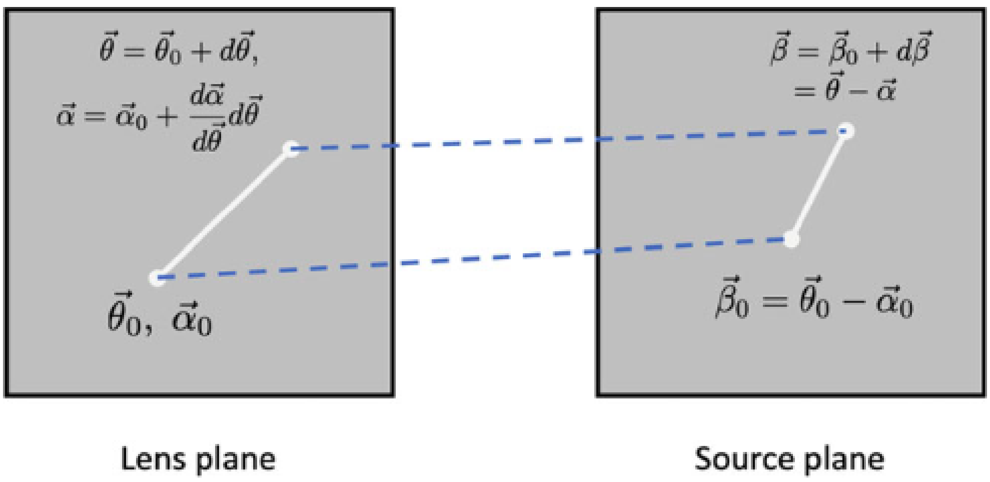

Figure 1.11: Visual representation of the first order lens mapping. [Meneghetti (2021)]

We want to describe the mapping from θ into β so from the lens plane into the source plane. Starting from the lens equation and using the equations reported in the above illustration, we get the definition of the vector $(\vec{\beta} - \vec{\beta}_0)$ that is equal to

$$(\vec{\beta} - \vec{\beta}_0) = \left(I - \frac{d\vec{\alpha}}{d\vec{\theta}}\right)(\vec{\theta} - \vec{\theta}_0) \tag{1.23}$$

So, the deformation of images can be illustrated by the Jacobian matrix A

$$A = \frac{\partial \vec{\beta}}{\partial \vec{\theta}} = \left(\delta_{ij} - \frac{\partial \alpha_i(\vec{\theta})}{\partial \theta_j}\right) = \left(\delta_{ij} - \frac{\partial^2 \hat{\psi}(\vec{\theta})}{\partial \theta_i \partial \theta_j}\right) = \left(\delta_{ij} - \hat{\psi}_{ij}\right) \tag{1.24}$$

where the subscripts i, j specify the components with which we are working.

This Jacobian matrix can be expressed in terms of the convergence, already introduced, and the shear tensor Γ

$$A = \begin{pmatrix} 1 - k - \gamma_1 & -\gamma_2 \\ -\gamma_2 & 1 - k + \gamma_1 \end{pmatrix} = (1-k)I - \Gamma = (1-k)\begin{pmatrix} 1 & 0 \\ 0 & 1 \end{pmatrix} - \gamma \begin{pmatrix} \cos 2\phi & \sin 2\phi \\ \sin 2\phi & -\cos 2\phi \end{pmatrix} \tag{1.25}$$

in which

- the convergence k introduces a re-scaling of the images by a constant factor in all directions, therefore it describes an isotropic deformation
- the shear tensor Γ is responsible for the stretching, along a particular direction defined by the angle ϕ, of the source shape and the shrinking in the perpendicular direction.

1.3.4 Magnification

The shape of the lensed images can be determined by solving the lens for all the points of the initial source. However, gravitational lensing not only distorts the observed images but also produces a magnification effect. Considering that the intrinsic luminosity of a source is unknown, the magnification cannot be treated as an observable. According to the Liouville theorem, light deflection does not change the surface brightness of the source but it changes the solid angle under which it is observed. Therefore, the flux observed is magnified or demagnified according to this variations.

The magnification μ is described as the determinant of the magnification tensor M that coincides with A^{-1}

$$\mu = \det M = \frac{1}{\det A} = \frac{1}{(1-k)^2 - \gamma^2} \tag{1.26}$$

where the eigenvalues of M correspond to the amplification in the directions defined by the eigenvectors of Γ. Considering the case of an axially symmetric lens we can see that there are curves, in the lens plane, where the magnification is ideally infinite that are called critical lines ($\det A = 0$). Mapping these critical lines, using the lens equation, into the source plane we get the caustics curves. The position of a source with respect to the caustics determines the number of images that will be produced.

1.3.5 Multiple imaging

There are two criteria we can use to understand if a matter distribution, with k, is able to produce multiple images:

1. a transparent, isolated lens produces multiple images if there is a point θ where $\det A(\theta) < 0$

2. a lens produces multiple images if there is a point θ where $k(\theta) > 1$. This is a sufficient, but not necessary, condition which provides insights into why these lenses are called strong.

1.3.6 Time delay

An important consequence of gravitational lensing is the time delay introduced in the propagation of the light rays, This latency is made of two components

$$t = t_{grav} + t_{geom} \tag{1.27}$$

where:

- $t_{grav} = -\frac{D_L D_S}{D_{LS}} \frac{1}{c} \hat{\psi}$ is the *gravitational time delay*, that can be quantified measuring how the presence of a gravitational potential changes light travel time

- $t_{geom} = \frac{\Delta l}{c}$ is the *geometrical time delay* and is a consequence of the different length of the light path in the presence of a gravitational field

The total time delay caused by the lensing, at a position $\vec{\theta}$ on the image plane is equal to

$$t(\vec{\theta}) = \frac{(1 + z_L)}{c} \frac{D_L D_S}{D_{LS}} \left[\frac{1}{2} (\vec{\theta} - \vec{\beta})^2 - \hat{\psi}(\vec{\theta}) \right] \tag{1.28}$$

this result describes the time delay surface, whose stationary points represent the positions where the images are located. It is important to introduce the Hessian matrix of this surface

$$T_{ij} = \frac{\partial^2 t(\vec{\theta})}{\partial \theta_i \partial \theta_j} \tag{1.29}$$

that is proportional to the Jacobian A_{ij}; therefore the curvature, at the image position, is inversely proportional to the magnification of the image. It is then possible to distinguish between three image types, according to their position on the time delay surface:

- *Type I images*, at the minima, with both eigenvalues that are positives and so they have positive magnification
- *Type II images*, at the saddle points, with eigenvalues of opposite signs and so they have negative magnification
- *Type III images*, at the maxima, with both eigenvalues that are negatives and so they have a positive magnification

The sign of the magnification is related to the parity, so the orientation of the image. Only in cases where $|\mu| < 1$ the image appears demagnified.

1.4 Main applications

This section is dedicated to a brief overview of the main lensing applications, which cover a wide spectrum.

As a matter of fact, gravitational lensing is not just a striking physical effect, but a real tool used to explore the universe in a way that has never been done before.

The main applications of this phenomenon are:

- **the measurement of the mass**, this determination is possible considering that lensing is sensitive to dark and luminous matter. Therefore, this phenomenon is useful to measure the total mass of astronomical objects. From the detection of multiple images and the Einstein rings we can infer the mass of a galaxy behaving as a lens. This approach, available also for the characterisation of galaxy clusters, obviously depends on the use of detailed modelling.

- **the constraint of the number density of mass distributions**, given that a lensing event can occur depending on the projected number density of the potential lenses. Studying samples of sources we can obtain the number density of lenses; an example is represented by the determination of the number density of dense objects in the dark matter halo of the Milky Way.

- **the estimate of cosmological parameters**, as already introduced by Refsdal with the idea of determining the Hubble constant exploiting the time delays in multiple images of the same source. This method, independent of the usual distance ladder, has given lower values with respect to those obtained using Cepheids. There are also other cosmological parameters that can be estimated and studied using these phenomenon.

- **the observation of distant sources**, given that lensing magnifies background objects. So this effect not only can be used to observe sources otherwise too faint to be detect but can also let us characterise objects in a better way, for example with spectroscopic data.

- **the search for exoplanets**, that is simplified considering that planets, with the right orbital phase and distance from their star, can leave traces in microlensing light curves. This technique is particularly efficient in the case of low-mass planets orbiting around distant stars.

Chapter 2

Strong galaxy-galaxy lensing

2.1 Introduction to strong gravitational lensing

To understand the properties of a gravitational lens we need to consider the type of system with which we are working, more specifically, the effects that it is able to generate. Considering, as already done in subsection 1.3.2, that a key parameter is the critical surface density, we can distinguish between two regimes:

- if $\Sigma > \Sigma_{cr}$ we are in the **strong lensing regime**, with massive lenses that are able to produce multiple images, arcs, and rings when deflecting the light from a background source
- if $\Sigma < \Sigma_{cr}$ we are in the **weak lensing regime**, where the produced effects can be appreciated within a much larger scale

To highlight this clear distinction, one can refer to figure 2.1.

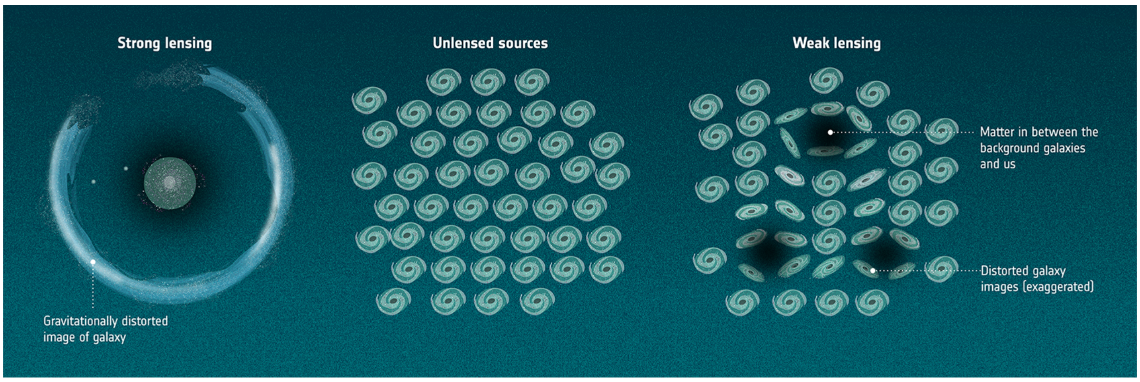

Figure 2.1: Representation of the different effects of the two regimes, starting from a group of unlensed sources. Credits: ESA [Euclid Consortium (2023)]

From now on the focus will be on strong gravitational lenses and their features. A good way to start describing this specific class of lenses is the introduction of some data, in particular referring to the reasonably complete summary of lenses that is available on the CASTLES (CfA-Arizona Space Telescope LEns Survey of gravitational lenses) site [Kochanek et al.]. This site provides information, data, and images about gravitational lens systems; it is worth noting that it also includes multiply imaged systems. The majority of the lenses have "standard" geometries for models in which the quadrupole moments of the density distribution determine the angular structure of the gravitational potential. Among the CASTLES list there are lenses with $1 < N_{images} < 6$ and also lenses with extended images or Einstein rings. The cases with two (*doubles*) or four images (*quads*) are generated by standard lenses with nearly singular central surface densities. It is important to notice that in *doubles*, an example is reported in figure 2.2, the images are at different distances from the galaxy behaving as a lens, this is explained by the fact that the source has to be offset from the center of the lens otherwise four images will be produced. For the *quads*, there are three generic patterns that depend on the source position with respect to the center of the lens and the caustics. Considering the caustic theory, the expected patterns are the following:

- *cruciform quads*, with the source almost directly behind the lens, that produce cross patterns. An example is reported in figure 2.3
- *fold-dominated quads*, with the source close to a fold caustic, that produce highly magnified images that are close to each other
- *cusp-dominated quads*, with the source close to a cusp caustic, that produce triples of highly magnified images

Instead, systems with non-standard geometries arise from different situations where more complicated sources lead to more complicated image geometries.

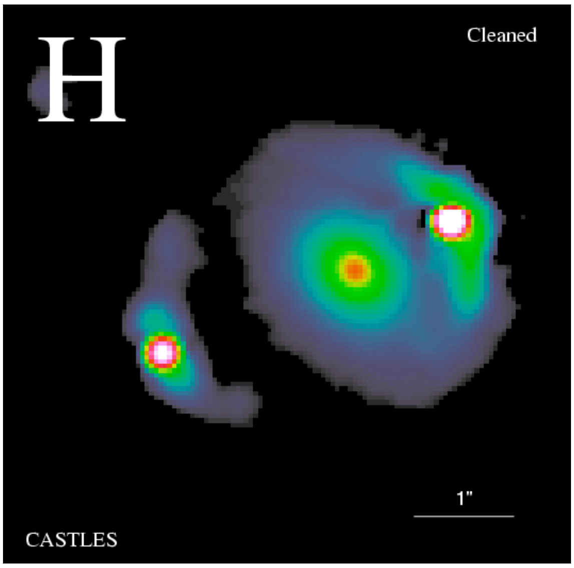

Figure 2.2: Cleaned picture of HE1104-1805, a two-image lens, that is obtained working in the H-band (NIR).[Kochanek et al.]

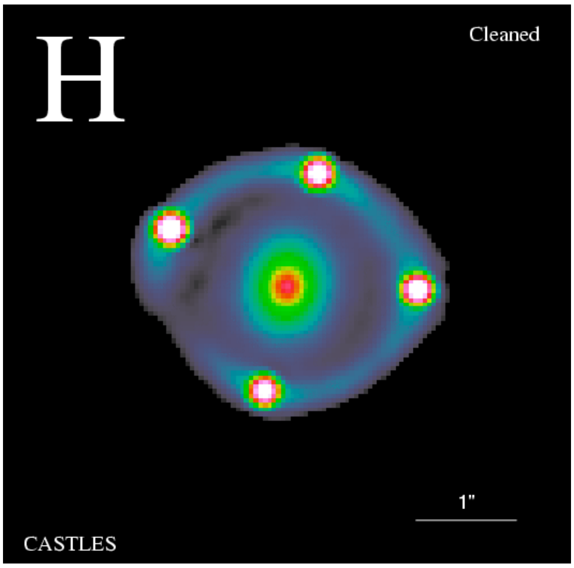

Figure 2.3: Cleaned picture of HE0435-1223, a cruciform quad, that is obtained working in the H-band (NIR).[Kochanek et al.]

2.2 Modeling extended lenses

Multiple images and gravitational arcs are effects related to galaxies and galaxy clusters behaving as lenses; the characterisation of these extended mass distributions allows us to understand the relationship between specific lens properties and the observed effects. The starting point is the introduction of circular and axially symmetric models. Then, the deviations from these models will be considered, including the ellipticity of the lenses and the possible presence of substructures. The lens environment will also be taken into account, considering the importance of its influence on the final effects observed.

2.2.1 Circular lens models

Modelling gravitational lenses with circular models is important to introduce the elements of a general lens model. Nevertheless, this model does not apply to real lenses, since we cannot overlook their angular structure. For these lenses the lensing potential is constant on concentric circles around the lens center, therefore the effective potential depends only on the distance from the lens center

$$\hat{\psi}(\vec{\theta}) = \hat{\psi}(\theta) \tag{2.1}$$

Then, the deflection angle, equal to the gradient of the lensing potential in angular units, results in

$$\alpha(\theta) = \frac{2}{\theta}\int_0^\theta \theta k(\theta) d\theta = \frac{4GM(<\xi)}{c^2\xi}\frac{D_{LS}}{D_S} \tag{2.2}$$

We can notice that, due to the symmetry, the properties of the lens depend only on the mass profile $M(<\xi)$. Therefore, the lens equation becomes the following

$$\beta = \theta[1 - \alpha(\theta)/\theta] = \theta[1 - \langle k(\theta)\rangle] \tag{2.3}$$

where, since we are talking about strong gravitational lensing, there must be an area with $\langle k\rangle > 1$ that results in the production of two images on the opposite sides of the lens. The positions of the images are not random, but by symmetry, are distributed along a line that connects the source position and the center of the lens.

In dimensionless notation, the equation becomes

$$y = x - \frac{m(x)}{x} \tag{2.4}$$

where $m(x) = \frac{M(\xi_0 x)}{\pi {\xi_0}^2 \Sigma_{cr}}$ is the dimensionless mass that will be important in the introduction of power-law lenses. In circular lens models, the convergence and the shear acquire the following forms

- the convergence $k = \frac{1}{2}\left(\frac{\alpha}{\theta} + \frac{d\alpha}{d\theta}\right)$
- the shear $\gamma = \frac{1}{2}\left(\frac{\alpha}{\theta} - \frac{d\alpha}{d\theta}\right)$

and in dimensionless notation, we get

- the convergence $k(x) = \frac{1}{2}\frac{m'(x)}{x}$
- the shear $\gamma(x) = |k(x) - \overline{k}(x)|$, where $\overline{k}(x) = \frac{m(x)}{x^2}$ is the mean convergence within a circle of radius x

It is also important to consider the inverse magnification tensor, whose eigenvectors point in the radial and tangential directions with the following eigenvalues

- radial eigenvalue $\lambda_+ = 1 - k + \gamma = 1 - d\alpha/d\theta$
- tangential eigenvalue $\lambda_- = 1 - k - \gamma = 1 - \alpha/\theta = 1 - \langle k \rangle$

when equal to zero they describe either radial or tangential critical curves, meaning that the magnification diverges in that direction. More specifically, the tangential critical line is represented by the lens Einstein ring, which has a radius equal to

$$\theta_E = \sqrt{\frac{4GM(\theta_E)}{c^2}\frac{D_{LS}}{D_L D_S}} \tag{2.5}$$

usually known as the Einstein radius. With $M(\theta_E)$ that describes the mass contained within the Einstein ring.

2.2.2 Power-law lens models

To further explain how a circular lens model works, it is useful to evaluate different density profiles, more specifically focusing on power-law lenses. This class of lenses is described by a specific form of the mass profile $m(x) = x^{3-n}$. Starting from this expression, we can define several features:

- the density distribution $\rho \propto r^{-n}$

- the deflection angle $\alpha(\theta) = b\left(\frac{\theta}{b}\right)^{2-n}$
- the convergence $k(\theta) = \frac{3-n}{2}\left(\frac{\theta}{b}\right)^{1-n}$
- the shear $\gamma(\theta) = \frac{n-1}{2}\left(\frac{\theta}{b}\right)^{1-n}$

In general, these models are characterised by the following eigenvalues:

- the tangential magnification eigenvalue $1 - k - \gamma = 1 - (\theta/b)^{1-n}$ that becomes zero at $\theta = b = \theta_E$, also known as the Einstein radius. For circular lenses, inside of this circle $\langle k \rangle = 1$
- the radial magnification eigenvalue $1-k+\gamma = 1-(2-n)(\theta/b)^{1-n}$ that becomes zero only with $n < 2$. So there can be two different scenarios: for $n < 2$ the lens has a radial critical curve inside the tangential one, while for $n > 2$ the deflection is constant or increases toward the center

An important feature of circular lenses is that they have simple visual solutions of the lens equation starting from deflection profiles. The idea is that after determining the radial positions of the images, using the source position, we can compare the area of the images with that of the source, in order to determine the magnification.

These lenses describe simple and interesting models that can be separated and differentiated based on the value of n. We can appreciate their features in the following brief introduction. It is important to remember that to focus on lenses that have bound mass distributions, we consider only values of $n > 1$. After the introduction, in table 2.1, of few differences between lenses with $1 < n < 2$ and with $n > 2$, there will be a description of some specific models that are listed in order of increasing power-law index n.

Criterion	**Lenses with** $1 < n < 2$	**Lenses with** $n > 2$
Deflection angle profiles	Monotonically increase with x and vanish at the origin	Either flat ($n = 2$) or singular ($n > 2$)
Multiple images	Either one or three	For $n > 2$, always two

Table 2.1: Comparison between lenses with different power-law indices

Uniform critical sheet (n=1)

This model is defined by the limit $n \to 1$ and the deflection angle $\alpha = \theta$. The convergence is $k = 1$ and the shear becomes $\gamma = 0$.

Moore profile (n=3/2)

This softer power law model, defined by $n = 3/2$, has the cusp exponent of the Moore, Quinn et al. (1999) model introduced for Cold Dark Matter (CDM) halos. According to the absolute value of β, there can be two different scenarios:

- for $|\beta| > b/4$ there is only one image in a minimum at $\theta_1 = \frac{1}{2}(b + 2\beta + \sqrt{b+4\beta}) > b$ considering $\beta > 0$. Magnification tends to infinity at $\theta = b$ when the source is on the tangential pseudo-caustic.

- for $|\beta| < b/4$ there is the formation of two additional images

  1. in the saddle point at $-b < \theta_1 = \frac{1}{2}(-b + 2\beta - \sqrt{b+4\beta}) < -b/4$ with a negative magnification that tends to infinity at $\theta_2 = -b/4$ and at $\theta_2 = -b$ where the tangential critical curve is located. Instead, the radial critical curve is defined by the radius $\theta = b/4$.
  2. in a maximum at $-b/4 < \theta_3 = \frac{1}{2}(-b + 2\beta + \sqrt{b+4\beta}) < 0$ with a positive magnification that tends to infinity at the radial critical curve.

With the source moving outward from the center, the two additional images are going to merge on the radial critical line. This situation would result in the presence of only one image, and it can also be obtained by adding a core radius to the Singular Isothermal Sphere (SIS) model. The visual representation for the image structure is crucial to understand the meaning of partial parities considering as the reference the initial source structure:

- image 1, with positive partial parities, presents the same initial orientation

- image 2, with mixed partial parities, manifests a tangential inversion of the image

- image 3, with negative partial parities, presents an image inverted in both directions (radial and tangential)

When the total parity, product of the partial parities, is positive the image orientation can be obtained with a rotation of the source; otherwise this is not possible.

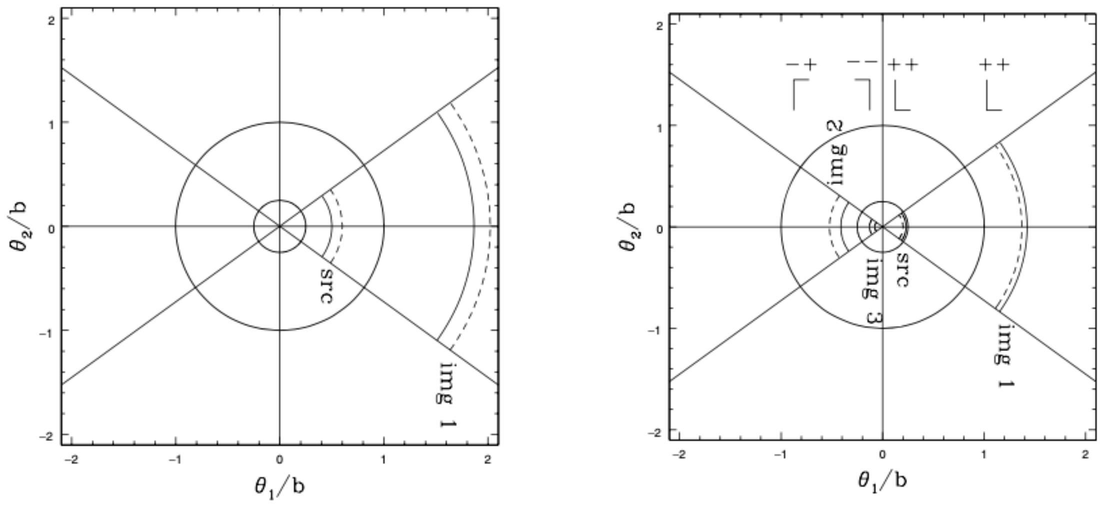

(a) $\beta > b/4$: only one image

(b) $\beta < b/4$: three images

Figure 2.4: Visual representation of the image structure for the Moore profile cusp lens. [Schneider & Kochanek & Wambsganss (2006)]

Singular isothermal sphere SIS (n=2)

This model represents the standard choice for galaxies, and it is based on the assumption that the matter content of the lens is behaving as an ideal gas, in thermal and hydrostatic equilibrium, trapped by a spherically symmetric gravitational potential. According to these conditions, the density profile is defined by

$$\rho(r) = \frac{\sigma_v^2}{2\pi G r^2} \tag{2.6}$$

where σ_v is the velocity dispersion of the gas particles and $r = \sqrt{\xi^2 + z^2}$ is the distance from the center of the sphere. Now, the projection of this three-dimensional density onto the lens plane leads to the surface density

$$\Sigma(\xi) = \frac{\sigma_v^2}{2G\xi} \tag{2.7}$$

that presents a singularity at $\xi = 0$. This model is defined by $n = 2$ and as a consequence the deflection angle is constant $\alpha = b$, while convergence and shear become $k = \gamma = b/2\theta$. The number of images produced depends on the value of β, more specifically with $0 < \beta < b$ there are two images, and otherwise there is only one. The two images produced in the first case are the following:

1. one in the minimum at $\theta_1 = \beta + b$ with $\mu_1 > 0$

2. one in the saddle point at $-b < \theta_2 = \beta - b < 0$ with $\mu_2 < 0$

The images are separated by a distance $|\theta_1 - \theta_2| = 2b$, with a total magnification $|\mu_1| + |\mu_2| = 2b/\beta$. The magnification produced is purely tangential considering that the radial magnification is unity.

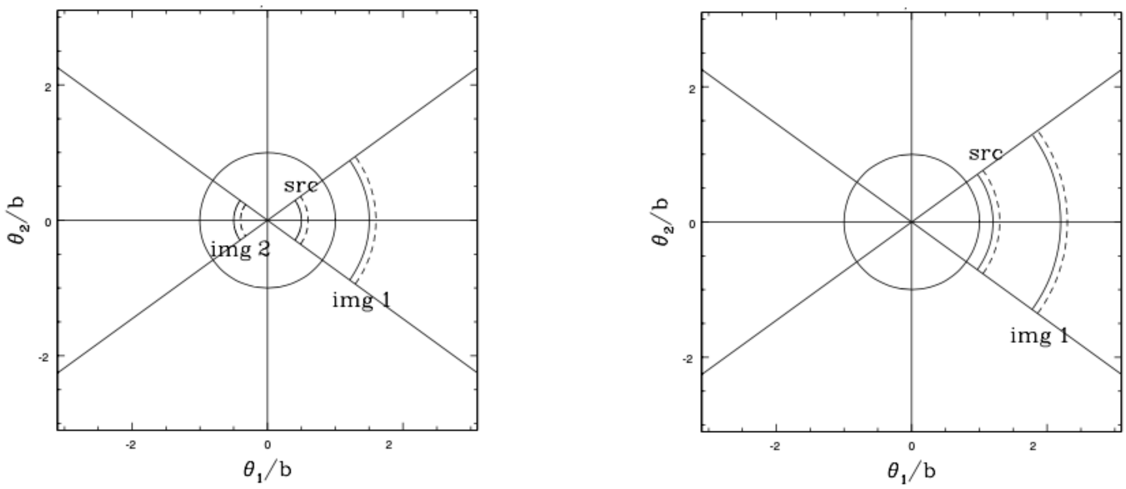

(a) $\beta < b$: two images

(b) $\beta > b$: only one image

Figure 2.5: Visual representation of the image structure for the singular isothermal sphere model [Schneider & Kochanek & Wambsganss (2006)]

The model can be generalised with the introduction of a core in the surface density profile

$$\Sigma(\xi) = \frac{\sigma_v^2}{2G} \frac{1}{\sqrt{\xi^2 + \xi_c^2}} \tag{2.8}$$

leading to the **Non-singular Isothermal Sphere (NIS)** lens model, in which up to three images are produced. The extended-source images produced by these two models can be seen in figure 2.6 and figure 2.7.

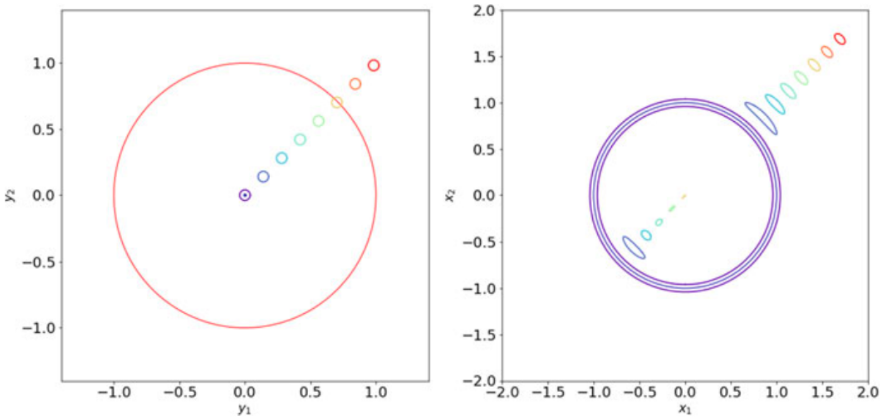

Figure 2.6: Extended-source images produced by the SIS lens. In the *left panel*, the red circle represents the pseudo-caustic while the blue point is the tangential caustic. There are also several extended circular sources, represented with different colors. In the *right panel*, there are the extended-source images produced by the SIS lens. It is important to notice that the blue circle is the Einstein ring. [Meneghetti (2021)]

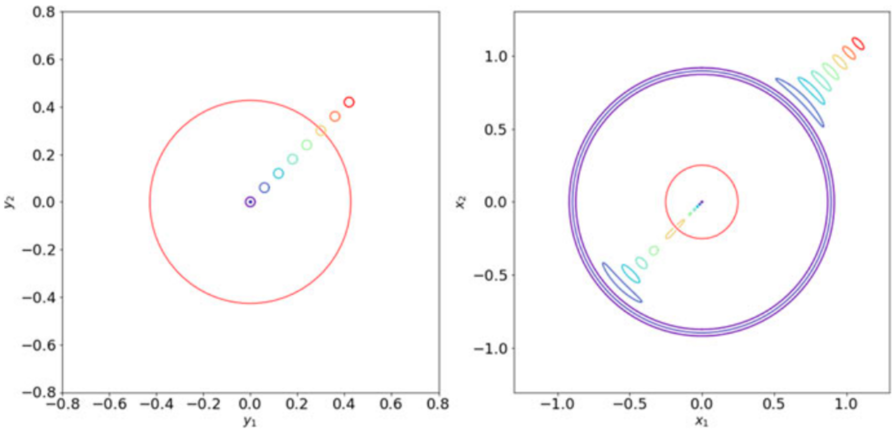

Figure 2.7: Extended-source images produced by the NIS lens. In the *left panel*, the red circle represents the radial caustic while the blue point is the tangential caustic. There are also several extended circular sources with different colours. In the *right panel*, there are the corresponding critical lines and also the extended-source images produced by the NIS lens. [Meneghetti (2021)]

Point-mass lens (n=3)

This model is characterised by the limit $n \to 3$ and the deflection angle $\alpha = b^2/\theta$. The convergence is $k = 0$ (with a central singularity), and the shear presents this form $\gamma = b^2/\theta^2$. This specific model generates two images on each lens side. Taking into account the condition $\beta > 0$, the two images are:

1. one in the minimum at $\theta_1 = \frac{1}{2}(\beta + \sqrt{\beta^2 + 4b^2} > \theta_E$ with $\mu_1 > 0$

2. one in the saddle point at $-\theta_E < \theta_2 = \frac{1}{2}(\beta - \sqrt{\beta^2 + 4b^2}) < 0$ with $\mu_2 < 0$

The images are separated by a distance, $|\theta_1 - \theta_2| \geq 2b$, larger than the diameter of the Einstein ring, and manifest a total magnification $|\mu_1| + |\mu_2| \geq 1$.

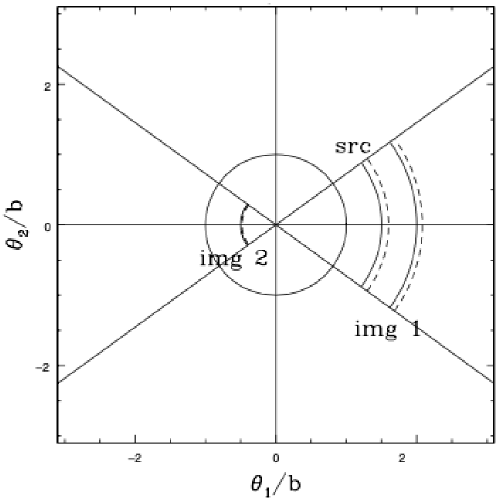

Figure 2.8: Visual representation of the image structure for the point mass lens. [Schneider & Kochanek & Wambsganss (2006)]

2.2.3 Non-circular lens models

A circular lens can become a non-circular model by adding any angular structure into the lens gravitational potential. Angular perturbations that define this transition are several. An example is the not perfectly circular shape of a lens galaxy; therefore, it is important to take into account the ellipticity of the galaxy's potential. Taking into account an axis ratio q, the ellipticity is represented by $\epsilon = 1 - q$. We also need to consider the tidal perturbations produced by nearby objects, also known as the *external shear*, since it can be represented as a linear distortion of the deflection field. The amplitude of this effect can be expressed by using a Taylor expansion of its potential near the lens. Now, we discuss how ellipticity affects the properties of lenses and then we consider the effects of external perturbations.

2.2.4 Elliptical lens models

The addition of the ellipticity, inevitably removing the axial symmetry of the lens, redefines the tangential caustic: from a point it becomes an astroid-like shape, with possibly two or four cusps. We now briefly consider some elliptical models to understand their main features.

Singular Isothermal Ellipsoid SIE

In this case, the surface density profile is described by

$$\Sigma(\vec{\xi}) = \frac{\sigma_v^2}{2G}\frac{\sqrt{f}}{\sqrt{\xi_1^2 + f^2\xi_2^2}} \tag{2.9}$$

where $0 < f \leq 1$ is the ratio of the axis of the ellipses. This model does not present a radial critical line, as seen for the SIS lens, because the radial magnification is always equal to one. At the same time, the tangential critical line forms an ellipse characterised by $k(\vec{x}) = 1/2$. The behaviour of these critical lines can be appreciated in figure 2.9.

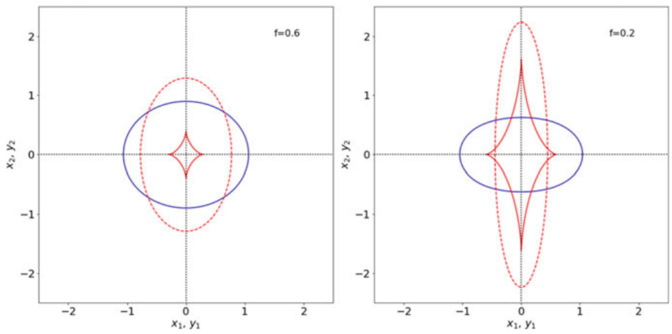

Figure 2.9: Visual representation, for a SIE lens, of the critical line (the dashed red line), the caustic (the solid red line) and the cut (the solid blue line). The left panel refers to a SIE lens with $f = 0.6$ while the right panel to $f = 0.2$. [Schneider & Kochanek & Wambsganss (2006)]

As we can see from this figure, the introduction of the ellipticity defines a transformation of the caustic: from a point into an extended curve with four cusps and four folds. Now, to find the multiple images produced by the SIE model, it is necessary to use numerical methods. However, it can be useful to observe how the different parts of the tangential critical line are mapped onto the caustic, as represented in figure 2.10.

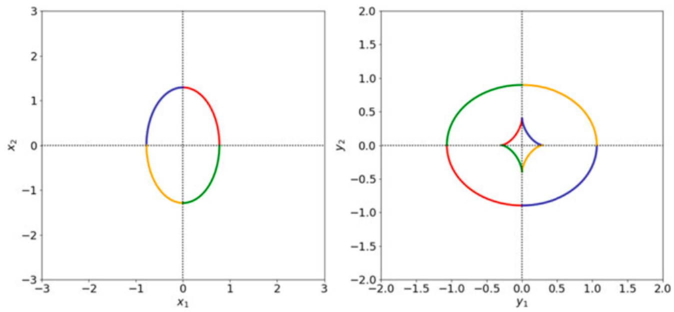

Figure 2.10: Mapping of the critical line (left panel) onto the caustic (right panel). To better understand how the mapping is working, there are different colours for each portion of the critical line. More precisely, the four colours corresponds to different quadrants on the lens plane. [Schneider & Kochanek & Wambsganss (2006)]

Finally, we consider, in figure 2.11, the images of circular sources that are lensed by a SIE lens.

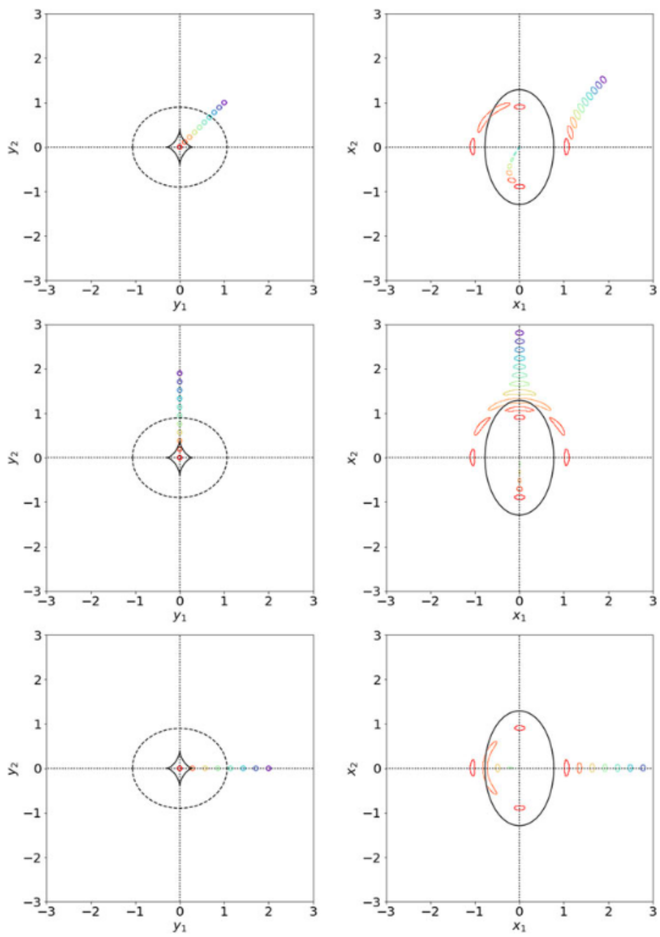

Figure 2.11: Images of circular sources that are lensed by a SIE lens with $f = 0.6$. In the left panel there are the caustics (solid line), the cut (dashed line) and positions of several circular sources. In the right panel there are the corresponding images and the critical line (solid line). [Schneider & Kochanek & Wambsganss (2006)]

Non-singular Isothermal Ellipsoid NIE

As in the SIS model, the SIE can be generalised with the addition of a core, and it is therefore named NIE. This model becomes more complicated from an analytical point of view, and the surface density is now described as

$$\Sigma(\vec{\xi}) = \frac{\sigma^2}{2G} \frac{\sqrt{f}}{\sqrt{\xi_1^2 + f^2\xi_2^2 + \xi_c^2}} \tag{2.10}$$

with ξ_c that describes the radius of the core. It is useful to visualise, in figure 2.12, the critical lines and caustics of the NIE lenses with different values of f and x_c.

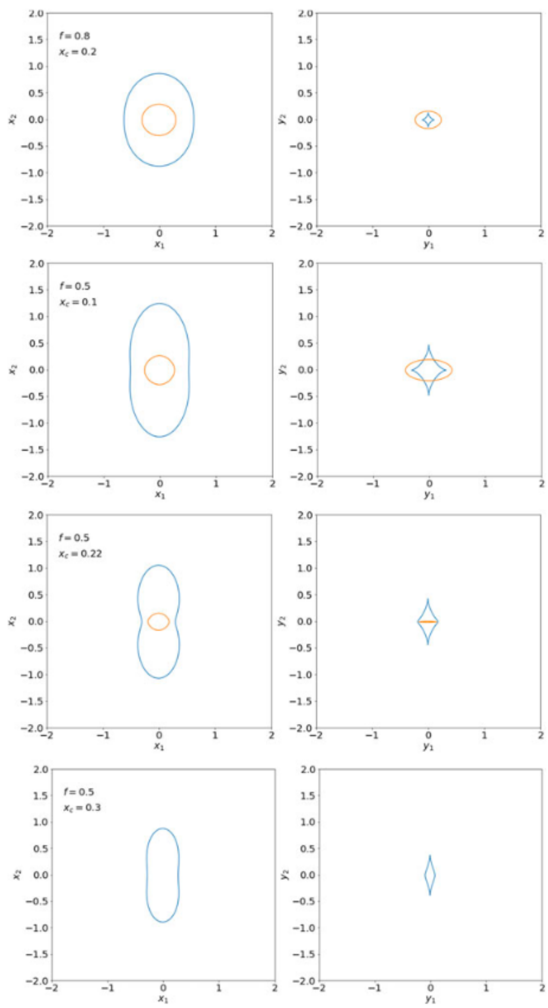

Figure 2.12: Representation of critical lines and caustics related to NIE lenses with different values of f and x_c. More specifically, these values determine whether the lens has two separate critical lines and caustics, one tangential critical line and caustic or no critical lines and caustics. [Schneider & Kochanek & Wambsganss (2006)]

2.2.5 External perturbations

It can be necessary to consider the presence of matter near the lens; this is achieved by embedding a lens into an external shear. This shear is modelled with a potential ψ_γ that is subjected to the following relations

$$\begin{aligned} \gamma_1 &= \frac{1}{2}(\psi_{11} - \psi_{22}) = \text{constant} \\ \gamma_2 &= \psi_{12} = \text{constant} \\ \kappa &= \frac{1}{2}(\psi_{11} + \psi_{22}) = \text{constant} \end{aligned} \tag{2.11}$$

and therefore it has the general form

$$\psi_\gamma(\vec{x}) = Cx_1^2 + C'x_2^2 + Dx_1x_2 + E \tag{2.12}$$

After differentiation, imposing $k = 0$, we obtain the following

$$\psi_\gamma(x, \phi) = \frac{\gamma}{2}x^2 \cos 2(\phi - \phi_\gamma) \tag{2.13}$$

where ϕ_γ defines the direction of the external shear.

2.2.6 Other models

Several mass profiles have been introduced to model gravitational lenses; among them, we briefly describe two models.

Navarro, Frenk and White model NFW

This model is defined by the density profile of dark matter halos, obtained with simulations performed in the Cold Dark Matter paradigm

$$\rho(r) = \frac{\rho_s}{(r/r_s)(1 + r/r_s)^2} \tag{2.14}$$

in the mass range 3 x $10^{11} \lesssim M_{vir}/(h^{-1}M_\odot) \lesssim$ 3 x 10^{15}. With r_s being the scale radius and ρ_s being the characteristic density of the halo. An important feature of the model is the capability of producing radial arcs, as observed in galaxy clusters, since it can have a radial critical line.

Pseudo-Isothermal Elliptical model

This model is obtained starting from the Isothermal model, already considered, and adding a core and a cut radius to the density profile

$$\rho(r) = \frac{\rho_0}{(1 + r^2/r_{core}^2)(1 + r^2/r_{cut}^2)} \tag{2.15}$$

with r_{core} that is the core radius, while r_{cut} is the cut radius ($r_{cut} > r_{core}$). Instead, in the numerator ρ_0 represents the central density, which is related to the central velocity dispersion (1D). Analysing the surface density profile, it appears to be equal to the difference between two NIS lenses. This model is important because it can describe mass distributions on galaxy and galaxy cluster scales.

2.3 Strong lensing by galaxies

Gravitational lensing is nowadays widely used to study the matter distribution inside of galaxies and galaxy clusters.

2.3.1 Scale of the events

The scale of a strong lensing event can be described with the size of the critical lines since the strong lensing effects arise near them. For example, extended sources overlapping the caustics generate multiple images, through the critical lines, which merge to form gravitational arcs. Even if galaxies are not axially symmetric, we can still use the Einstein radius, the size of the tangential critical line for an axially symmetric lens, to quantify the size of the lens. More specifically, we consider an equivalent Einstein radius

$$\theta_{E,eq} = \sqrt{\frac{A}{\pi}} \tag{2.16}$$

that is the radius of a circle that has the same area bounded by the lens critical line.

For galaxies with masses around $\sim 10^{11} - 10^{12} M_{\odot}$ the Einstein radius will have a size of about ~ 1".

2.3.2 Cross-section and optical depth

The cross section is defined as the solid angle within which a source has to be, in order to produce a detectable signal. In the case of microlensing, the cross section is the area contained inside of the Einstein ring; this definition can also be applied to multiple images produced by galaxies modelled as SIS. In the case of point sources, the cross-section for multiple images generated by the strong lensing of galaxies is the area enclosed by the caustics. The cross section for multiple images is small, few squared arcsecond, and therefore strong lensing by galaxies is difficult to detect. This situation is even further complicated by the fact that galaxies often lens only one source.

The probability that a source is lensed by a foreground galaxy requires a model for the distribution of these galaxies behaving as lenses. Usually, the luminosity function of local galaxies, assuming that the comoving density of galaxies is not evolving with the redshift, is used as a starting point. The distributions of galaxies in luminosity are well-described by the Schechter function, which is defined by three parameters that depend on the wavelength of the observations and the type of galaxy that is observed. As discussed before, it is the mass, not the light, that defines the lensing properties; therefore, Maoz and Rix (1993) assigned a mass-to-light ratio to the galaxies and to the properties of the lenses. Unfortunately, this attempt was not successful, and another approach was considered: converting the luminosity function into a velocity function. Even this method presented several disadvantages, and so it was clear that the mass scale of the lenses should not be imposed through local observations but rather obtained from the observed separation distribution of the lenses.

Another important quantity for any statistical analysis is the optical depth: the portion of the sky in which the presence of a source is followed by specific effects. To estimate the optical depth, we need to consider all the lens galaxies in between the observer and the source. As always, for simplicity, we consider the case of a SIS lens

$$\tau_{SIS} = \int_0^{z_s} \frac{dV}{dz_l} dz_l \int_0^{\infty} \frac{dn}{d\sigma_v} \frac{\sigma_{SIS}}{4\pi} d\sigma_v \tag{2.17}$$

where dV/dz_l represents the comoving volume element per unit redshift and $dn/d\sigma$ is the comoving density of lenses per unit dark matter velocity dispersion.

2.3.3 Lensing galaxies

Galaxies can deflect, along the line of sight, the light coming from a distant source. It is important to introduce this family of astrophysical objects, which is usually divided into types according to morphology: early-type galaxies (ellipticals) and late-type galaxies (spirals). This classification is based on the Hubble sequence represented in figure 2.13.

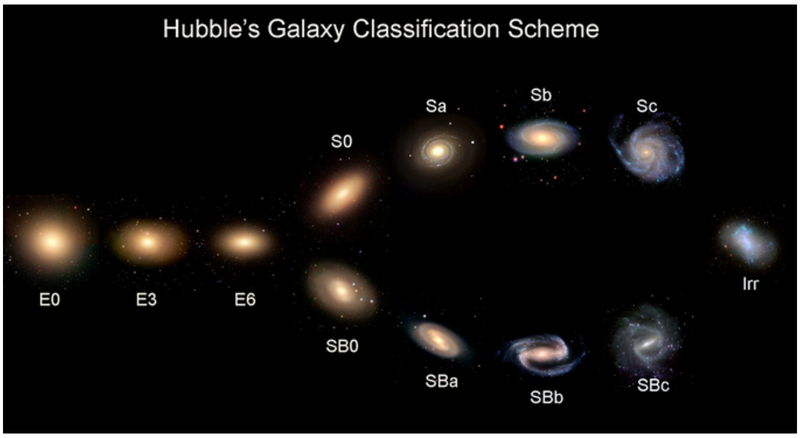

Figure 2.13: Tuning fork diagram that represents the Hubble classification of galaxies. On the left side there are the early-type galaxies, while on the right side there are the late-type galaxies. Credit: Zooniverse [Zooniverse (2026)]

Elliptical galaxies have old stellar populations and no significant star formation; indeed, their spectra are characterised by absorption lines from old stars and the absence of emission lines. The mass distributions of early-type galaxies, accordingly red, are described by standard NFW halos and present a coherence between total mass and light. These galaxies are pressure-supported and also lack an important amount of dust or gas. On the other end, spirals present significant star formation, and their mass distribution is decomposed into three components: the disk, the bulge, and the halo.

Contribution, to the total mass, of each component cannot be obtained using only kinematic data; this problem is known as *disc-halo degeneracy*. To address this issue, we can consider the additional mass constraints obtained through lensing. The efficiency of strong lensing for spirals is strongly related to the inclination of galaxies: in fact, the inclination can modify the projected mass density. As a conclusion, among lensing galaxies we find more ellipticals than spirals, since the number of early-types dominates at high masses.

2.3.4 Lensed sources

There are several astrophysical objects whose light rays can be lensed by galaxies. Now, we focus on a brief introduction of some of these sources in order to highlight their physical characteristics. To describe these sources, the most important features are the luminosity functions and source shapes. Starting from galaxies, we can divide them into two classes: unobscured star-forming galaxies and dust-obscured star-forming galaxies (DSFGs). The former are characterised by a blue continuum with absorption lines produced by the gas in the vicinity of the star-forming regions, while the latter are among some of the most active star-forming galaxies. Indeed, DSFGs present star-forming regions that can be studied through the far-infrared emission: the light from these regions is absorbed by dust and re-emitted in the UV band. The peculiarity of DSFGs is that without lensing, a large number of them would have very small fluxes. However, there are more sources that can be lensed, an example is represented by quasars with their multi-wavelength emission. Other important sources are transients, such as: supernovae, Fast Radio Bursts (FRBs), Gamma Ray Bursts (GRBs) and gravitational waves.

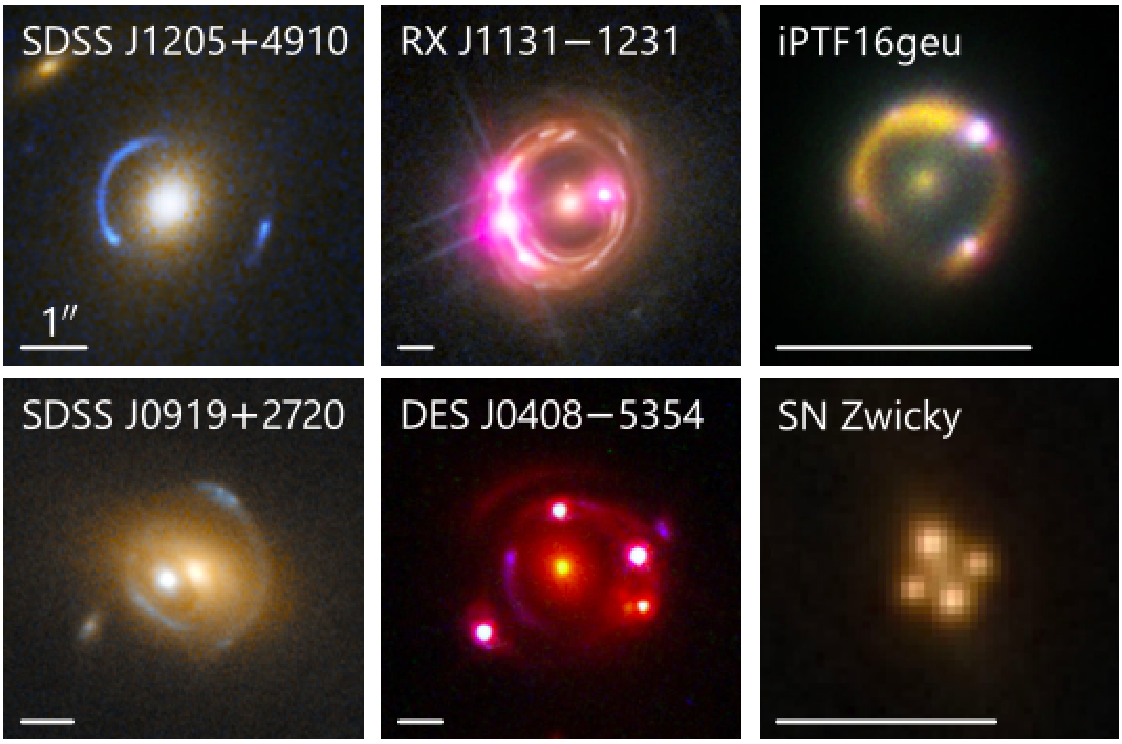

Figure 2.14: Examples of gravitational lenses in which a galaxy is deflecting the light coming from a background source. In bottom left side of each image, a white line represents 1”. The images, created with multi-band HST imaging, are divided in columns according to the type of background sources. The first column displays two lenses with background galaxies, the second column displays two lensed quasar systems and the last column displays two lensed supernovae. The image of RX J1131-1231 is obtained combining also the Chandra X-ray data while the image of iPTF16geu is produced using Keck Observatory IR imaging. Credit: NASA, ESA, A. Bolton, the SLACS team, Chandra, A. J. Shajib, W. M. Keck Observatory, T. Li, and J. Pierel [Shajib et al. (2024)]

Different background sources produce different images, this is something we can appreciate in figure 2.14. The case of galaxy-galaxy lenses is represented in the first column, while the other columns represent quads and doubles, produced by quasars or supernovae.

2.3.5 Observational search

After the first serendipitous detections of gravitational lenses, a more systematic approach was applied. Currently, the research is performed using two methods: source-oriented and lens-oriented. To better understand how they are applied, it is useful to consider some examples.

Source-oriented methods

Surveys that use this technique focus on sources that are likely lensed. Examples of surveys that are using this method are the following:

- the *Cosmic Lens All-Sky Survey* (CLASS) that searched for gravitationally lensed compact radio sources. These possible sources were studied using the Very Large Array (VLA), the Multi-Element Radio Linked Interferometer Network (MERLIN) and the Very Long Baseline Array (VLBA). The number of strong lenses identified by this survey is 22.

- the search, in the sub-mm band, was performed in the context of the *Herschel Astrophysical Terahertz Large Area Survey* (H-ATLAS). This lens search exploited the magnification bias effect to detect dusty star-forming galaxies (DSFGs) that undergo lensing by foreground galaxies. The magnification bias effect can be introduced considering that the observed cumulative source number density is changing due to lensing: the source fluxes and the space between sources are magnified. Because of this effect, sources with flux greater than ~ 100 mJy are expected to be lensed.

The majority of lenses have been found with this approach, since the number of targets that need to be observed is smaller. Considering that the typical cross section for a lens galaxy is $\pi\theta_E^2$; if we search N lenses to detect a lensed source, we would expect to find $N\pi\theta_E^2\Sigma_{source}$ lenses where Σ_{source} defines the surface density of detectable sources. Instead, searching for N sources to detect a foreground lens galaxy, we would expect to find $N\pi b^2\Sigma_{lens}$ lenses where Σ_{lens} is the surface density of lens galaxies. Since $\Sigma_{lens} \gg \Sigma_{source}$, we need to observe a smaller number of sources than lens galaxies to reach the same number of lensed systems. The methods for finding sources that are lensed by a foreground galaxy are several, each with advantages and disadvantages. The first possibility is represented by redshift surveys that can lead to the detection of spectral features from any lensed images. Obviously, these images must be within the aperture that is used to obtain the spectrum. According to theoretical estimates, we should discover one lensing event per $10^4 - 10^5$ redshift measurements.

An important approach, to minimise the follow up observations, is to look for high redshift radio lobes with optical signals of non-stellar origin. They represent excellent candidates since radio lobes are not characterised by an intrinsic optical emission. Even if several lensing events have been discovered with this technique, it is limited by the low angular resolution of all sky radio surveys (like FIRST and NVSS). Most surveys focus on optical quasars or radio sources because they are present at relatively high redshifts. In the case of optical quasars, we work with bright sources, which is a positive aspect, which can possibly mask the lens galaxy, which is a disadvantage. However, there is a common issue for all surveys: it is important to understand the method used to identify the sources. More specifically, in a catalog we need to know if the source flux refers to the total flux of all the images or only a part of the flux. This consideration is going to affect the statistical corrections for using a flux-limited catalog and is named as "magnification bias". Instead, to determine the lens separations that we can appreciate, we need to consider the selection function of the observations that is a combination of: the resolution, the dynamic range, and the field of view. This function can be used to quantify the cost of any follow up observations.

Lens-oriented methods

Surveys that use this approach focus on the detection of lenses rather than lensed sources. Examples of surveys that are using this method are the following:

- the *Sloan Lens ACS* (SLACS) survey considers sources with several galaxies along the line of sight. This selection was performed by looking at the spectra of sources from the Sloan Digital Sky Survey (SDSS). The targets were then observed using the Advanced Camera for Surveys (ACS) of the Hubble Space Telescope (HST). The higher spatial resolution of this instrument is crucial for detecting multiple images and arcs, especially with multi-band imaging. The SLACS survey identified about 150 lenses and possible lenses, some of them can be appreciated in figure 2.15, and among them the majority are elliptical galaxies (80%).

- the surveys like the *Strong Lensing Legacy Survey* and the *Survey of Gravitationally lensed Objects in Hyper-Suprime-Cam Imaging* (SuGOHI) identified tens of lenses and possible candidates. In this case, specific software, arc or ring finders, were used to identify blue features surrounding red galaxies.

- the surveys like the *Kilo-Degree-Survey* (KiDS) and the *Dark-Energy-Survey* (DES) that covered thousands of square degrees of the sky. These surveys highlighted the possible importance that Artificial Intelligence can have in the identification of gravitational lenses.

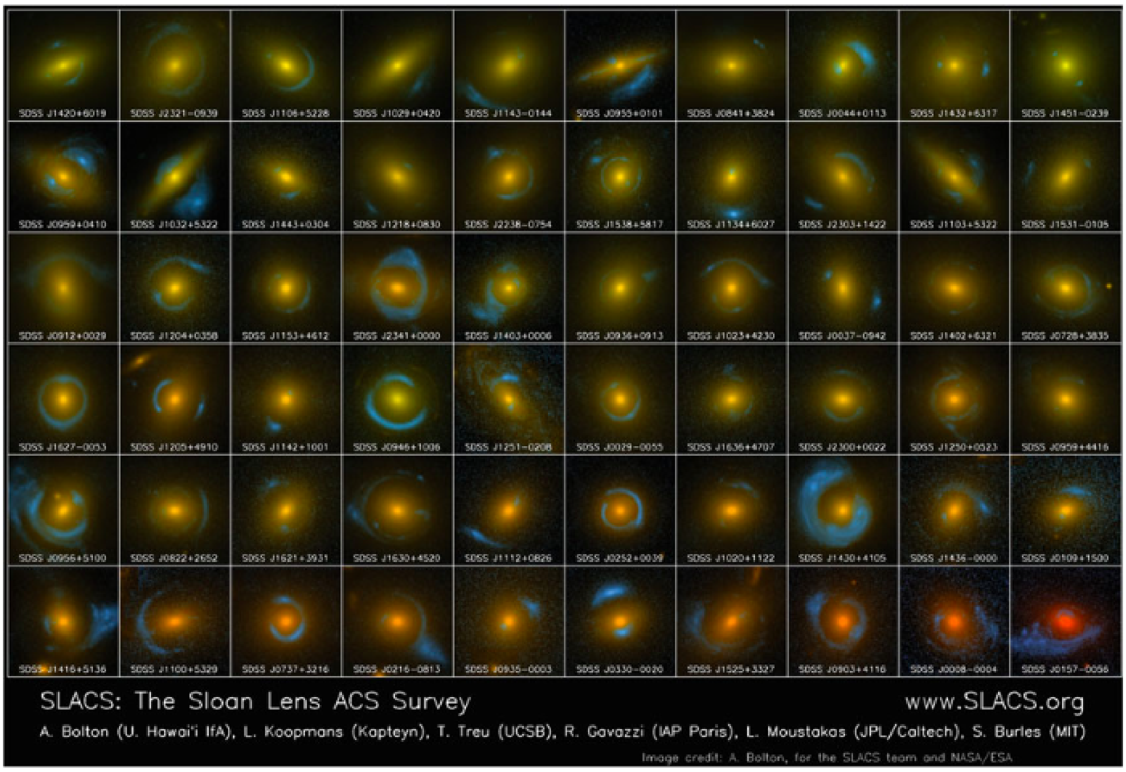

Figure 2.15: Images of 60 gravitational-lens galaxies, organised from the upper left in order of increasing distance of the foreground galaxy from the Earth, obtained with the Hubble Space Telescope. These images, of lenses discovered by the SLACS survey, are colour-enhanced: the foreground galaxy is represented in yellow to red while the background galaxy, with its distorted features, is in blue.[Schneider & Kochanek & Wambsganss (2006)] Credit: A.Bolton (UH/IfA) for SLACS and NASA/ESA [Bolton et al. (2006)]

2.3.6 Reconstruction of the lens mass distribution

The mass distribution of a lens is an important feature that we can reconstruct starting from some constraints. For example, the most accessible constraints are the **positions of multiple images**, which are obtained thanks to deep, high-resolution imaging data. These positions are essentials to probe the lens's deflection field, so the first derivatives of the lensing potential. In the optical and the near-infrared bands we acquire these constraints using the Hubble Space Telescope and its cameras: the Advanced Camera for Surveys (ACS) and the Wide-Field Camera3 (WFC3). At the same time, images with sufficiently high resolution can be acquired also via adaptive optics (AO) from the ground: this system, by correcting the wavefronts for the atmospheric effects, is able to produce images with nearly diffraction-limited point-spread-function (PSF).

Instead, to probe higher-order derivatives of the lensing potential, we need to study the **fluxes and shapes of multiple images and gravitational arcs**. This information is crucial because it is sensitive to small-scale mass substructures that can alter images of extended sources. However, to acquire these constraints follow-up observations of the lenses are needed and they usually require a considerable telescope time.

Alternatively, to probe directly the lensing potential we need the **relative time delays between multiple images**, but they are usually difficult to measure: we need a source intrinsically variable, such as quasars or supernovae, that is followed right after its discovery. From these observed constraints, we obtain the mass distribution of lens; this process is called *lens inversion* and can be performed according to specific algorithms: the parametric or non-parametric algorithms.

2.4 Applications

The strong lensing produced by galaxies is a powerful tool that has a wide variety of astrophysical applications. Here we consider briefly some of them. First of all, strong lenses on the galaxy-scale are important for **revealing the properties of the deflector galaxies**, which are usually elliptical galaxies at $0.1 \lesssim z \lesssim 1$. In the near future the upcoming deep sky surveys could possibly discover other type of galaxies behaving as deflectors. Among the features of galaxies that we can study with lensing, we find: the galaxy mass density profile, the baryonic mass profile, the dark matter profile, the stellar initial mass function, and constraints on central densities and SMBH mass.

Moreover, the physical properties of lens galaxies are useful for **measuring masses**. More specifically, the mass within the Einstein radius is one of the most precise mass measurements for distant galaxies and supports the presence of dark matter within galaxies, since the value of the mass is not entirely described with stars and gas. Indeed, through lensing, we can state that stars do not represent the entire mass density that is located near the lensed images. Outside of the Einstein radius it is more difficult to define the mass distribution and therefore we need to combine different methods, such as the observations of the stars motions within the lens galaxy, in order to obtain the full density profile of a lens galaxy. While offering a unique way to measure masses, lensing also supports the idea that stellar populations vary from one galaxy to another, a quantitative study in that regard needs to be performed in the future.

Instead, finer details in the mass distributions of lens galaxies are important to investigate the possible **presence of substructures**, which can induce specific anomalies. According to the standard cosmological model, cold dark matter (CDM) is the dominant matter component in the universe. This matter, detected only through gravitational interactions with ordinary matter, can be found in dark matter halos that are forming under a *bottom-up* framework: more massive dark matter halos are produced via merging from the smaller ones. Therefore, large dark matter halos contain sub-halos and are characterised, according to simulations, by the NFW density profile. In this context, gravitational lensing has emerged as a powerful tool to test the predictions of the standard cosmological model: until now there has not been a discrepancy with this paradigm. For example, possible substructures in a lens, detected even if they are dark, produce specific lensing effects that are identified through the fitting of extended images with smooth mass distributions. This approach, known as *gravitational imaging*, detects substructures in source-subtracted images and estimates their masses by adding perturbations in the lens model. A valid alternative is also represented by the characterisation of anomalous image fluxes of multiply imaged point sources.

Strong gravitational lensing by galaxies is expected to trace the dark matter in the galactic halos: measuring masses and spatial distribution within the clusters. The mass distribution of these massive clusters is well described by the NFW profile, as confirmed by the Cluster Lensing And Supernova Survey with Hubble (CLASH), and the relation between concentration and mass is consistent with the standard cosmological model. In the CDM framework, dark matter particles have negligible self-interactions and strong lensing helped putting constraints on their cross-section. Strong and weak gravitational lensing are important to define the distribution of baryons and dark matter in cosmic structures; but they need to be compared to complementary data, such as the stellar and the galactic kinematics. In this way we can explain the complex interplay between dark matter and baryons; with the latter that condense inside of halos to form stars. This star formation mechanism can be investigated via strong lensing that can estimate the amount of dark matter, with respect to the total mass, that is contained within the Einstein radius. In this way we can obtain also the mass-to-light ratios inside of galaxies and clusters. Indeed, lensing may be crucial in the determination of the fundamental properties of dark matter particles, since it is able to detect small-scale structure in a unique way.

Another important application is the use of lensing to **study dusty star-forming galaxies (DSFGs)**, since these galaxies are crucial for understanding more about galaxy evolution. Several bright DSFGs are seen through lens galaxies. Using lensing, we can discover the intrinsic properties of DSFGs with a high effective resolution.

Finally, lensing can be used as **a probe of the global geometry of the universe**, with gravitational lens time delays used to constrain cosmological parameters. Indeed, time delay cosmography, involving different physics and data, is an important complement to cosmological probes such as the Cosmic Microwave Background and Type Ia supernovae.

2.4.1 Cosmological applications

Strong gravitational lensing is a powerful tool that, mapping the distribution of matter in galaxies, is used to address specific questions in cosmology and astrophysics. Cosmological applications of this phenomenon are possible since lensing, depending on the distances of lenses and sources, is strongly related to the geometry of the universe. Specifically, the curvature of the universe depends on the cosmological parameters; moreover, the lensing effects produced by galaxies depend on their internal structure. Another important relation is the one between the abundance of lenses and the epoch of their formation: studying the frequency of gravitational lensing events, we can constrain cosmological parameters. Now, we focus on some cosmological applications of gravitational lensing by galaxies.

Cosmic telescopes

Current telescopes have important limitations in the detection of distant sources and, therefore, gravitational lenses offer a powerful alternative. The observation of distant sources represents a way to study the early phases of star and galaxy, formation, and evolution. For instance, stars and galaxies within the first 1 billion years after the Big Bang appear too faint to be detected, therefore, only lensing can efficiently deliver samples of high-redshift sources.

Time delay cosmography

The total time delay, measured in lensing events with multiple images of a variable source, is connected to cosmological parameters through the time delay distance. In particular, time delays are inversely proportional to the Hubble constant H_0 at the present time, which measures the current expansion rate of the universe. The main limitation is represented by the amount of time, usually years, needed to monitor multiple images and sample light-curves of the individual images.

These measurements are currently performed by the COSmological MOnitoring of GRAvItational Lenses (COSMOGRAIL) which is focusing on optical light curves; the aim is to obtain time delays with an accuracy below 3%. The value of H_0 obtained by the COSMOGRAIL's Wellspring (H0LiCOW) collaboration is $H_0 = 73.3^{+1.7}_{-1.8}$ km s^{-1} Mpc^{-1}, within the ΛCDM model, which is consistent with the value ($H_0 = 74.03 \pm 1.42$ km s^{-1} Mpc^{-1}) measured by the SH0ES (Supernoave, H0, for the Equation of State of Dark Energy) collaboration. These latter values, obtained using Type Ia supernovae as standard candles, differ from those based on the Cosmic Microwave Background measurements; therefore, there is a tension in the measurement of H_0.

Strong lensing cosmography

Strong gravitational lensing can also exploit the dependence of the deflection angle on the ratio D_{LS}/D_S to constrain cosmological parameters. This approach can be illustrated using a SIS lens for which the Einstein radius scales as

$$\theta_E \propto D_{LS}/D_S \sigma_0^2 \tag{2.18}$$

where D_S and D_{LS} are the angular diameter distances, while σ_0 represents the velocity dispersion. The idea is that measuring this radius from the positions of multiple images of two sources, at different redshifts, we obtain a second estimate of the Einstein radius. Moreover, their ratio depends only on cosmology because it is only related to the angular distances.

2.4.2 Current state and future prospects

Lens statistics, focusing on the CLASS flat spectrum radio survey, is useful to estimate the cosmological model. The results are obtained applying the maximum likelihood methods that lead to conclusions consistent with the estimates from Type Ia supernovae. However, the CLASS survey presents several problems that can limit our results; first of all, the lack of information regarding the redshift distribution of the lenses and also the lack of studies that treat adequately the lenses with satellites or associated with clusters. Lens statistics can also be applied to constrain dark energy, but larger samples are needed.

The future of strong lensing, with its possible applications, is connected to the expansion of the sample of lenses available. Lensing could be used to map out the halo mass function, since this method works uniformly on dark halos, galaxies, and clusters. The effects produced by lenses are distinguished on the basis of mass rather than luminosity; therefore, the same approach works for all halos: the halo mass function could be mapped through the separation in the distribution of lenses. The dependence on the mass could be exploited also to study the evolution of galaxies with redshift over optically-selected samples, where the selection is different at low and high redshift. The VLA and Merlin radio arrays are crucial for achieving this goal. Instead, to improve the knowledge regarding the mass distributions of lenses, we need to measure accurately time delays, and so systematically monitor the variability of several lenses. Using lensing it could be possible to measure the central surface densities of galaxies and look for supermassive black holes; both of these goals can be achieved through ultra-deep, high-resolution radio maps of lenses. Expanding the sample of lenses and data, it may be possible to identify univocally dark satellites, so satellites without an optical counterpart. Another future application of lensing is represented by the measurement of the kinematics of distant host galaxies. This step is a consequence of the lens magnification that simplifies photometric studies of a lensed quasar host galaxy, with respect to an unlensed galaxy.

Chapter 3

Connection between galaxies and dark matter halos

3.1 Dark matter

Dark matter represents an important open question in both cosmology and particle physics. By dark matter, we mean matter that is not detectable by its emitted or absorbed radiation. Dark matter is usually distinguished between baryonic and non-baryonic; studies of the Cosmic Microwave Background (CMB) and the Big Bang nucleosynthesis suggest that non-baryonic dark matter is dominating. Therefore, from now on we use the term dark matter instead of non-baryonic dark matter.

The characterisation of dark matter is problematic because of its elusive nature; indeed, contrary to baryonic matter, it is considered collisionless. Dark matter is massive and stable over billions of years, and it is distinguished based on its thermal velocity: hot (relativistic speeds), cold (non-relativistic speeds), and warm. Hot dark matter (HDM) is defined by particles of very low-mass, such as neutrinos whose thermal speed at the present time is above 100 km s^{-1}. Since this value is consistent with the speed related to the potential wells of galaxies, neutrinos are not gravitationally bound to galaxies, and therefore galactic dark halos cannot be made of HDM. Instead, cold dark matter (CDM) is made of massive particles, such as the weakly-interacting massive particles (WIMPs), and represents most of the total amount of dark matter. In the end, warm dark matter (WDM) particles have masses in between those of HDM and CDM. All of the different types of dark matter particles are collisionless and can interact only through gravity.

3.1.1 Observational evidence

Dark matter can be detected through observations of gravitational effects at different scales. These detections can be performed using several astrophysical objects; we can start by considering galaxies, especially spiral galaxies in which most of the visible mass is located in the bulge and disk. These galaxies present rotation curves in which the observed velocity far from the center becomes constant; as a consequence the mass is still increasing beyond the observable disk. An additional evidence sustaining the presence of dark matter is represented by the stability of disk galaxies. Also in galaxy clusters there has been the detection of dark matter; in this case gravitational lensing reveals that visible matter can account only for $10-20\%$ of the total mass. Galaxy clusters are among the largest gravitationally bound objects and, therefore, are considered representative of the Universe.

The evidence for dark matter is obtained through the virial theorem, used to compute the total mass, and the baryon fraction considering the hot X-ray emitting gas. In this context, gravitational lensing is a powerful tool to understand the mass distributions of these clusters and, therefore, to prove the existence of dark matter. Moving to cosmological scales, dark matter is able to influence structure formation, more specifically the gravitational attraction that it generates is important to counteract the expansion of the Universe.

3.1.2 Experimental searches for dark matter particles

Dark matter particles are searched by means of several experiments: dark matter direct detections, dark matter indirect detections, and colliders.

Dark matter direct detections

Dark matter particles are continuously crossing Earth, and therefore we can look for them by building large tanks and detectors which can increase the probability of interaction. Indeed, in a year each cubic meter on Earth is crossed by about 10^{13} dark matter particles. This estimate is obtained considering the local density of dark matter in the Solar System, 0.4 GeV/cm^3, and the fact that dark matter is made of particles of masses around 100 GeV.

In order to detect dark matter we can exploit its interaction with standard matter: more specifically the scattering with atoms (nucleons or electrons). The goal is therefore to measure the mass of dark matter and its scattering cross section with nucleons. The development of new technologies will increase the sensitivity of these experiments, and therefore could possibly lead to interesting conclusions.

Dark matter indirect detections

The indirect approach is based on the detection, always performed on Earth, of Standard Model particles, produced by dark matter decay or interaction. These interesting particles are photons, neutrinos, and charged particles. They are affected in different ways by the interstellar and intergalactic media and therefore need to be studied according to different methods.

The searches are concentrated on regions in which dark matter is believed to be denser, such as galaxies. These astrophysical objects have density profiles generally described by a few options: the NFW profile, the Einasto profile, or the Burkert profile.

Particle colliders

Particle colliders, such as the Large Hadron Collider (LHC), offer the possibility to probe new physics scenarios. These instruments rely on the production of new particles through collisions of protons and electrons or by means of decay.

3.2 Dark matter halos

The formation of galaxies is a process that starts with the collapse of gas, and consequent cooling in dark matter halos. Considering the spatially flat CDM cosmological model, dark matter halos are identified as structures with a mean density equal to 200 times the background density of the Universe, and they are described by the NFW profile.

Dark matter and dark matter halos had a crucial role in structure formation, since a Universe with only baryons could not form galaxies. These halos are produced by the development of primordial perturbations in the Universe matter density distribution.

3.2.1 Observational evidence

The idea that dark matter could represent most of the total matter in the Universe was introduced in the 1930s; indeed, Zwicky believed that most of the matter in the Coma cluster was dark matter.

Later, in 1973 Ostriker and Peebles considered the presence of dark matter in galaxies, and finally the existence of dark matter halos was taken into account to explain the observed rotation curves of disk galaxies. Instead, the presence of these halos in early-type galaxies was confirmed by gravitational lenses.

3.2.2 Hierarchical merging

Cold dark matter halos form according to a bottom-up paradigm: smaller systems virialise first, while the larger ones are produced by the accretion of diffuse matter and small dark matter halos. More specifically, dark matter halos growth is generated by the merging of small systems; this formation mechanism is known as **hierarchical merging**. The situation is well described by a tree-shaped diagram, represented in figure 3.1, in which the growth of dark matter halos is reported as a function of time. It is important to note that this representation does not consider the accretion of diffuse matter.

The history of dark matter halos is characterised by several merging events in which we distinguish between major and minor mergers. The former describe a situation in which both mergers have similar masses, while the latter describe the accretion of smaller halos. The parameter that is useful to discern between mergers is the **merger mass ratio**, that is the ratio of the masses of the two systems. Another important parameter is the **halo merger rate**, which represents, at a given time, the probability that a halo with a specific mass merges with another one.

This quantity can be estimated analytically with the Press-Schechter formalism or numerically using N-body simulations.

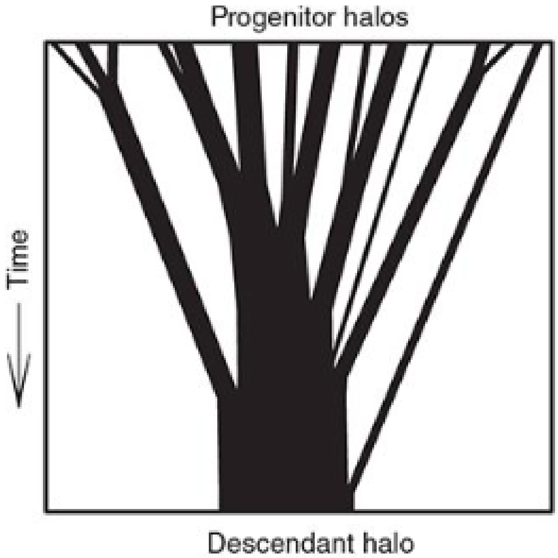

Figure 3.1: Representation of a merger tree which shows the growth history of dark matter halos. In the upper portion of the scheme, the progenitor halos are progressively merging to produce the descendant halo that is reported in the bottom part. This process is represented as a function of the time, which is increasing toward the lower portion of the scheme. [Nipoti & Fraternali & Cimatti (2019)]

3.2.3 Structural and kinematic properties

To study the structure and kinematics of dark matter halos we use cosmological numerical simulations, more specifically dark matter-only cosmological N-body simulations where gravity is the only force in action. These simulations lead to halo merger trees and mass functions, at different redshift; while they also provide the dark matter density distribution, with: elongated structures (filaments), empty regions (voids) and high-density areas (halos).

Density profiles

The density profiles of dark matter halos, obtained through dark matter-only cosmological simulations, do not vary considerably with the mass or from halo to halo, at a fixed mass. Usually we can use two main profiles: the Navarro-Frenk-White, already discussed in subsection 2.2.6, and the Einasto profile. The latter, originally considered for stellar components of galaxies, is described by

$$\rho(r) = \rho_s \exp\left\{-\frac{2}{\alpha}\left[\left(\frac{r}{r_s}\right)^{\alpha} - 1\right]\right.$$

where α is the Einasto index. This profile, contrary to the NFW, is characterised by three parameters and varies as a function of α; with $\alpha \simeq 0.2$ it is similar to the NFW profile. These two profiles are represented in figure 3.2.

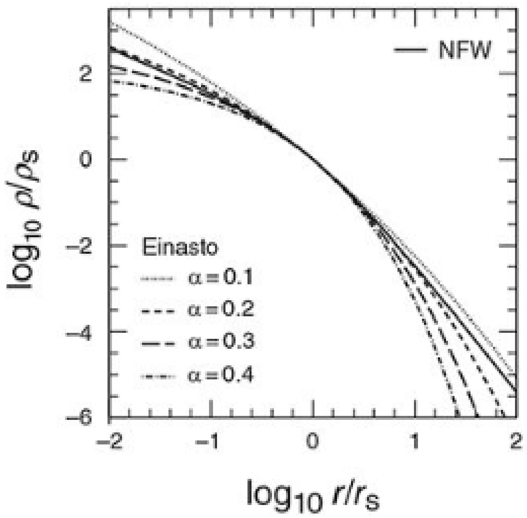

Figure 3.2: Representation of the NFW and Einasto profiles, where the density is expressed as a function of the radius. [Nipoti & Fraternali & Cimatti (2019)]

Shape

Dark matter halo simulations show a significant deviation from spherically symmetric distributions. This situation is produced by the triaxiality of the dark-matter density distribution, on large scales, and the presence of substructures, on small scales. Instead, the presence of baryons and processes like gas cooling leads toward halos with a more spherical shape.

Considering the triaxiality, we take into account isodensity surfaces, which are well described by concentric ellipsoids. These ellipsoids are characterised by their intrinsic semi-axes $c_{int} \leq b_{int} \leq a_{int}$, which are useful to introduce the triaxiality parameter

$$T = \frac{a_{int}^2 - b_{int}^2}{a_{int}^2 - c_{int}^2} \tag{3.2}$$

According to the value of T that describes triaxial halos, we can distinguish between different types of spheroids: oblate ($0 < T < 1/3$), triaxial ($1/3 < T < 2/3$) and prolate ($2/3 < T < 1$). In the context of dark-matter only cosmological simulations, most of the dark matter halos are prolate, several are triaxial, while only a few are oblate.

Another important parameter is the shape parameter, which can quantify the halos deviation from spherical symmetry

$$s = c_{int}/a_{int} \tag{3.3}$$

where s decreases as the mass increases. Instead, on small scales we notice the presence of subhalos, which are basically dark matter halos orbiting around larger halos.

In the case of a massive galactic halo, the subhalos are believed to host satellite galaxies. These substructures evolve through interactions with other subhalos and are characterised by their mass function. In particular, we focus on the unevolved subhalo mass function which represents subhalos masses at the time of accretion; this fundamental property does not depend on the halo mass and redshift.

Therefore, we can express the subhalos number per unit logarithmic mass as

$$\frac{\mathrm{d}n}{\mathrm{dln}\mu} = \gamma\mu^{\alpha}e^{-\beta\mu^{w}} \tag{3.4}$$

where μ represents the ratio between the masses of the subhalo and the host halo, while the other parameters are dimensionless and are defined by specific reference values ($\alpha \approx -0.9, \beta \approx 6, \gamma \approx 0.2, w \approx 3$). It is important to notice that the contribution of the subhalos to the total halo mass, usually about 10%, decreases with the evolution of the system.

Spin

Dark matter halos are pressure-supported systems that acquired an angular momentum during their formation. The non-spherical nature of these structures, combined with the surrounding inhomogeneous matter distribution, gives rise to tidal forces that induce a torque and then a rotation to the halos. The rotation support of the halos can be represented through the spin parameter

$$\lambda = \frac{J\,|E|^{1/2}}{GM_{\triangle}^{5/2}} \tag{3.5}$$

where J quantifies the magnitude of the total angular momentum, E defines the total energy, and $M_{\triangle}$ is the virialized mass of the halo.

The presence of a spin in the halo is crucial for the formation of galactic discs, and it can be increased thanks to the transfer of angular momentum from baryons.

The influence of baryons

The dark halo properties presented so far are obtained using dark matter-only cosmological simulations; but they are not always consistent with observed properties, especially at small scales. As a consequence, we can understand that baryons have important effects on the structure and kinematics of dark matter halos.

First of all, baryons modify the dark matter density profile: it becomes steeper in the central area. In fact, baryons lose energy through dissipation, basically the emission of radiation, and therefore they end up in the central regions of the halos. These baryons inevitably influence the dark matter gravitationally and modify the density distribution; this process is called contraction.

Baryons can also modify dark matter halos in the opposite direction: the net effect of the dynamical friction heating, between baryons and dark matter, is a lower halo density profile in the central regions. Other important events able to modify the dark matter distribution are related to the gas with feedback mechanisms and ram-pressure stripping, which become significative when the galaxy is a cluster. Indeed, the removal of gas modifies the overall gravitational potential.

3.3 Galaxy-halo connection

The formation and evolution of galaxies are directly connected to the growth of the dark matter halos in which they were created. Indeed, dark matter halos are gravitationally bound regions in which matter collapses. The connection between these astrophysical objects can be represented in figure 3.3; with the growth and merging of dark matter halos that impact the properties of galaxies. The galaxy-halo connection is not only related to the masses but includes a wide variety of properties.

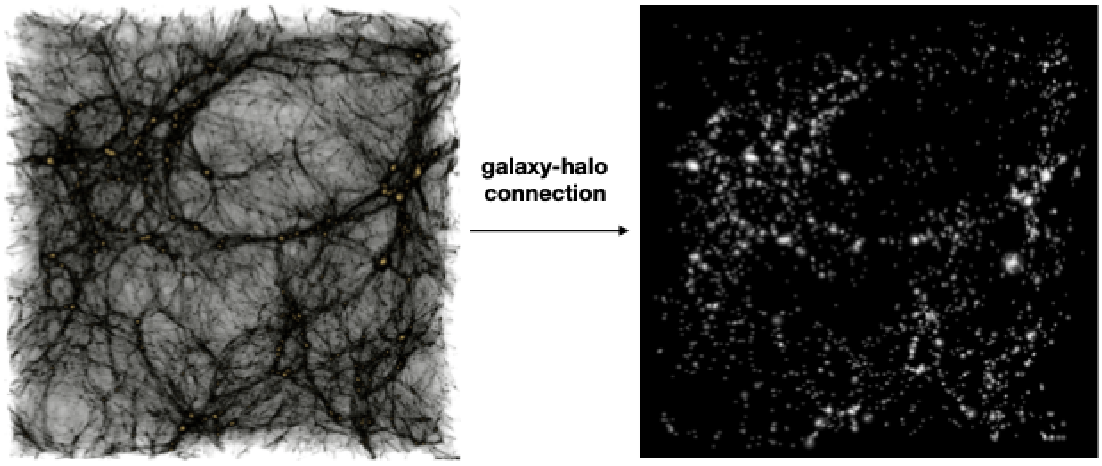

Figure 3.3: In the left panel, there is the dark matter distribution produced by a cosmological simulation in a 90 x 90 x 90 Mpc h^{-1} slice. In the right panel, there is the distribution of galaxies obtained through a model that matches the galaxy clustering properties of an observed sample. [Wechsler & Tinker (2018)]

3.3.1 Modelling

Modelling the galaxy-halo connection is possible by considering two different approaches: empirical and physical modelling.

Empirical modelling

The empirical modelling focuses on data to describe the galaxy-halo connection as a function of time; this method focuses on the reconstruction of the galaxy evolution through observations. Therefore, the model matches the properties at the time in which galaxies are accreted into the host halos. Basically, observations from galaxy surveys are linked to the properties of dark matter halos, which are predicted using N-body simulations.

First of all, we need to specify the assumptions that are usually applied; one of the simplest is that most massive galaxies reside in the most massive dark matter halos. This premise, regarded as a non-parametric technique connecting the stellar and halo mass functions, is called **abundance matching**, and it is important to calculate several statistics for the model. Indeed, abundance matching is used to determine the **galaxy stellar-to-halo mass relation** (SHMR); however, the minimum halo mass that is able to host a galaxy is still uncertain.

Another approach, to clarify the relation between galaxies and dark matter halos, is to consider the **Halo Occupation Distribution** (HOD), which is the probability distribution function (PDF) for the number of galaxies, with specific features, inside of a halo.

Other important tools are the **conditional luminosity function** (CLF) and the **conditional stellar mass function** (CSMF), which are able to describe the distribution of galaxy luminosities for a specific halo mass.

Considering the HOD and the CLF, there are usually two approaches that we can select; the first one is to populate a halo, identified through a simulation which applied the Monte Carlo method, and measure the observables. The alternative is to work with an analytic halo model of dark matter clustering in order to predict, analytically, some statistics. Both models, the HOD and CLF, since they indicate the number of galaxies per halo, are crucial to understand the galaxy-halo connection.

Physical modelling

The physical modelling or theoretical modelling, through simulations and parameterisations of galaxy formation physics, is able to describe the relation between a galaxy and its dark matter halo. This approach is based on **hydrodynamical simulations** and **semi-analytic models** describing the key physical processes involved in galaxy formation. More specifically, hydrodynamical simulations are based on the solution of the equations of gravity and hydrodynamics, focusing on several processes, such as gas cooling, stellar feedback, feedback from black holes, and supernovae. Obviously, these simulations, performed with some parameterisations below the resolution scale, have been able to produce realistic galaxy populations, due to an increase in the resolution and an improvement in several physical models.

Therefore, these models are useful for testing assumptions regarding the current description of empirical models; the negative aspect is that this approach is computationally expensive. Instead, semi-analytic models of galaxy formation are computationally more efficient, since they approximate several physical processes using analytic prescriptions obtained through the analysis of the merging history of dark matter halos. Inevitably, this approach is based on a large number of parameters and uses several simplifying assumptions.

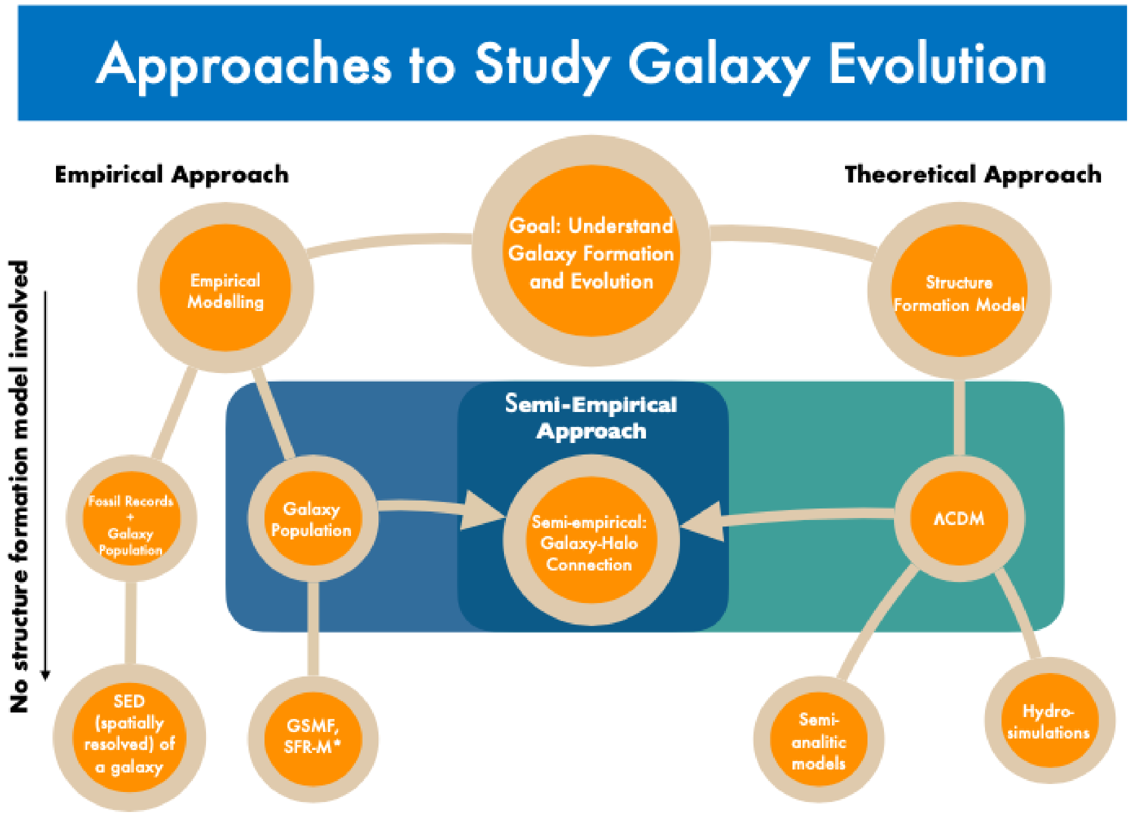

Figure 3.4: Brief graphical representation of the different approaches used to study galaxy evolution. [Rodriguez-Puebla (2024)]

The two approaches are complementary to each other: physical models can test parameterisations and assumptions of the empirical ones, while empirical models can define uncertainties in physical parameterisations. Since they are less computationally expensive, empirical models are used in researches which try to constrain the galaxy-halo connection using cosmological parameters.

3.3.2 Implications

The study of the galaxy-halo connection has several applications, among which we find: the characterisation of the physics of galaxy formation, the estimate of cosmological parameters, and the determination of dark matter properties and distribution.

Characterisation of the physic of galaxy formation

Galaxy-halo connection is crucial to identify the relation between dark matter halos properties and the properties of galaxies that are formed inside of them. Also, empirical models can trace galaxy histories through time, offering useful insight about galaxy star formation histories and quenching. Moreover, the shape of the SHMR is evidence for strong feedback in galaxy formation: the part describing larger masses constrains the AGN feedback strength, while the size of the scatter constrains the types of properties, regarding halo and galaxy, that are related to halo quenching. Instead, an essential test of structure formation is represented by the galaxy merging rates, which are highly sensitive to the galaxy-halo connection.

Estimate of cosmological parameters

Considering clustering measurements to smaller scales will be crucial to define high precision constraints on cosmological parameters. These scales, explored by future surveys, are important for studying the galaxy-halo connection and therefore for characterising the growth of structures and the universal expansion rate.

The starting point is represented by the measurements of projected galaxy clustering, this step is important in order to take into account the effect of the redshift-space distortions (RSDs): the redshifts of galaxies are also influenced by peculiar motions, which are produced by the local gravitational potential. These measurements are analysed using halo occupation methods and can lead to cosmological constraints.

Another important statistic is represented by the mass-to-number ratio of galaxy clusters (M/N), which is similar to the mass-to-light ratio (M/L), but has the advantage of reducing the number of free parameters in the model. Cosmological information is contained in the measurements of the mean occupation; while the ratios M/L and M/N are used to constrain cosmological parameters through data of low-redshift sources.

Currently, simple HOD models are used to produce unbiased parameter constraints, but in the future additional parameters will be necessary. In the context of cosmological information, galaxy-galaxy lensing is fundamental since it is sensitive to matter density and the amplitude of matter fluctuations.

Determination of dark matter properties and distribution

The galaxy-halo connection is a powerful tool to understand and constrain dark matter properties; even if at large scales several attempts have been successful, at small scales there are still a lot of problems. An approach can be that of using statistical modelling to characterise the galactic population of the halo. Indeed, the searches for an indirect detection of WIMP dark matter, through gamma rays, are directly related to a well defined description of the galaxy-halo connection, since we need accurate mass estimates of the galaxy groups. The statistical galaxy-halo connection plays, also, a key role in the description of the Milky Way; with its halo properties constrained using this connection.

3.3.3 Galaxy abundance and halo occupation distribution

There are several measurements that are crucial to describe and characterise the galaxy-halo connection, among them we focus on: the amount of galaxies, the relationship between satellite and central galaxies, and their spatial distribution. The most important constraint, for a given cosmological model, is represented by the stellar mass function (SMF) or the luminosity function, which describe the abundance of galaxies as a function of the stellar mass or luminosity.

The determination of the SMF is now very precise, considering the local universe; and constraints on the evolution of the galaxy SMF have improved, leading to a consequent improvement in our understanding of the galaxy-halo connection. Regarding the spatial distribution of galaxies, it is important to identify in the correct way the number of satellite galaxies as a function of the galaxy mass. Considering abundance matching and SHMR models, seen before, there is no limitation in treating galaxies in the same way within host halos and subhalos. One approach is to constrain central galaxies using the SHMR, while the number of satellites, within an halo, can vary freely; the alternative is to work with two different SHMR describing central and satellite galaxies.

In the context of galaxy abundance it is important to talk about the **halo occupation distribution**; which is the probability distribution function for the number of galaxies, satisfying certain criteria, contained within an halo. This probability distribution, usually conditioned on the mass $P(N\,|M)$, is evaluated in different ways according to the region of the halo that describes: for central galaxies, we consider a Bernoulli distribution, while for satellite galaxies a Poisson distribution is used.

With these premises, the HOD is defined by its mean occupation number $\langle N|M\rangle$, and can also be a function of other properties other than the mass of the halo. In the early 2000s, several studies were conducted with the goal of linking halo occupation models to the data regarding galaxy clustering, and now a wide variety of galaxy samples have been well described. The analyses assumed that the HOD form, for galaxies selected according to mass or luminosity criteria, is similar between dark matter halos and their subhalos, with the latter being well-described by a power law ($N \sim M$), with the inclusion of a central galaxy.

Now, we examine some representative studies that highlight both the potential and the current limitations of the HOD approach.

Clustering of luminous early-type galaxies

As reported in [Zheng et al. (2009)], the clustering of galaxies depends on several galactic properties, such as the luminosity and the morphology, and represents a key element in understanding the galaxy formation. This study focuses on the luminous red galaxies (LRGs) and their clustering activity, which contains information about their environment: usually represented by the central regions of clusters. In this context, the framework of the halo occupation distribution (HOD), and the conditional luminosity function (CLF) approach offer a way to improve the theoretical understanding of galaxy clustering.

The starting points are the probability distribution $P(N\,|M)$ that a halo, with mass M, contains N galaxies that satisfy a specific criterion, and the velocity distributions of galaxies contained within the halos. The HOD/CLF method has been used, with great results, to study galaxy clustering in several surveys. In this situation, for the HOD parametrization it was useful, since not all LRGs are central galaxies in clusters, to distinguish the contributions from central and satellite galaxies: the CLF form is used for the distribution of central LRGs, while the HOD form is considered for the satellite LRGs.

This research had the goal of studying the mean relation between the luminosity of central LRGs and the halo mass, characterising the satellite occupation function, and determining the amount of L_* galaxies contained in massive halos. In this case, the HOD of LRGs, modelled with five parameters, is consistent with those obtained in several recent studies. More specifically, this LRG modelling is able to relate, at $z \sim 0.3$, massive galaxies and dark matter halos, thus it represents a powerful tool to test models describing the formation of massive galaxies. Nevertheless, there is a discrepancy between the LRG HOD observed and the one theoretically predicted; this systematic effect is the manifestation of the limitations of the semi-analytic galaxy formation model.

The possible application of the HOD of LRGs is not only limited to tests of the galaxy formation but can also be extended for studying cosmological parameters. The results obtained highlight that, in massive halos, the distribution of L_* of galaxies is roughly consistent with that of dark matter; and the mean occupation number is scaling as $M^{1.5}$ where M is the halo mass. Therefore, the more luminous LRGs appear to be more clustered, and massive clusters should contain numerous LRGs.

Halo occupation number and limitations

The halo occupation number is described in the work of [Peacock & Smith (2000)].

The distribution of galaxies within the halo depends on the efficiency of the galaxy formation and the location of the galaxies. Galaxy formation is considered through the halo occupation number, and therefore using the luminosity function; instead, for the positions, we assume that one galaxy defines the halo center while the others, acting as satellites, are used to trace the mass of the halo.

As introduced before, the formation of galaxies is a non-local process with the cooling of baryonic matter within virialised dark matter halos. Models that study the galaxy density field focus on the halo occupation number, which affects the bias on intermediate scale correlations between properties of galaxies and dark matter. Numerical models describing galaxy formation try to determine the number of galaxies that form within a specific halo; this information can be obtained as well considering empirical observations. Then, the number of galaxies in the halo can be converted into the total stellar luminosity, which is crucial to determine the All Galaxy Systems (AGS) luminosity function. The AGS luminosity function is a quantity that can trace, as a function of the total luminosity, the distribution of gravitationally bound galaxy systems.

The process of constraining the clustering of galaxies presents several issues that can limit the results, such as the fact that the galaxy distribution is biased, the high sensitivity of the small-scale correlations of galaxies to their distribution inside the halo, and the dependence of the amplitude of the small-scale clustering on the amount of "isolated" galaxies.

Galaxy evolution

The formation and evolution of galaxies can be studied considering their spatial clustering; more specifically, we can model, at different redshifts, the luminosity dependence of the galaxy two-point correlation functions. This approach is used in the work of [Zheng et al. (2007)], where the redshift values that have been considered are: $z \sim 1$ with the sample of galaxies from the DEEP2 Galaxy Redshift Survey and $z \sim 0$ with galaxies from the Sloan Digital Sky Survey (SDSS). The idea of comparing galaxy clustering at different redshifts provides a lot of crucial insights on galaxy evolution; but it is worth recalling that it is not a simple task since the surveys have different sample selections.

As is well known, the evolution of galaxies is related to that of dark matter halos; in this context, the HOD offers a framework in which we can infer, starting from galaxy clustering data, the statistical relation between these structures. The study of the HOD evolution could be useful in improving our understanding of the evolution of baryons in galaxies, and it is also an approach that lets us study the time evolution of galaxy properties as a function of the host halo mass. This strategy leads to important constraints on galaxy evolution and star formation over the past $\sim$ 7 billion years. With respect to this model, the parameterisation is a key aspect, and it has been proved that the optimal choice is to separate the description of central and satellite galaxies. Indeed, the mean occupation function, defined by five parameters, is described using two components:

- the **mean occupation function of central galaxies** that is a steplike function

$$\langle N_{cen}(M)\rangle = \frac{1}{2}\left[1+\mathrm{erf}\left(\frac{\log M - \log M_{min}}{\sigma_{\log M}}\right)\right] \tag{3.6}$$

  where erf represents the error function

$$\mathrm{erf}(x) = \frac{2}{\sqrt{\pi}}\int_0^x e^{-t^2}dt \tag{3.7}$$

  Therefore, for central galaxies we can identify two parameters: the lower mass limit M_{min} for halos that host central galaxies above the luminosity limit, and $\sigma_{\log M}$ which represents the profile spread.

- the **mean occupation function of satellite galaxies** which, with the same cutoff profile considered for central galaxies ($M > M_0$), is described by

$$\langle N_{sat}(M)\rangle = \frac{1}{2}\left[1+\mathrm{erf}\left(\frac{\log M - \log M_{min}}{\sigma_{\log M}}\right)\right]\left(\frac{M-M_0}{M_1'}\right)^{\alpha} \tag{3.8}$$

  where there are three parameters: M_0 is the mass at which there is a drop of the function, M_1' defines the amplitude, while α is the asymptotic slope in the high-mass end.

This HOD parameterisation leads to the two-point correlation function, which on small scales reflects the galaxy distribution inside halos. The mean occupation functions obtained from the DEEP2 survey samples are represented in figure 3.5a, while the results obtained from the SDSS are shown in figure 3.5b.

The comparison between data from these different surveys is made more complex by the fact that galaxies have been selected in different rest-frame bands. Among the results, we find that central galaxies, at a fixed halo mass, are usually more luminous than satellite galaxies, and therefore luminous galaxies are far more likely to be central galaxies in low-mass halos than satellite in high-mass halos. Moreover, galaxies are usually dimmer than their progenitors; this was expected since stars decrease in brightness with age.

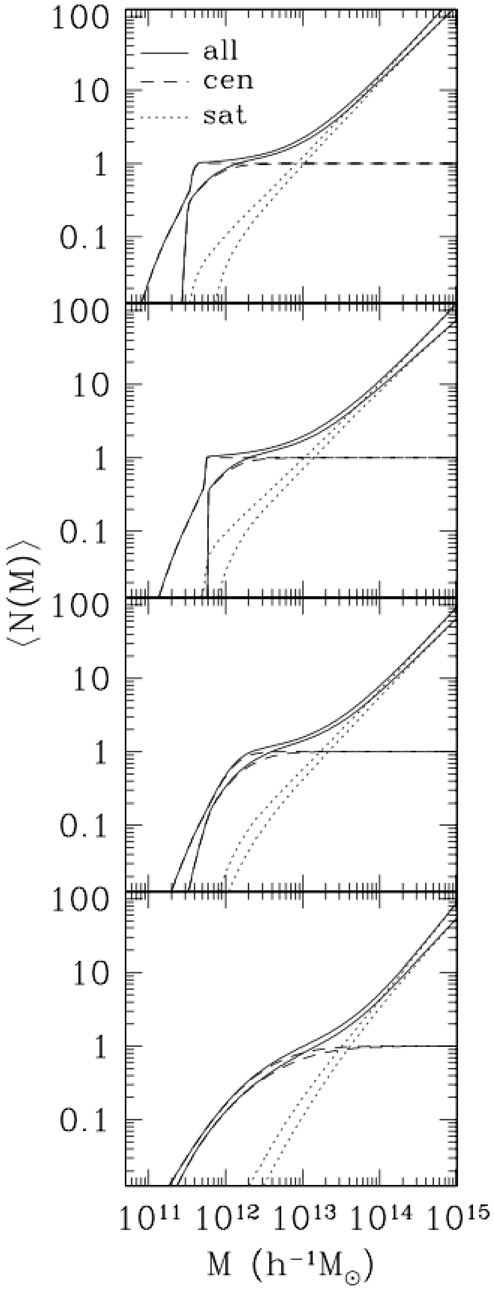

(a) Mean occupation functions obtained considering samples from the DEEP2 survey. [Zheng et al. (2007)]

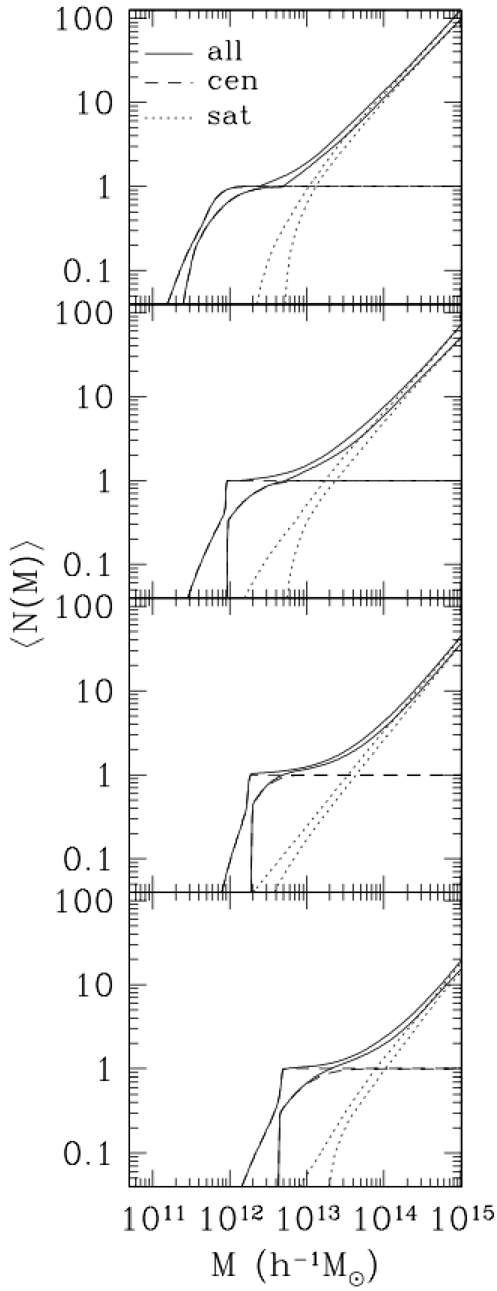

(b) Mean occupation functions obtained considering samples from the SDSS survey. [Zheng et al. (2007)]

Figure 3.5: Comparison between the mean occupation functions obtained using DEEP2 and SDSS survey samples. More specifically, there are four different samples, which are divided according to specific magnitude ranges ($M_B < -19.0$; $M_B < -19.5$; $M_B < -20$; $M_B < -20.5$). In the two series of plots, the mean occupation functions are also divided between the contributions from central and satellite galaxies. We can notice a trend: as the luminosity increases, the mean occupation function moves to a higher value of the halo mass.

Chapter 4

Dataset description

4.1 Description of the Euclid Mission

Euclid is a space mission of the European Space Agency (ESA) which, through weak gravitational lensing and galaxy clustering, has the goal of studying dark matter and dark energy. Euclid will perform, from the Lagrangian point L2 referring to the Sun-Earth system, a wide area imaging and spectroscopic survey in the visible and the near-infrared. The Euclid Wide Survey (EWS) observations started on 14 February 2024 and in 6 years they will survey the sky for about 14 000 $\deg^2$. This survey will be crucial to expand the knowledge in many astrophysical fields, such as the accelerated expansion of the Universe and dark energy. The EWS has an average limited magnitude of 24.5 mag in the near-infrared bands (Y_E, J_E, H_E) and 26.5 mag in the visible (I_E). During this time, Euclid will also conduct an additional deep survey (DS) covering about 40 $\deg^2$, to study dimmer objects in smaller areas and provide calibration data for the EWS.

This mission, thanks to high-resolution and a wide-area approach, represents an unparalleled instrument for identifying strong gravitational lenses; indeed, it will resolve about 1.5 billion galaxies in the next ten years, which will correspond to the identification of 100 000 galaxy-galaxy strong lenses. Considering Euclid's point spread function, it is able to resolve even lenses with Einstein radii of about $0''.5$; in that regard, ground-based telescopes are usually limited to $1''.0$. To better appreciate the peculiarity of the Euclid mission, we can compare its specifics with the one of the surveys used to find lenses before, as reported in figure 4.1.

Instrument	PSF Seeing	Field-of-view
DECam (DES, 620 nm)	0″.9	10 800′
HSC (Wide, 620 nm)	0″.7	6480′
HST WFC3 (700 nm)	0″.07	7′.3
JWST NIRCam (700 nm)	0″.03	9′.7
Euclid VIS (700 nm)	0″.16	1900′

Figure 4.1: This table reports the PSF, or seeing for ground-based telescopes, and the field-of-view of Euclid VIS, and the other instruments used to find lenses. [Euclid Collaboration (2025)]

More specifically, this space telescope is capable of performing high-resolution imaging in the optical and near-infrared part of the spectrum. These details make Euclid the best-performing instrument in the search for strong lenses ever built; indeed, the rate at which this mission detects lenses is between 10 and 100 times higher than what has been accomplished in recent surveys, as we can see in figure 4.2.

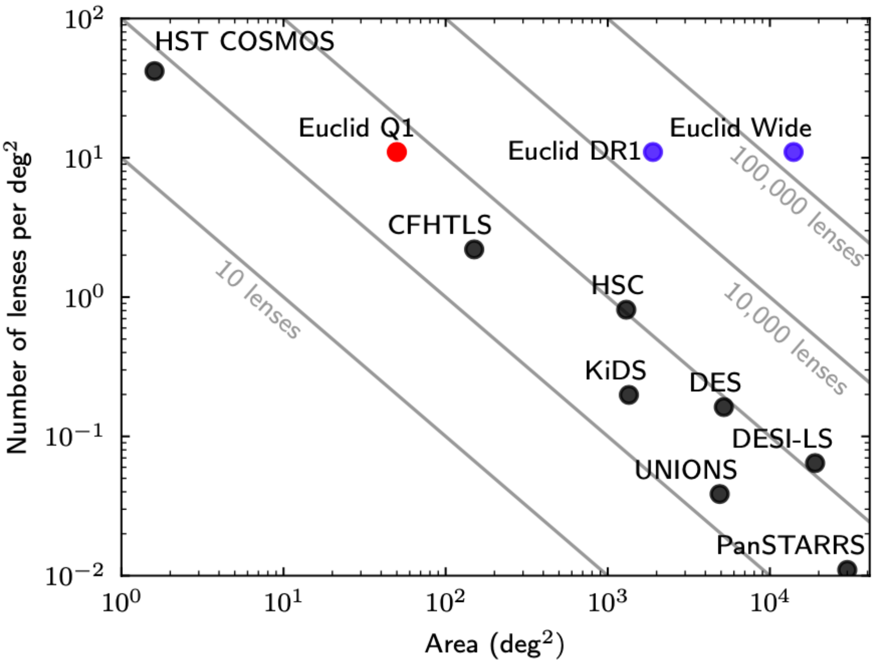

Figure 4.2: Comparison between the capabilities of finding lenses of Euclid and recent surveys. This plot represents the number of lenses per deg^2 as a function of the survey area, and we can see also contours corresponding to a constant number of detected lenses. The lenses considered are A and B graded, so they exhibit the highest reliability. It is important to remember that for Euclid DR1 and Euclid Wide the performance has been estimated. [Euclid Collaboration (2025)]

An example of the critical role of this mission is represented by the expected increase, of about one order of magnitude, in the number of gravitational lenses produced by galaxy clusters currently identified. Indeed, projections estimate that more than 4200 strong lensing clusters will be observed by Euclid. The rate at which the telescope collects data is 6.25 $\deg^2$ per day; in this regard, citizen science will be important to help visual inspection of the great amount of data that are produced. Indeed, visual searches for galaxy-galaxy strong lenses are usually performed using several approaches: expert inspection, citizen science, and automated searches. Expert inspection consists of the analysis of candidate images by professional astronomers; unfortunately, this technique requires a great amount of time and effort by the astronomers. Instead, citizen science is a faster approach since it relies on a larger "crowd" made by volunteers from the public. Moreover, automated searches are implemented with deep learning models, which are trained with lens and non-lens examples. The majority of the strong lenses, currently identified, have been detected through the synergy between deep learning methods and expert inspection. Taking these premises into account, many lensing applications, used in pairs with other techniques, will lead to meaningful results in the near future.

4.1.1 Instrumentation details

Euclid is equipped with an off-axis 3-mirror Korsch cold telescope, with a field of view of 0.54 $\deg^2$ and three mirrors built in Silicon Carbide (SiC), which is immune to ionising radiations. The primary mirror is characterised by a diameter of 1.2 m and remains at a temperature of $T < 130\ K$. Instead, the secondary mirror can be displaced by 1 μm, thanks to a 5 degrees-of-freedom mechanism (M2M), to correct focus and tilt. Furthermore, the telescope is connected to two instruments:

- **VIS**, shown in figure 4.3, which is a broad-band optical imager (spatial resolution of 0".18). This high-quality panoramic imager can study the distortion of galaxy shapes with $I_E \lesssim 24.5$ and it covers the 550 to 900 nm region using a broad-band filter. This instrument will be crucial for obtaining weak-lensing measurements.

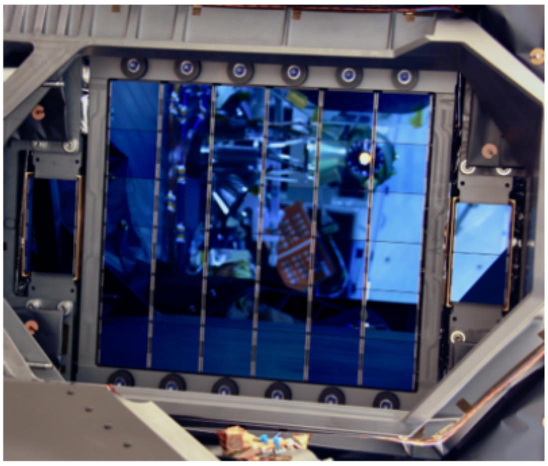

Figure 4.3: VIS focal plane, which is characterized by an array (6 x 6 e2V) of CCDs. Courtesy of Thales Alenia Space (TAS) [Troja et al. (2022)]

- **NISP** (Near-Infrared Spectrometer and Photometer), shown in figure 4.4, which integrates the capability of an imager in the NIR bands (Y_E, J_E, H_E) with a NIR-slitless spectrograph. Therefore, this instrument is crucial for obtaining the photometric redshifts of galaxies that are studied with VIS and for obtaining the redshifts of galaxies characterized by bright emission lines. This instrument is defined by a wavelength coverage of $900 - 2020$ nm.

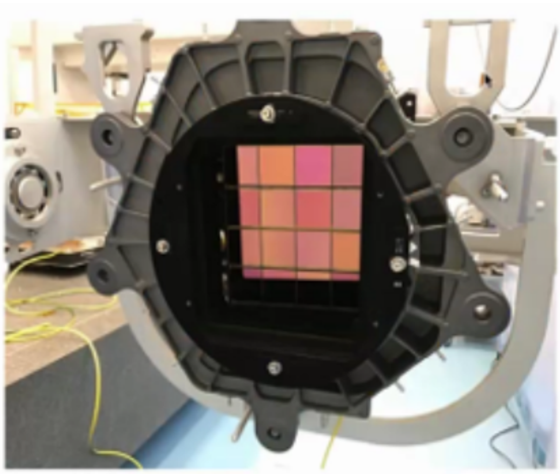

Figure 4.4: NISP focal plane, which is equipped with an array (4 x 4) of HAWAII-H2RG detectors. Courtesy of Thales Alenia Space (TAS) [Troja et al. (2022)]

The Euclid mission also includes a fine-guidance sensor (FGS), made of four charge coupled devices (CCDs), which is adiacent to the VIS detectors.

4.2 Euclid Quick Data Release 1

Euclid includes three major data releases: the Data Release 1 (DR1) regarding the data collected during the first year (sky area of 2500 deg^2), the Data Release 2 (DR2) which considers the first three years (sky area of 7500 deg^2), and finally the Data Release 3 (DR3) available after all observations have ended. Currently, only the Euclid Quick Data Release 1 (Q1) has been released with the aim of showing, to the astronomical community, the potential of the Euclid mission. This release, containing data of about 7 days of observations, is important for non-cosmological studies, as demonstrated by the several articles that have been published using this dataset. Q1 already includes about 30 million sources, such as galaxies, stars and quasars. More specifically, this special release contains a number of detectable strong lenses comparable to the most extensive searches so far. The results and lens catalog obtained from the Q1 release are going to be important in: training machine-learning algorithms in view of Data Release 1 (DR1), showing the potential of the Euclid survey data, and defining new scientific projects.

The Q1 covers an area of 63.1 deg^2 of the Euclid Deep Fields (EDFs) and includes visible and near-infrared space-based imaging and spectroscopic data, as well as ground-based photometry in several bands (u, g, r, i and z). For Q1, all EDF observations are made with the "red grism" (RG_E, $1206 - 1892$ μm) and the "blue grism" (BG_E, $926 - 1366$ μm); considering a blue-to-red exposure-time ratio of $5:3$. These EDFs offer a preview of the depth expected throughout most of the survey and through multiple observations, with DR3, they will go deeper in magnitude, about 2 mag, than EWS. Each EDF visit, composed of "patch" of reference observing sequences (ROSs), covers the full deep field considering an area of 53 deg^2. A margin of 10 deg^2 is necessary for the tiling and the variation of the position angle from the orbit progression.

This first dataset is limited to three specific areas, represented in figure 4.5), near the ecliptic poles:

- the **EDF-North** (EDF-N) which is an ecliptic-polar field with a circular shape. This field is always visible and will cover 20 deg^2 by DR3.
- the **EDF-South** (EDF-S) which, at a lower ecliptic latitude, is characterised by a stadium shape and will cover 23 deg^2 by DR3.
- the **EDF-Fornax** (EDF-F) which defines a circular region centred on the Chandra Deep Field South (CDES). This region, for Euclid, has two short visibility windows per year. By DR3, this field will cover 10 deg^2.

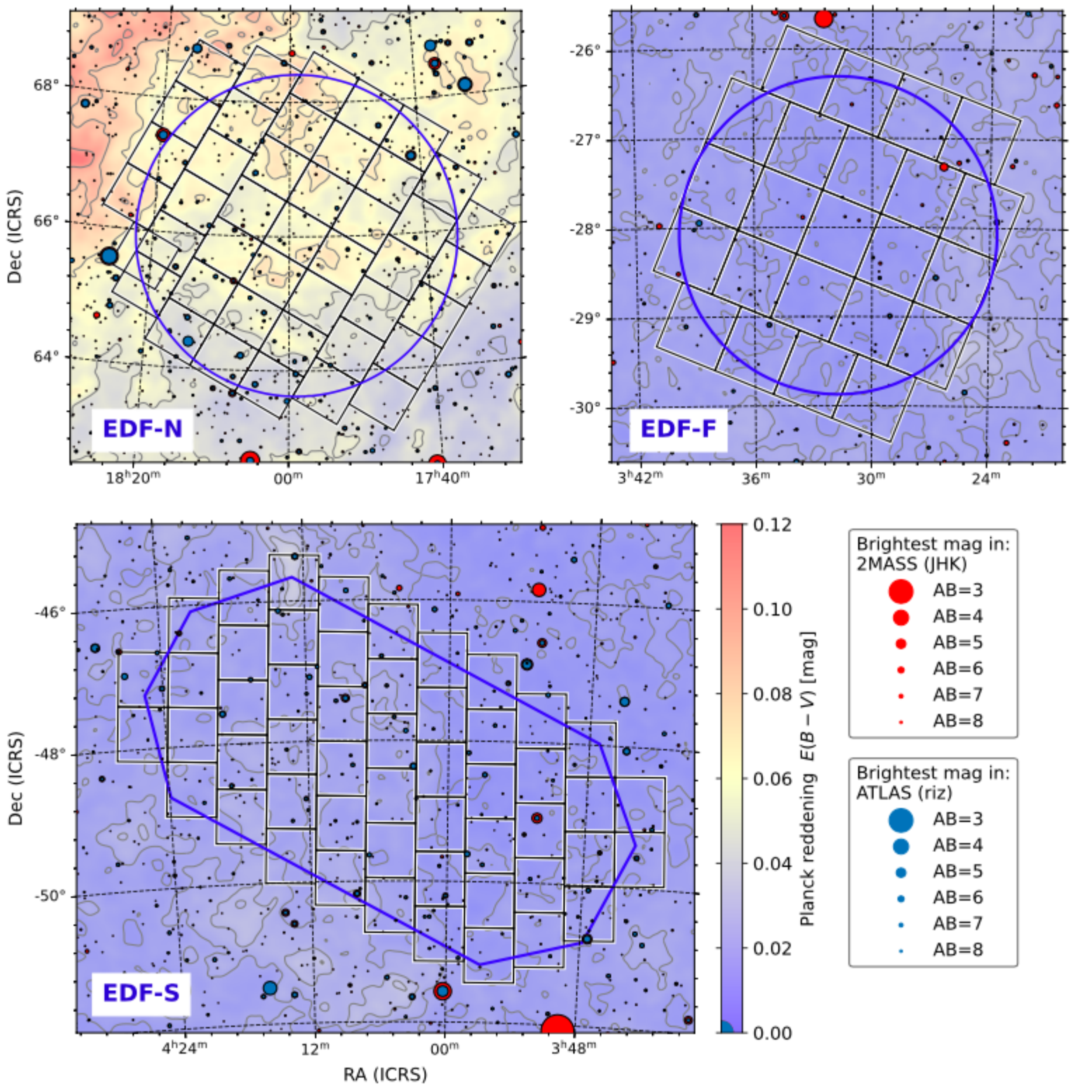

Figure 4.5: Three EDF tilings of Q1 overlaid with the bright stars from 2MASS and ATLAS-Refcat2. The blue lines, in these boxes, represent the areas that will be covered to full depth with the DR3. [Euclid Collaboration (2025)]

In order to demonstrate, through Q1, the potential of the EWS the researchers considered ground-based observations overlapping the EDFs locations.

4.2.1 Data processing

Euclid collects visual and near-infrared images that are transferred to Earth every day. The satellite data are complemented with data, referring to the same sky area, from ground-based telescopes. Indeed, the Euclid mission archive also includes ground-based photometry data from large-area surveys, such as the Ultraviolet Near-Infrared Optical Northern Survey (UNIONS) in the northern sky and the Dark Energy Survey (DES) in the southern sky. The data of the mission are then processed by the Science Ground Segment (SGS) which is organised across ten Science Data Centres (SDCs) located in Europe and the United States. The pipeline used for processing includes several processing functions (PFs) and leads to various data products, as we can see in figure 4.6. The development of these PFs is defined by the Organisation Units (OUs), which include Euclid scientists and engineers with specific competences.

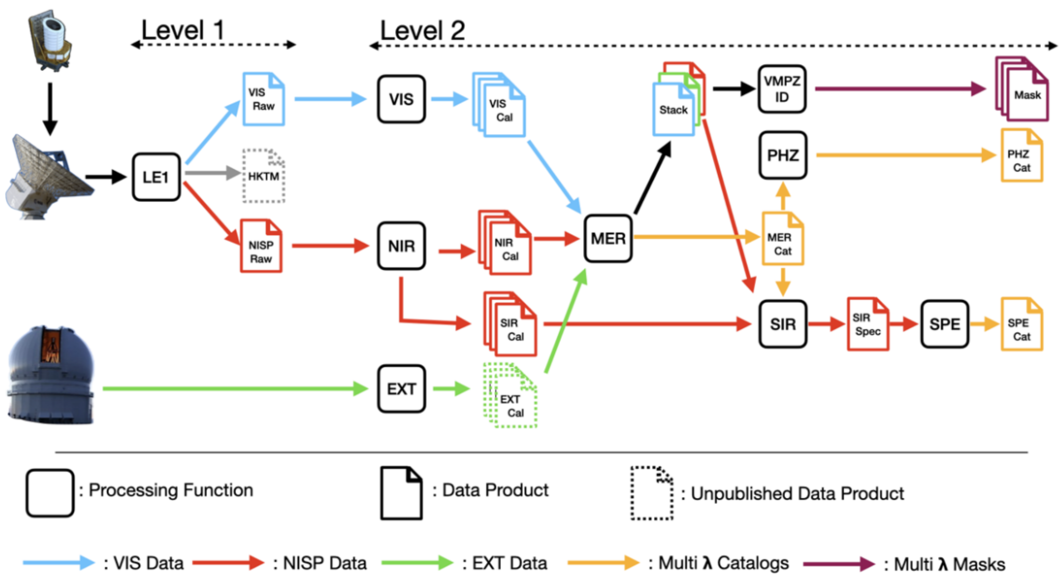

Figure 4.6: Brief overview of data processing for the Q1 release [Euclid Collaboration (2025)]

Considering spacecraft communication, the first step of data processing is represented by the extraction and reconstruction of individual data streams from a time-multiplexed signal. This phase is usually known as telemetry decommutation, where telemetry refers to VIS and NISP detector data, as well as spacecraft housekeeping data. So, the "LE1"-PF transforms telemetry into three level 1 products: the VIS and NISP raw-frame products and the housekeeping telemetry (HKTM) product. The VIS and NISP raw-frame products are the inputs of the SGS pipeline for data processing, while the HKTM product, not distributed in Q1, is important for reconstructing the VIS point-spread function (PSF).

These LE1 products are distributed among the other SDCs, in order to obtain the LE2 products; the VIS PF processes VIS data into single-frame calibrated images in the I_E band, while the NIR PF processes NISP imaging data into single calibrated frames in the Y_E, J_E and H_E bands. Instead, the external ground-based imaging data are processed by the EXT PF. At this point, these data are collected by the MERge datasets (MER) PF, which defines combined stacks per band and creates a master catalog. To summarise, MER processing divides the sky into tiles of $32' \times 32'$ with a $2'$ wide overlap. This PF is crucial since, for each source, it provides photometric and morphological measurements; with MER photometric information, which are then used by the PHotometric redshift (PHZ) PF to study the source. The PHZ pipeline is important for several reasons; in fact, it is responsible for the source classification based on photometric colours, the determination of photometric redshifts, and the physical properties of the source. For example, for galaxies, the PHZ processing function determines the luminosity, the star-formation rate, and the stellar mass. The list of parameters calculated by the PHZ PF is represented in figure 4.7.

Parameters	Comments
Galaxies (Method: NNPZ)	
Redshift	
AGN bolometric luminosity	
Intrinsic attenuation A_V	not in the catalogue
Absolute AB magnitude[a]	
Stellar metallicity	[Fe/H]
(SFH) Stellar age of galaxies	
(SFH) Characteristic SF timescale	
Star formation rate (SFR)	$\log_{10}(\mathrm{SFR}/\mathrm{M}_\odot\,\mathrm{yr}^{-1})$
Stellar mass	$\log_{10}(\mathrm{M}_*/\mathrm{M}_\odot)$
Stellar mass formed during SFH	$\log_{10}(\mathrm{M}_*^{\mathrm{form}}/\mathrm{M}_\odot)$
Stars, QSOs, NIR-only objects (Method: Phosphoros)	
Redshift	not for stars
SED normalization in $L_\odot$	
Luminosity in $L_\odot$	not for stars
SED template	
Reddening curve	not for stars
Internal color excess E_{B-V}	not for stars

Figure 4.7: List of the physical parameters determined by the PHZ PF. [Euclid Collaboration (2025)]

Moreover, the determination of the photometric redshifts has been tested using the COSMOS2020 catalog and a sample of spectroscopic redshifts. In figure 4.8 we can appreciate the redshift distribution of all VIS-detected objects, not star-classified, with $I_E < 24.5$ and $S/N\ (I_E) > 5$.

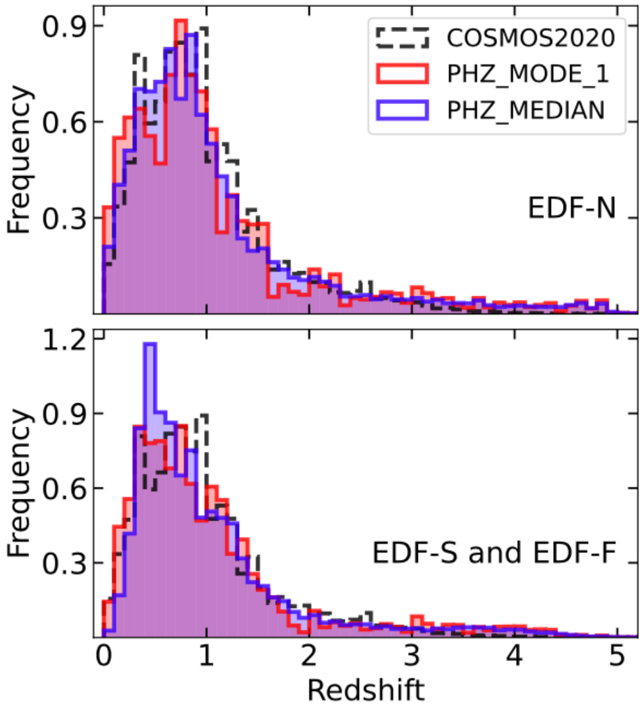

Figure 4.8: Redshift distribution for objects identified in the EDF-N (top) and in the EDF-S and EDF-F (bottom). The redshifts were estimated using the median of the redshift posterior probability distributions (zPDFs) in blue and the centroid of the zPDFs main peak in red. In the figure there are also the redshifts obtained from the COSMOS2020 catalog ($I_E < 24.5$) as dashed histograms. The redshifts appear consistent with the COSMOS2020 catalog and they present a peak around $0.5 - 0.8$ and a decrease at $z > 1$. [Euclid Collaboration (2025)]

At this stage, the spectra, for the sources detected at $H_E \leq 22.5$, are extracted from the NISP spectroscopic exposures and processed by the SIR-PF which produces calibrated spectra. The output of the SIR-PF is subsequently processed by the SPEctroscopy (SPE) PF which provides measurements of redshifts and line fluxes.

As already introduced before, Euclid uses also external data, such as ground-based optical imaging to complement VIS and NISP data for the estimation of the photometric redshift. Since the external data set is not homogeneous, a common data model, named single-epoch frame (SEF), is required for the calibration and processing. The SEFs are then calibrated with a homogeneous photometric calibration that uses the Gaia spectrophotometric dataset.

4.2.2 Current applications

The Q1 dataset has already led to about 30 papers regarding non-cosmological science; these publications establish the foundation for efficiently exploiting Euclid data in upcoming releases. They range between several topics, among which we find:

- **nearby galaxies**, with the possible characterisation of dwarf galaxies;
- **galaxy morphology**, with data used as a starting point for deep-learning models. The goal is to define catalogs of galaxies with their properties and morphology-related features such as bars and spiral arms. Considering the image resolution and large area of the Q1 release, we could morphologically describe more than a million galaxies;
- **star-forming galaxies**, since the dataset has a high potential for studying scaling relations that are crucial to comprehend galaxy formation and evolution. In that regard, Euclid is really useful for working with statistical samples of peculiar objects;
- **galaxy quenching**, with the distinction between "Ageing", "Quenched", and "Retired" galaxies. Studying the drivers of galaxy quenching will lead to a better understanding of their evolution;
- **AGN evolution**, with photometric selections and spectroscopic diagnostics applied to Euclid data. This application is important for testing new machine-learning methods, for studying major mergers in triggering AGNs, and for exploring dust-obscured red quasi-stellar objects (QSOs);
- **cosmic environment** and how it impacts properties of galaxies and galaxy clusters. This analysis, for Q1 data, is performed by measuring the local environmental density for each galaxy;
- **strong gravitational lensing** since Euclid represents the most efficient instrument for the detection of lenses that has ever been built. More specifically, from Q1 data it was possible to define a catalog of 497 galaxy-galaxy strong lenses, and the final EWS will include more than 100 000 high-confidence lenses. This will mark an important turning point in strong lensing science;
- **galaxy clusters** with hundreds of high-confidence clusters already found in Q1. This release is also important for the detection of new strong lensing galaxy clusters and protoclusters at early epochs;

- **transients** with serendipitous observations.

4.2.3 Limitations

The Q1 release represents the first step of the Euclid mission and, therefore, it is limited by several factors. Data processing still needs improvement, with processing functions that have identified new pathways that need to be developed in view of DR1. Among the caveats that we need to consider, while working with these data, we find the redshift measurements and imaging data in specific cases. The Q1 dataset will be improved with the DR1, which will cover almost 30 times the Q1 area and, therefore, it will consist in an increase of about 1.5 orders of magnitude in the number of objects identified. We conclude this paragraph by recalling that the final data release, DR3, is expected in the early 2030s.

4.3 Dataset details

4.3.1 List of lenses

The list of lenses that I used is that described by the paper [Euclid Collaboration (2025)] and is available at [Walmsley et al. (2025)]. This catalog is made up of 497 strong lens candidates that have been identified from the Euclid Quick Release 1. Among these lenses, there are double source plane configurations and about 20 candidate edge-on lens galaxies. In order to identify the lenses correctly, researchers have considered an approach that combines multiple methods: deep learning methods, citizen science, and a final confirmation by astronomers. The idea is that by combining these search approaches, each will bring its own strengths and can partly compensate for the limitations of the other methods. Therefore, only the combination of these approaches will lead to the best results. For example, deep learning models can search in a great number of images but the samples that are produced usually contain a high number of non-lenses. Instead, citizen science, even if limited to a restricted number of images, is able to infer patterns outside of its training dataset. Lastly, experts are assumed to have high accuracy and low variance, but can analyze only a small number of images. More specifically, the experts were astronomers from the Euclid Consortium Strong Lensing Science Working Group, who voluntarily decided to collaborate and were asked to grade each image according to a specific system, as reported in table 4.1.

A+	Confident lens with intrinsic scientific value
A	Confident lens since it shows evident lensing features
B	Probable lens, with additional information needed
C	Possible lens, since it can be explained without lensing
X	Not a lens
otherwise interesting	Not a lens but could still be interesting

Table 4.1: Classification of lens candidates

These grades were adjusted to account for the potential mistakes made by experts and converted into a numerical score, reported in table 4.2. This step is necessary to aggregate the results of the expert inspection and define the final grades: candidates with a score above 2 are defined Grade A, while with a score above 1.5 we talk about Grade B candidates.

Score	Grade
0	X
1	C
2	B
3	A or A+

Table 4.2: Score to grade conversion

We can appreciate the results of this scoring system in figure 4.9, and it is important to remember that the lenses were modelled according to an automated strong lens modelling. From the lens catalog available at [Walmsley et al. (2025)], I have considered only candidates graded A and B. Therefore, my starting point is represented by a sample of 497 lenses, in which 250 are candidates of grade A and 247 are of grade B. By applying the current classifiers to the DR1 release, we could possibly get from 3900 to 7600 lens candidates of grade A and B; this number is higher than the one obtained by adding together the results of previous studies. Extending the discussion to the complete Euclid Wide Survey, we could obtain about 100 000 high-confidence candidates; this result would inevitably change strong lensing science.

4.3.2 The ESA Datalabs platform

The analysis of Euclid Q1 data was possible thanks to the ESA Datalabs platform [ESA Datalabs] which is an e-science platform that allows direct access to the ESA's archives. This environment, for space data processing, plays a crucial role since it integrates access to big data, notebook technologies, and domain specific software.

Figure 4.9: A subset (140 of 500) of candidates for strong lenses is presented here as a function of the score assigned by the astronomers. In the upper left corner there are the lenses with the highest grades while in the lower right corner there are the lenses with the lowest grades. [Euclid Collaboration (2025)]

Chapter 5

Companion galaxies around strong galaxy-galaxy lenses and non-lens galaxies

5.1 Research aim

The aim of the thesis is performing a comparative study of companion galaxies around strong galaxy-galaxy lenses and non-lens galaxies. The control sample has been defined according to the distribution, in redshift and absolute magnitude, of the lenses.

The environmental analysis starts with an examination of the lines-of-sight of the two samples, using a specific redshift cut. Moreover, the average number of companions, surrounding the two samples, are compared and the environments are studied considering the radial profiles of the cumulative counts and the cumulative surface densities. In particular, the analysis includes the computation of the survey average density, which represents a reference for the latter profile. Then, the distribution of companion galaxies are statistically compared using the two sample KS test. It is interesting to also characterise the environments by comparing the distances, from the central source, of their n^{th} closest companion and to represent these values through a radial map. Additionally, companion galaxies are studied as a function of absolute magnitude and redshift; this approach is adopted to investigate whether the observed excess of companions depends on the physical properties of the galaxies.

The results obtained need to be interpreted considering the importance of environmental effects in lens models, as reported in [Keeton & Zabludoff(2004)]. The characterisation of lens environments prevents biases and uncertainties in several lensing applications, including constraints on the masses of galaxy dark matter halos. Errors related to the environments are not random errors but systematic biases resulting in overestimates of the lens galaxy velocity dispersions, the Hubble constant and the dark energy density parameter Ω_Λ. The environment influences, through local and LOS overdensities, the external convergence which then modifies the estimates of lensing and cosmological quantities.

Finally, the environmental information is translated, within the HOD framework, into a mass ratio between the dark matter halos of lenses and non lenses. Therefore, this study aims to investigate and quantify possible differences in the local environments of lens and non-lens galaxies, and to evaluate their implications for their corresponding dark matter halo masses.

5.2 Lens sample

The lens sample is made of 497 lenses which are A or B graded; this list includes the more reliable lenses identified using Q1 data. The lenses are univocally identified through specific object ids which are useful to match information from several catalogs. To study the lenses we need to consider the parameters reported in the Euclid *MER* and *PHZ catalogs*; according to our goal the most interesting parameters are represented in table 5.1.

Parameter	Description
right_ascension	for the host galaxy (in degrees)
declination	for the host galaxy (in degrees)
vis_det	source detected in the VIS (1) or NIR mosaic (0)
flux_detection_total	total flux of the source (μJy)
mu_max	peak surface brightness above background (mag/arcsec^2)
mumax_minus_mag	to distinguish point and compact sources (mag/arcsec^2)
phz_median	median of the PHZ PDF

Table 5.1: All the parameters were obtained from the *mer_catalogue*, except for the *phz_median* that is retrieved from the *phz_photo_z*

In joining information from the two catalogs, we notice that the object ids of two sources are not included in the *PHZ catalog* and, therefore, these sources are excluded from the analysis. Moreover, two lenses present invalid redshift values; therefore, the final sample includes 493 lenses. This situation cannot be modified, considering that redshift is going to be a key parameter in the identification of companion galaxies.

5.3 Control sample

The analysis of the lens sample is performed considering an appropriate control sample made of non-lens galaxies. More specifically, this control sample needs to be as similar as possible to the lenses, in order to obtain conclusions that are not limited by other factors. To minimise selection biases the sample of non-lens galaxies is defined with a similar distribution in redshift and absolute magnitude as the lenses; this choice reduces possible differences related to luminosity and cosmic epoch. This control sample is produced considering all the galaxies identified in the Q1 data release, which are objects satisfying the following quality cuts:

- **vis_det = 1** → to consider only sources detected in the visible.
- **flux_detection_total > 0.912** → to exclude faint objects. In particular, only galaxies brighter than 24 *mag*, in the Euclid VIS band, are considered. In fact, according to the 'AB system' [Tonry et al. (2012)] we can use the following relation to relate the apparent magnitude to the total flux

$$m_{AB}(\nu) = -2.5\log_{10}\left(\frac{f_\nu}{3631\ \mathrm{Jy}}\right) \tag{5.1}$$

  It is important to remember that $flux\_detection\_total$ is expressed in μJy, therefore it needs to be converted in Jy ($1\mu Jy = 10^{-6} Jy$).

- **mu_max > 15.0** → is a cut on the maximum surface brightness, which is applied to exclude less reliable detections.
- **mumax_minus_mag > -2.6** → is a cut on the difference between the maximum surface brightness and the total magnitude, which is applied to remove spurious detections.
- **phz_median > 0** → to include only objects with a valid redshift value.

The application of these cuts leads to the definition of a control pool made of 4 368 438 galaxies. This initial sample is then reduced by excluding possible duplicates and by removing galaxies that are included in our lens catalog. To obtain the final control sample we need to consider the redshift and the absolute magnitude of the lens sample. More specifically, we need to compute the absolute magnitude of galaxies and lenses

$$M = m - 5\log_{10}\left(\frac{D_L}{10\ pc}\right) \tag{5.2}$$

where the luminosity distance D_L is obtained thanks to **Planck2018** cosmological model (astropy library) and the photometric redshift of the sources. Working with the absolute magnitude is crucial to consider the intrinsic luminosity of each source, independent of its distance from the observer. After removing objects with invalid absolute magnitude values, the analysis proceeds in the (M, z) plane with a two dimensional histogram matching. The starting point is represented by the lenses distribution, with the definition of a two dimensional histogram $H_{lens}(M, z)$ in absolute magnitude and redshift. Considering 20 bins in absolute magnitude and 20 bins in redshift, the lenses are represented in a 20 x 20 matrix in which each cell reports the number of lenses it contains. This approach is also considered, with the same bins, for the creation of another two dimensional histogram $H_{control}(M, z)$ which represents the distribution of the control pool. The control pool represents the initial sample from which galaxies are drawn randomly, always according to the lenses properties, to define the final control sample. These 2D-histograms are crucial for the production of the final control sample, since they define the probability of a galaxy, from the control pool, of being selected

$$P_{select}(M, z) = \frac{H_{lens}(M, z)}{H_{control}(M, z)} \tag{5.3}$$

This quantity is used for the importance resampling of the control pool: the selected control galaxies will reproduce the distribution of the lens properties. The probability is then normalised in order to be useful for the matching; therefore, the bin with the highest number of lenses will have a normalised probability of 1, while the others will have values in between 0 and 1. The final control sample is obtained applying a stochastic selection: for each galaxy from the control pool a uniform random real number n_{random}, in between 0 and 1, is generated and compared to its normalised probability of being selected p, according to its (M, z) bin. If $n_{random} < p$ the galaxy is included in the final control sample. This approach leads to a sample of 45 653 galaxies with a similar distribution in absolute magnitude and redshift to the lenses, as reported in figure 5.1, figure 5.2, figure 5.3 and figure 5.4.

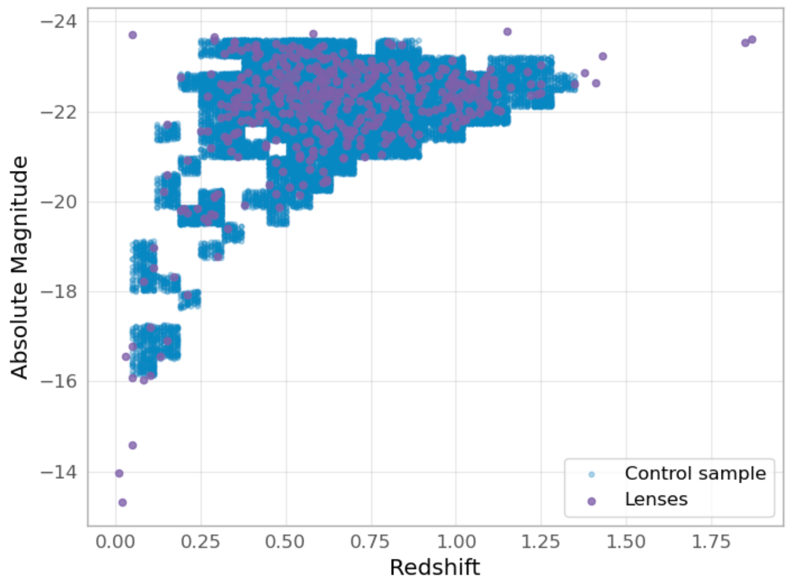

Figure 5.1: 2D histogram reporting the lenses and the control sample in the absolute magnitude-redshift plane. We notice that faint low-z (close to zero) lenses populate a region which does not present any control galaxy; this situation can be explained considering errors in the redshift determinations, as reported in [Euclid Collaboration(2026)]. Instead, for bright high-z lenses there could be the problem of the contamination from lensed source light.

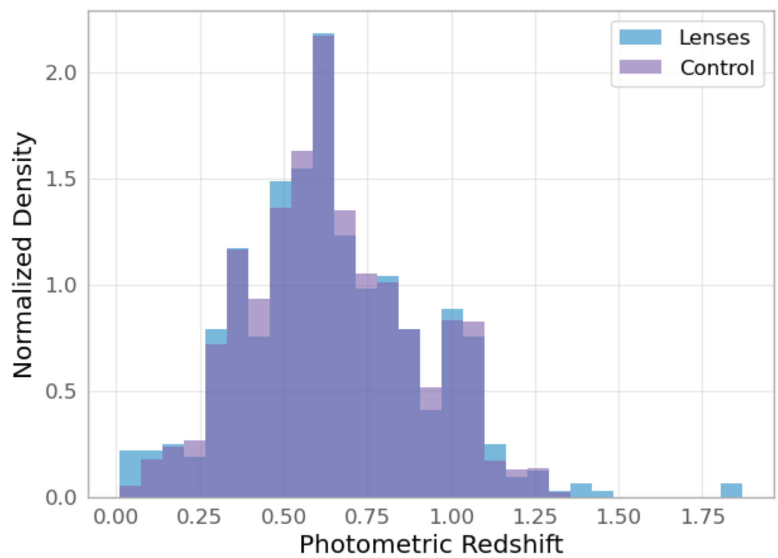

Figure 5.2: Redshift distribution for the samples of lenses and galaxies.

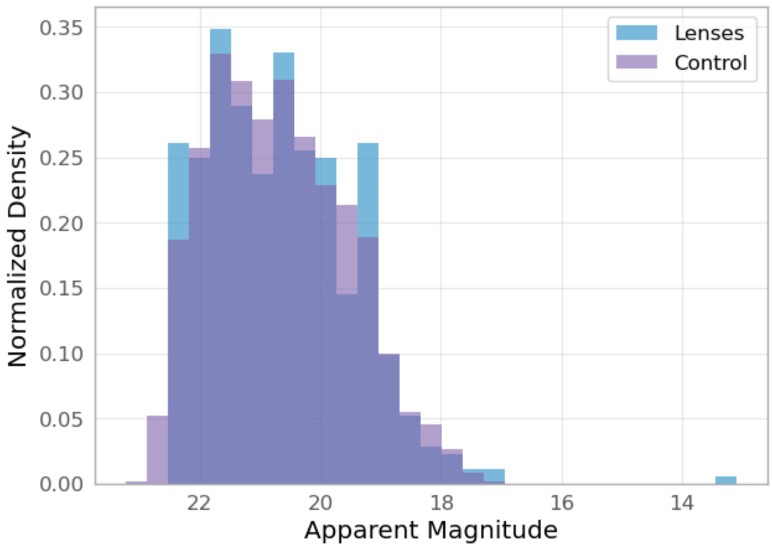

Figure 5.3: Apparent magnitude distribution for the samples of lenses and galaxies.

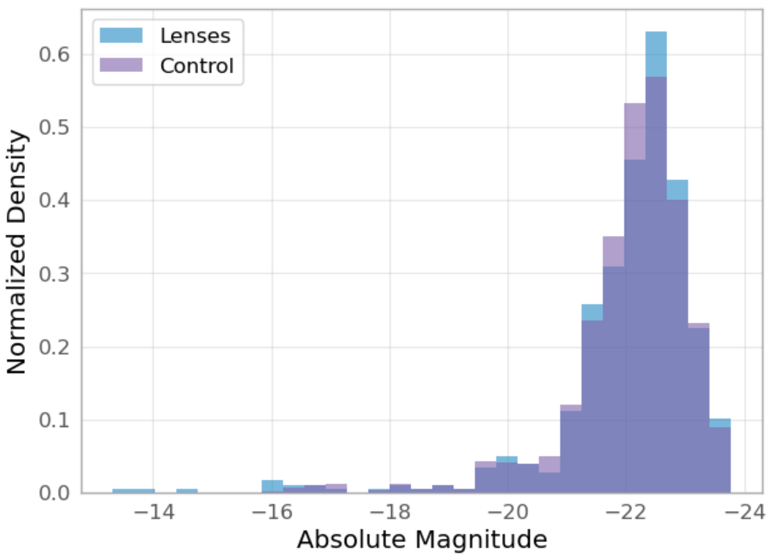

Figure 5.4: Absolute magnitude distribution for the samples of lenses and galaxies.

It is interesting to consider also the average values of redshift and absolute magnitude for the two samples, which are represented in table 5.2.

	Lenses	Control galaxies
Mean redshift	0.6475 ± 0.0124	0.6465 ± 0.0012
Mean absolute magnitude	-22.0441 ± 0.0590	-22.0894 ± 0.0050

Table 5.2: Average values of redshift and absolute magnitude for the lenses and the control sample. The errors are computed as the standard deviation of the sample divided by the square root of the sample size.

5.4 Possible line-of-sight bias

The analysis of the lens and control samples begins with an evaluation of possible line-of-sight (LOS) effects, which would introduce a bias in their comparison. In fact, the line of sight of lens systems could be disturbed by the large-scale structure (LSS) distribution, capable of adding perturbations to the lensing properties. If the line of sights of lenses are actually biased, the computation of parameters, such as the Hubble constant (H_0) using time-delays, will be biased.

5.4.1 Companions along the line-of-sight

In this regard, we want to work only with galaxies, identified along the LOS, with a redshift significantly different from the source of interest. For each source, lenses and non-lens galaxies, we consider the ring-counting approach developed by Altieri within the Euclid Collaboration: using a cone centred on the source, with an angular radius of 1 *arcmin* ($1' = 1°/60 = 0.0167°$). Inside this cone, we count the number of galaxies, according to the quality cuts introduced before. To distinguish the LOS contribution from the local lens environment we consider only galaxies with

$$\frac{\Delta z}{1 + z_c} = \frac{|z - z_c|}{1 + z_c} > 0.05 \tag{5.4}$$

where z_c represents the photometric redshift of the central source, while z is the photometric redshift of a possible companion galaxy. This redshift cut was originally applied to the Survey of Gravitationally lensed Objects in HSC Imaging project (SuGOHI) used in [Wong et al. (2018)]. The SuGOHI analysis was performed on the Hyper Suprime-Cam Subaru (HSC) imaging mainly in the i band. This environmental-selection strategy needs to be considered as a reference, which is applied to lenses and galaxies, extracted from the same survey, and processed homogeneously. The goal here is not a comparison with the SuGOHI results but a comparison between Q1 lenses and non-lens galaxies. The LOS analysis is applied to the lenses and a subsample of 1000 galaxies extracted from the control sample: for each source we count the number of foreground and background galaxies. During the evaluation of the LOS-objects, we exclude the central sources in order to prevent possible contaminations. The analysis leads to the conclusion that there is no significant difference in the LOS-objects of the two samples; in fact, the mean LOS galaxies for lenses is 53.134 ± 0.934 while for non-lens galaxies is 52.927 ± 0.479. The associated errors are boostrap errors, produced by generating 5000 resampling of lenses and galaxies. The ratio between these LOS-objects is 1.004 ± 0.020 with a 95% confidence interval equal to $[0.965, 1.043]$.

5.4.2 Statistical comparison

The analysis of the LOS galaxies is not limited to the means and the ratio, we also considers also their empirical distribution functions which are defined as follows:

$$\hat{F}_n(x) = \frac{1}{n}\sum_{i=1}^{n}\Theta(x_i \leq x) \tag{5.5}$$

In this formula where x represents the number of companion galaxies, $\Theta(x_i \leq x)$ is the Heaviside step function which is 1 when $x_i \leq x$ and is equal to 0 when $x_i > x$. In the limit of $n \to \infty$ we would expect $\hat{F}_n(x)$ to converge to the true cumulative distribution (CDF). With this approach we study the probability that objects, lenses and galaxies, are surrounded by less than a given amount of LOS galaxies. These empirical CDFs represent the starting point of the two-sample Kolmogorov-Smirnov test (KS test). This test compares two empirical CDFs, starting from the null hypothesis that both data sets come from the same data distribution

$$H_0 : \hat{F}_n(x) = \hat{G}_m(x) \tag{5.6}$$

Now, we introduce the KS statistic which represents the maximum vertical distance between the two sample cumulative distributions:

$$D_{mn} = \max\left|\hat{F}_n(x) - \hat{G}_m(x)\right| \tag{5.7}$$

This value should be interpreted as follows: if D_{mn} is small (close to zero) it means the distributions are similar.

Considering the LOS galaxies, surrounding lenses and galaxies, the KS statistic is equal to 0.0634. We compute the associated p-value, which represents the probability, under the initial null hypothesis, of obtaining this value for the KS statistic. Usually, the threshold is fixed at 0.05 meaning that for $p < 0.05$, corresponding to a confidence level of 95%, we can reject the null hypothesis. The p-value associated to the KS statistic for the two sample is equal to 0.1335. These values support the idea that the distributions of LOS galaxies surrounding lenses and non-lens galaxies are statistically similar; therefore, it is not possible to reject the null hypothesis.

5.4.3 The importance of line-of-sight contribution and comparison with previous work

It is interesting to focus on galaxy number counts around strong gravitational lenses (20), considering the results obtained with the Advanced Camera for Surveys (ACS) fields and reported in [Fassnacht et al.(2011)]. The comparison of galaxy counts, in fields containing moderate-redshift ($0.2 < z < 1.0$) lenses and two control samples, leads to the conclusion that the overdensity of galaxies along lenses LOS can be explained by the natural clustering of galaxies, rather than a line of sight bias for the lenses. In fact, lensing galaxies are usually massive early-type galaxies and so they are expected to lie in locally overdense environments. The Bayesian analysis of the number count distributions highlights, over a wide range of apertures, that lenses are surrounded, on average, by only a small excess of galaxies compared to non-lens fields. These average values can hide a large variation between different lens systems, which will become crucial in the determination of the Hubble costant. In fact, possible over- and underdensities along lenses LOS are quantified by the external convergence (k_{ext}), which is a key quantity for the estimation of H_0:

$$H_0 = (1 - k_{ext})H_{0,uniform} \tag{5.8}$$

where $H_{0,uniform}$ is equal to the estimate H_0 that does not consider k_{ext}. According to simulations these possible large variations would result in a determination of H_0 biased high by almost 2%.

This result is confirmed by studying the influence of matter along the line of sight of strong gravitational lenses, as performed in [Jaroszynski & Kostrzewa-Rutkowska(2014)]. Numerical experiments, by adding close neighbours to the line of sight of isolated lenses, include relative time delays which will modify the measurements of the Hubble constant. Moreover, objects along the LOS influence the external shear and so the lens potential itself, as reported in [Wong et al.(2011)]. In fact, by comparing the shear computed using the full environment and the one computed with only the local environment, it is possible to quantify the effect of LOS objects. They conclude that the shear contribution from these LOS objects is comparable to that produced by the local environment. Therefore, when working with strong gravitational lenses, we need to asses the presence of over- and underdensities along lenses LOS which could potentially bias our results.

Building upon the findings of [Fassnacht et al.(2011)], [Wong et al. (2018)] further investigate LOS overdensities of strong gravitational lens galaxies (87), considering the wide-area multiband imaging from the Hyper Suprime-Cam Subaru

Strategic Program (HSC SSP). By exploiting the specifics of the HSC SSP, capable of measuring the photometric redshifts to distinguish local galaxies from LOS galaxies, they obtained similar results to the previous study. In fact, the comparison of galaxy number counts, excluding the local environment, shows the consistency between the LOSs of the lens and control samples. Considering the lens and control samples obtained from the Q1 dataset, we are working with samples with similar distribution of their LOS galaxies.

5.5 Environmental comparison of lens and non-lens galaxies

After the analysis of the LOSs, the focus shifts to the characterisation of the local environments of lenses and non-lens galaxies. The local environments are quantified by the number of objects (within 1 arcmin from the central source) which satisfy the quality cuts for galaxies, and are defined by a redshift cut complementary to that adopted for the LOS. In the definition of the local environments the central sources are excluded. This approach produces two catalogs containing the companion galaxies of the two samples. To compare the environments of lenses and non-lens galaxies we consider: the average number of companions, the cumulative counts $N(< R)$ and the cumulative surface density $\Sigma(< R) = N(< R)/\pi R^2$. The total number of companions, within 1 arcmin, and their average number are reported in table 5.3.

	Lenses	Control galaxies
Total number	493	45 653
Total companions	6003	444977
Average companions	12.176 ± 0.330	9.747 ± 0.028

Table 5.3: Data describing the environmental comparison between lenses and non-lens galaxies. The errors are computed as the standard deviation of the sample divided by the square root of the sample size.

Lenses are, on average, surrounded by more companion galaxies than non-lens galaxies; more specifically, there are, on average , 2.429 ± 0.332 more companions within 1 arcmin. The uncertainty on the difference is obtained by standard error propagation, assuming independent uncertainties on the mean values. To quantify the relative variation V, between lens and non-lens galaxy companions, we consider the following expression

$$V = \frac{\bar{N}_{lens} - \bar{N}_{control}}{\bar{N}_{control}} \tag{5.9}$$

where $\bar{N}_{lens}$ and $\bar{N}_{control}$ are the mean number of companions surrounding lenses and control galaxies. The error, associated to this variation, is computed, assuming independent uncertainties of the mean values, through the standard error propagation

$$\sigma_V = \sqrt{\left(\frac{\partial N_{\text{lens}}}{\partial V}\right)^2 \sigma^2_{\text{lens}} + \left(\frac{\partial N_{\text{control}}}{\partial V}\right)^2 \sigma^2_{\text{control}}} = \sqrt{\left(\frac{\sigma_{\text{lens}}}{\bar{N}_{\text{control}}}\right)^2 + \left(\frac{\bar{N}_{\text{lens}}\,\sigma_{\text{control}}}{\bar{N}^2_{\text{control}}}\right)^2}$$

The global variation is equal to 0.249 ± 0.016, indicating that lens galaxies exhibit an excess of approximately 25% in the average number of companions with respect to control galaxies. Now, we consider the cumulative quantities which are studied, as a function of the radial distance from the central source, using 10 bins of $0.1'$ each. The cumulative radial profiles, figure 5.5, highlight a higher number of companions for lenses, with respect to control galaxies, at small radii. The separation between these profiles becomes more important as a function of the radius, with larger radii characterised by the largest discrepancy. In contrast, for the cumulative surface density profiles, figure 5.6, we notice the largest separation at small radii, while at larger radii the two profiles nearly converge. It is interesting to notice that only the companion galaxies of lenses in the first bin $(0' - 0.1')$ present a higher surface density with respect to the survey average. The survey average density can be computed considering all the galaxies ($N_{tot} = 4\ 395\ 097$) identified, according to the previous selection criteria, in Q1 data and the entire Q1 area ($A_{Q1} = 63.1\ deg^2$).

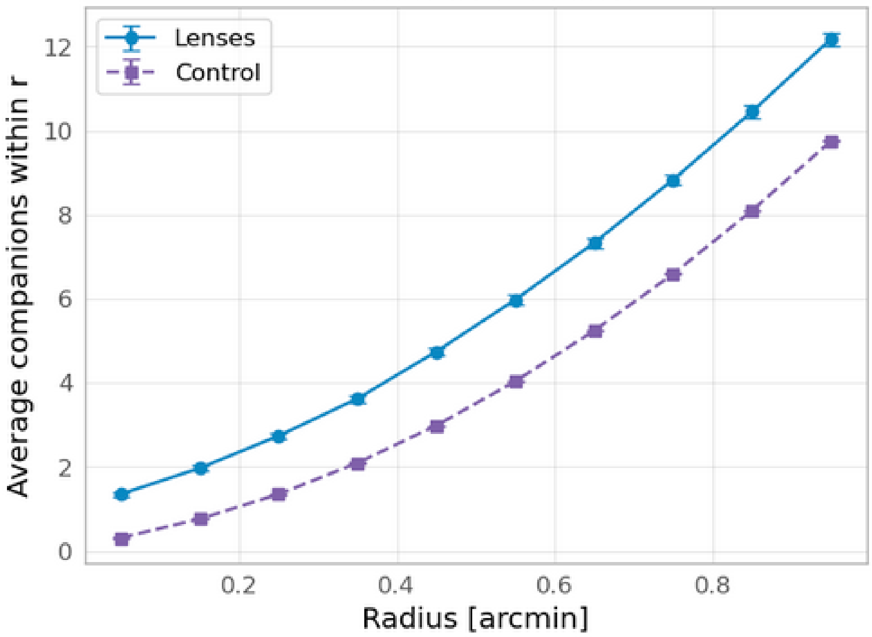

Figure 5.5: Cumulative radial profile, expressed in arcmin, of the average number of galaxies identified near the lenses and the control galaxies. The data points are plotted at the center of each radial bin. The error bars are computed assuming Poisson statistics $\sigma_{N(<R)} = \sqrt{N_{tot}(< R)/N_{sources}}$ where $N_{tot}(< R)$ refers to the companions and $N_{sources}$ to the central sources.

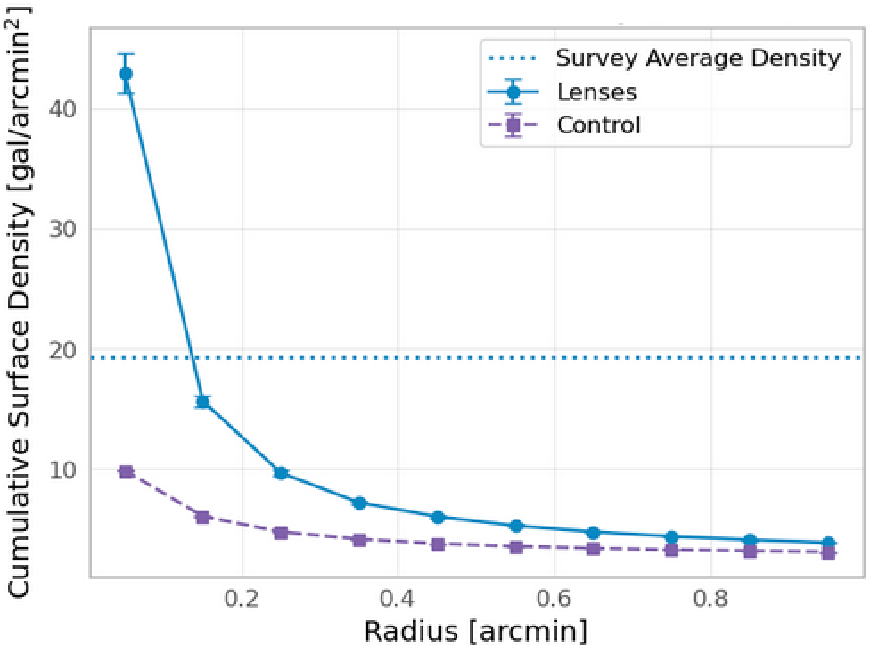

Figure 5.6: Cumulative radial profile, expressed in arcmin, of the surface density of galaxies surrounding the lenses and the non-lens galaxies. The data points are plotted at the center of each radial bin. The error bars are computed by propagating the Poisson uncertainty $\sigma_{\Sigma(<R)} = \sigma_{N(<R)}/\pi R^2$.

This area is usually expressed in deg^2 and so it needs to be converted into $arcmin^2$:

$$A_{Q1}[arcmin^2] = A_{Q1}[deg^2] \text{ x } 60^2 \tag{5.11}$$

Consequently, the Q1 average density can be computed as:

$$\sigma_{Q1} = N_{tot}/A_{Q1} = 19.348 \; galaxies/arcmin^2 \tag{5.12}$$

Instead, the error on the survey average density is obtained using the Poisson error on the total number of galaxies, divided by the survey area expressed in $arcmin^2$. Therefore, the Q1 average density is equal to $\sigma_{Q1} = (19.348 \pm 0.009) \; galaxies/arcmin^2$.

The surface density radial profiles can be improved using the physical distance, expressed in Mpc, which leads to a description of the real physical environments surrounding the sources. Objects at different redshifts can have the same angular separation, but not the same physical distance. The physical distances are computed through the following relation

$$R = \theta \cdot D_A(z) \tag{5.13}$$

where $D_A(z)$ is the angular diameter distance and θ is the angular separation expressed in radians. This latter quantity is transformed into a physical separation projected on the source plane.

The cumulative radial profile, in physical units, of the surface density of companions is presented in figure 5.7 , where the points correspond to the centers of 10 bins with a width of 0.06 Mpc. From this figure, we notice that the cumulative surface density profile of the lenses lies systematically above that of the control galaxies, with the largest separation observed within 0.06 Mpc. This suggests that lenses are characterised by denser environments, particularly in their immediate vicinity. As the projected radius increases, the cumulative surface density decreases for both samples, and the difference between the two profiles becomes much smaller.

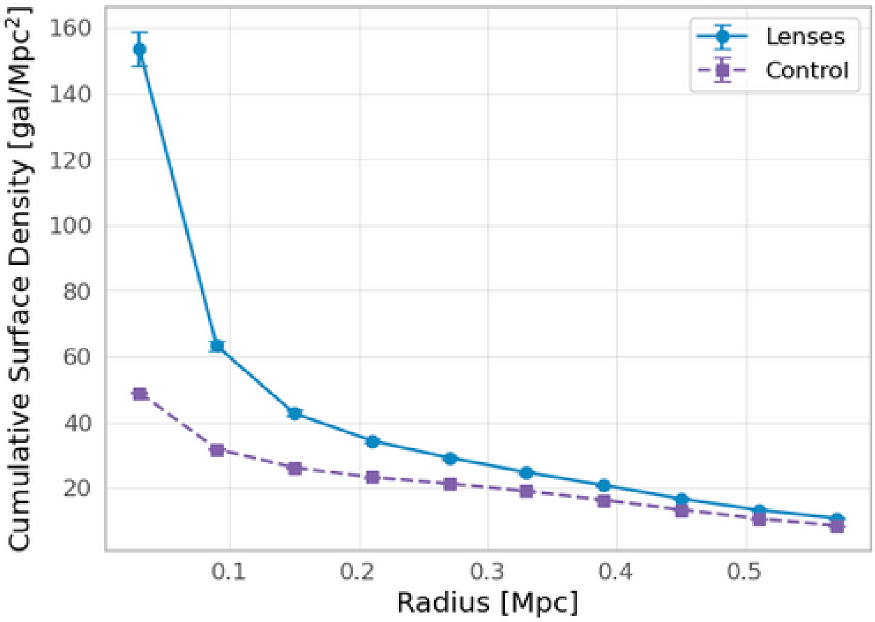

Figure 5.7: Cumulative radial profile, expressed in Mpc, of the surface density of galaxies surrounding the lenses and the non-lens galaxies. The error bars are computed by propagating the Poisson uncertainty $\sigma_{\Sigma(<R)} = \sigma_{N(<R)}/\pi R^2$.

Finally, the surface density is evaluated annulus by annulus, as reported in figure 5.8 where it is evident that the excess of companion galaxies is located within the innermost region around the lenses. This excess decreases as the projected radial distance increases, and it becomes negligible at about 0.4 Mpc.

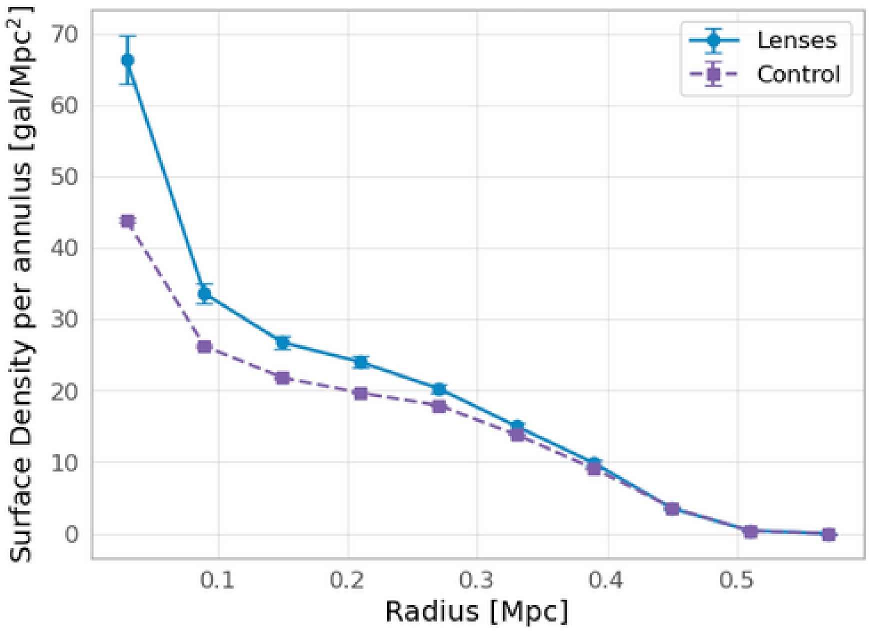

Figure 5.8: Radial profile per annulus, expressed in Mpc, of the surface density of galaxies surrounding the lenses and the non-lens galaxies. The data points are plotted at the center of each radial bin. The error bars are computed by propagating the Poisson uncertainty $\sigma_{\Sigma(R_1<r<R_2)} = \sigma_{N(R_1<r<R_2)}/\pi(R_2 - R_1)^2$.

Previous studies, such as the work of [Wong et al. (2018)], confirmed that lens fields contain a higher number counts of galaxies. Their analysis considers a control sample defined by randomly chosen galaxies and leads to the conclusion that lenses are characterised by a denser local environment than random fields, at the same redshift.

5.5.1 KS test of companion galaxy distributions

It is interesting to statistically compare the distributions of companion galaxies for the two samples; always referring to the previously constructed companion catalogs. The companion distributions, with the normalised density of objects as a function of the companions surrounding them, are reported in figure 5.9. In this plot the distribution of lens companions appears shifted, with respect to control galaxies, toward a region with a higher number of companions; in fact, lenses present a larger tail in the more populated environments.

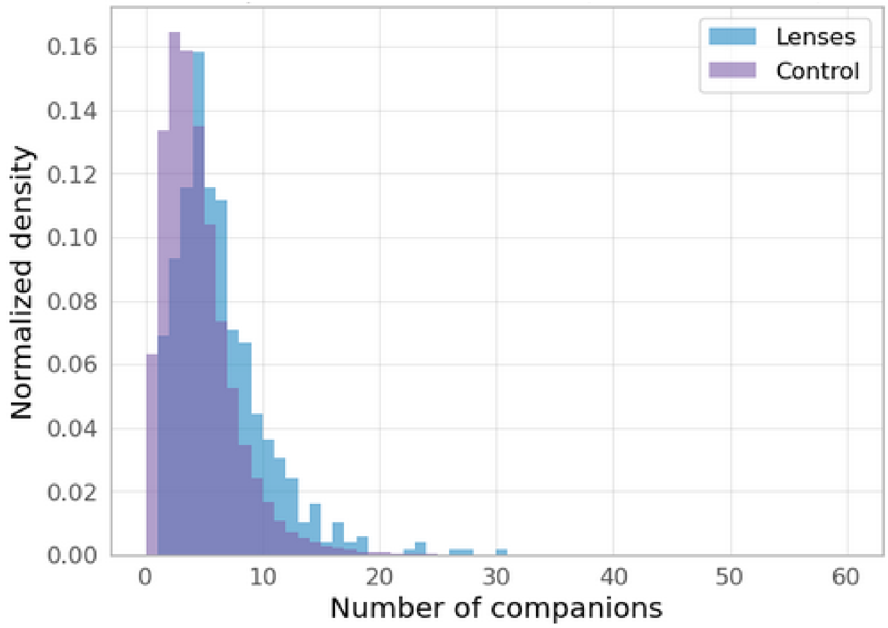

Figure 5.9: Companion distributions for lenses and control galaxies

The approach adopted to study the companion galaxy distributions is the two-sample KS test and to prevent any possible dilution effect, we focus on companion galaxies that are within 0.6 arcmin from the central source. This smaller search angular radius confirms that lenses are located in more populated environments; lenses are on average surrounded by 5.976 ± 0.185 companion galaxies within this radius, while non-lens galaxies only by 4.034 ± 0.015. With the errors computed as the standard deviation of the sample divided by the square root of the sample size. Returning to the KS test, the initial null hypothesis is that the CDFs for the companion galaxies, of the two samples, come from the same distribution. The CDFs of the two samples are reported in figure 5.10 where we notice that lenses are located in richer environments: the CDF of lenses is slightly shifted to the right, meaning that lenses need a higher number of companions to reach the same cumulative probability.

To asses the validity of the null hypothesis we consider the KS statistics and the p-value. The KS statistic is equal to 0.2422, indicating a maximum vertical separation of about 24% between the CDFs of the companion galaxies. Moreover, the associated p-value, equal to 1.0862×10^{-25}, leads to the rejection of the null hypothesis; therefore, these distributions are statistically different. The KS test is followed by the definition of the density ratio profile, which is obtained studying the

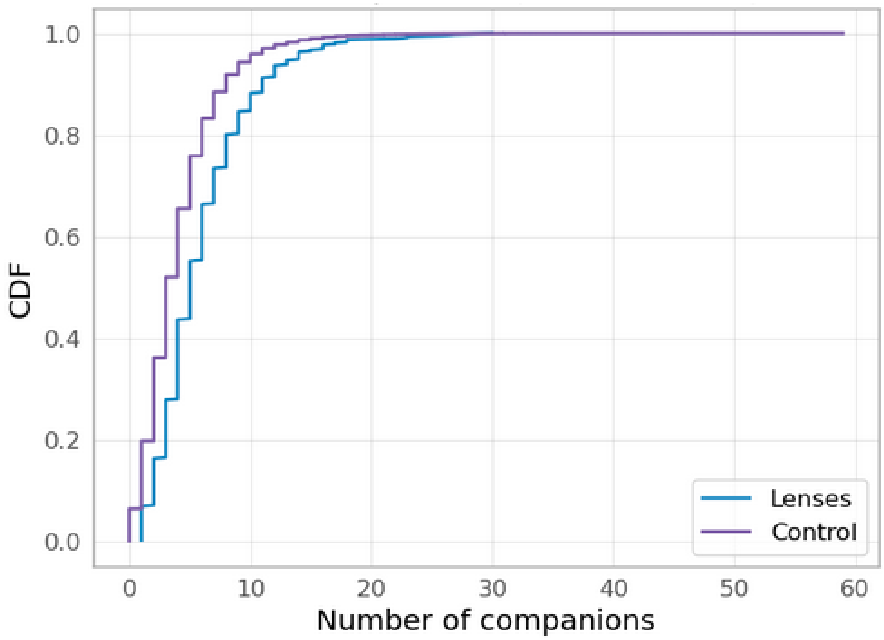

Figure 5.10: Empirical cumulative distribution functions of the lenses and control galaxies.

behaviour, as a function of the radius, of

$$\text{density ratio} = \frac{\Sigma_{lens}}{\Sigma_{control}}$$

where Σ_{lens} represents the density of companions for lenses, while $\Sigma_{control}$ describes the density of companions surrounding control galaxies. The result of this analysis, performed considering 10 bins of width equal to $0.06'$, is represented in figure 5.11 where we notice that this ratio is always above 1 meaning that lenses lie in denser environments with respect to non-lens galaxies. From the this figure we notice that lenses are characterised by a global overdensity which peaks as $r \to 0$.

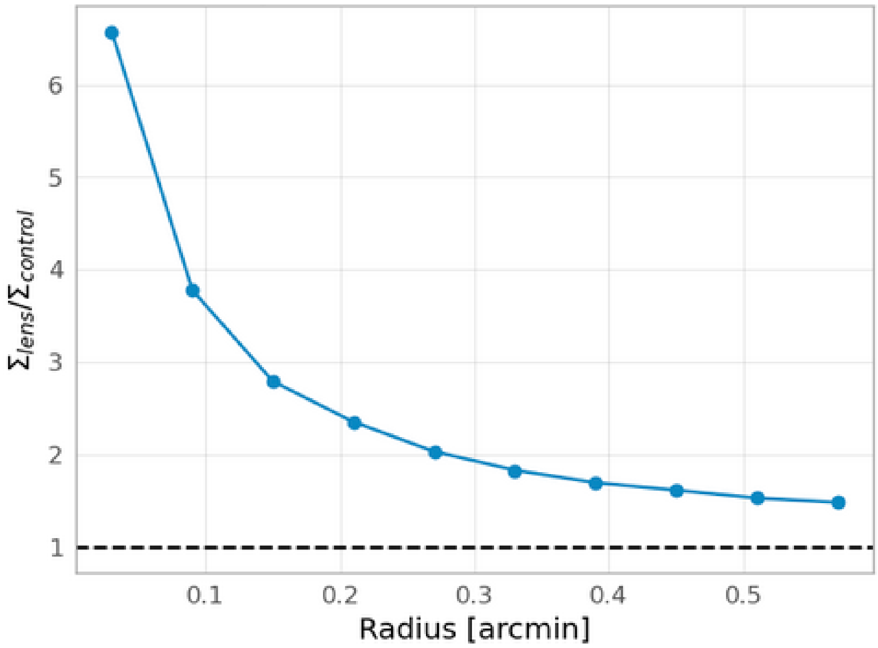

Figure 5.11: Density ratio profile representing the environment surrounding the lenses with respect to the non-lens galaxies. The data points are plotted at the center of each radial bin.

5.5.2 Environmental richness evaluation

Another approach to compare the environments of the two samples is to evaluate their richness according to the distance of their n^{th} companion; this method is commonly used in galaxy cluster studies. More specifically, we consider the distances of the 4^{th} and 10^{th} companions, as presented in table 5.4 and 5.5, in order to consider different environmental scales.

From these tables it is evident, since the number of objects is smaller than the sample size, that the selection criteria, in redshift and radial distance, are limiting the number of sources surrounded by the n^{th} companion. The results are obtained from the initial selection of only companions within 1 arcmin. The sources not surrounded, within a radius of 1 arcmin, by at least 4 companions are 46 lenses and 4480 control galaxies, and moving to the 10^{th} companion we exclude 199 lenses and 25969 control galaxies. This situation becomes progressively worse as we work with companions that are farther away, since the samples become progressively incomplete and dominated by galaxies located in denser environments. Therefore, the following results represent an estimate of lower limits for the distances and can be improved by increasing the radial distance, from the central source, within which we are searching for companions.

	Lenses	Control galaxies
Objects	447	41173
Mean distance (arcmin)	0.526 $\pm$ 0.010	0.589 $\pm$ 0.001

Table 5.4: Mean distances for the 4^{th} companion galaxies of lenses and non-lens galaxies. The errors are computed as the standard deviation of the sample divided by the square root of the sample size.

	Lenses	Control galaxies
Objects	294	19684
Mean distance (arcmin)	0.744 $\pm$ 0.011	0.789 $\pm$ 0.001

Table 5.5: Mean distances for the 10^{th} companion galaxies of lenses and non-lens galaxies. The errors are computed as the standard deviation of the sample divided by the square root of the sample size.

Moreover, the distributions of the 4^{th} and 10^{th} companions are studied through two-sample KS test; the results of this analysis are presented in table 5.6.

Distributions	KS statistics	p-value
4^{th} *companions*	0.1322	3.4286×10^{-7}
10^{th} *companions*	0.1348	1.5606×10^{-4}

Table 5.6: Results of the KS test applied to the distances of the n^{th} companion galaxies.

In both cases the distribution of distances are statistically different. To visualise the situation it is useful to consider a plot, figure 5.12 , which shows how the average distance of the n^{th} companion changes. The lens companions are consistently located closer to the central source, implying that they lie in a denser environment.

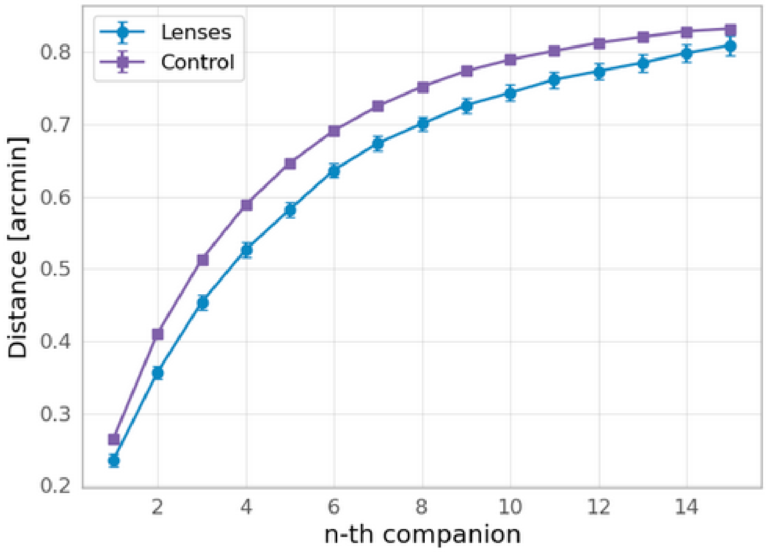

Figure 5.12: Plot representing the behaviour of the distance, in arcmin, of the n^{th} companion $(1 < n < 15)$ for both samples. The errors are computed as the standard deviation of the sample divided by the square root of the sample size.

This difference is quantified through a plot, figure 5.13, that analyses how this radial excess behaves as a function of n^{th}. From this figure we notice that there the radial excess reaches a maximum at the 5^{th} companion, and after slowly decreases.

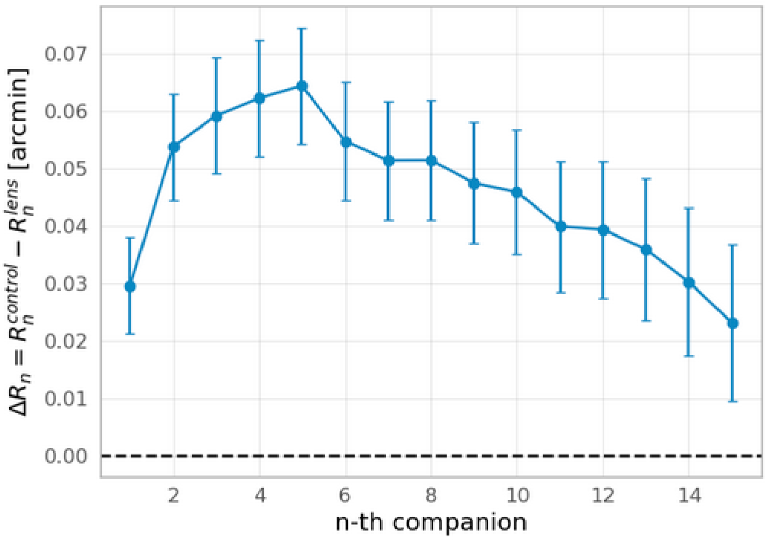

Figure 5.13: Radial excess between the distance of companions of lenses and control galaxies, as a function of the n^{th} companion $(1 < n < 15)$. The error bars are obtained through the standard error propagation, considering independent samples: $\sigma = \sqrt{\sigma_{lens}^2 + \sigma_{control}^2}$ where σ_{lens} and $\sigma_{control}$ are the standard errors associated to the means of the two samples.

The difference, in the distances of control galaxies with respect to lenses, can be represented also considering a radial map, figure 5.14, that represents the average distance at which the n^{th} companion is located. The map is defined in terms of concentric circles obtained through the parametric representation ($x = R_n \cos\theta; y = R_n \sin\theta$) where R_n is the distance of the n^{th} companion, presented in table 5.7 , and $\theta \in [0, 2\pi]$.

n	Lenses	Control galaxies	Radial excess
2	0.357 ± 0.009	0.410 ± 0.0010	0.054 ± 0.010
3	0.454 ± 0.010	0.513 ± 0.0010	0.059 ± 0.010
4	0.526 ± 0.010	0.589 ± 0.0010	0.062 ± 0.010
5	0.582 ± 0.010	0.646 ± 0.0010	0.064 ± 0.010

Table 5.7: Mean distances, in arcmin, at which the n^{th} companion ($2 < n < 5$) is located. The errors are computed as the standard deviation of the sample divided by the square root of the sample size. The number of sources surrounded by the n^{th} companion are limited by the selection criteria, in redshift and radial distance, which lead to an estimate of distance lower limits.

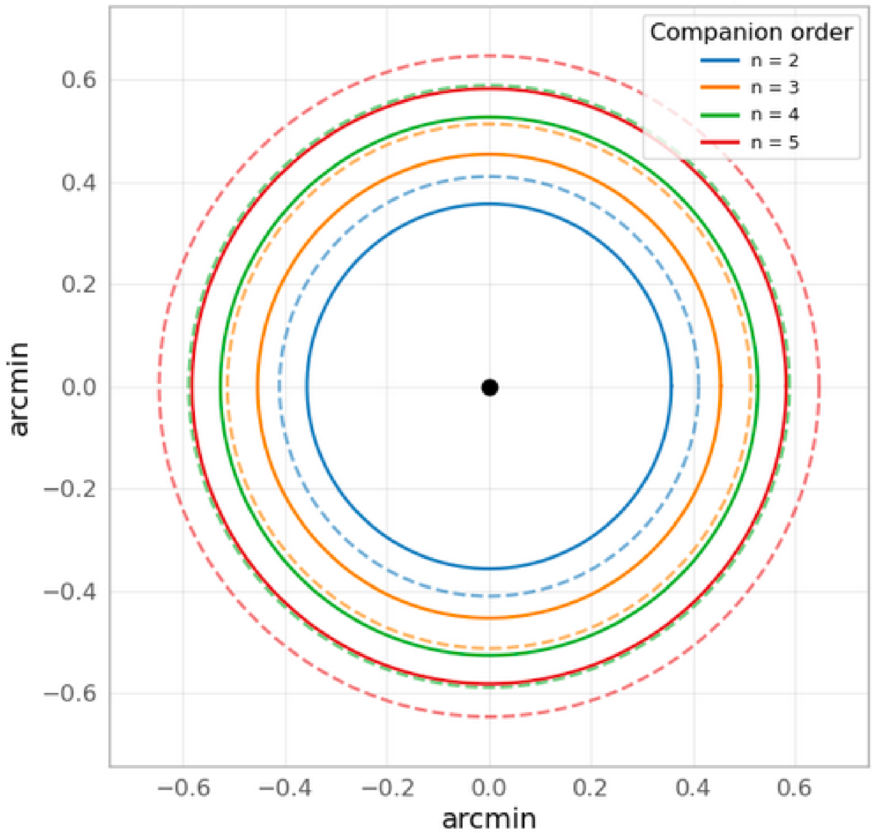

Figure 5.14: Radial map representing, for lenses (solid lines) and non-lens galaxies (dashed lines), the average distance at which the n^{th} companion ($2 < n < 5$) is located.

It is evident from figure 5.14 that lenses lie in denser environments, with the 5^{th} companion of lenses located nearly at the same distance of the 4^{th} companion of control galaxies. This situation, characterising also the 4^{th} companion of lenses and the 3^{rd} of galaxies, further confirms the differences between the two local environments.

5.5.3 Monte Carlo resampling of the control sample and evaluation of the errors

It is useful to apply the Monte Carlo resampling to the control sample and test whether the number counts of galaxies are Poisson distributed. Working with random subsamples, with the same size of the lens sample, we can analyse how the mean companion counts would change. The Monte Carlo resampling method tries to estimate a statistic's expectation value and variance, without assuming a specific distribution. By repeating this process 5000 times, we get a mean number of companions, for the control sample, equal to $\bar{N}_{control} = 9.751 \pm 0.269$, with the error corresponding to the standard deviation of the distribution obtained from the Monte Carlo resampling. This result can be compared with the lens sample to estimate the significance of their difference

$$\frac{\bar{N}_{lens} - \bar{N}_{control}}{\sigma_{control}} = 9 \tag{5.15}$$

which supports the hypothesis that lens environments are significantly denser with respect to non-lens galaxies. This situation is represented in figure 5.15.

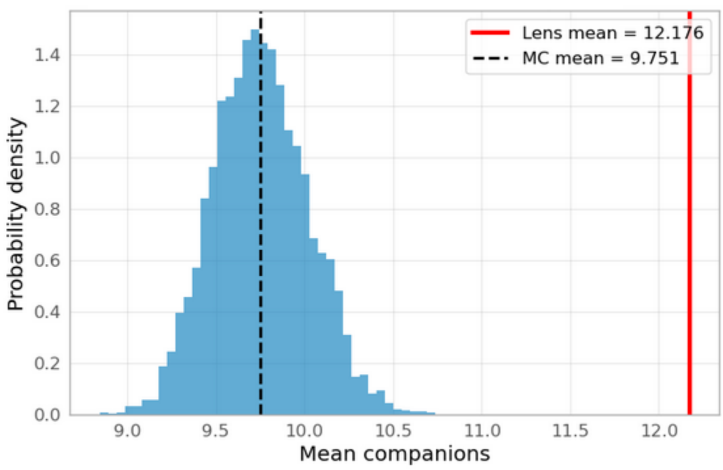

Figure 5.15: Representation of the Monte Carlo control subsamples, where the blue histogram represents the distribution of the means. The red line is the value observed for the lenses, and the black-dashed line is the mean value of the Monte Carlo control distribution.

It is interesting to notice that the Poisson uncertainties ($\sigma_{lens} = 0.157, \sigma_{control} = 0.015$) of the mean number of companions are smaller, by a approximately a factor two, than the empirical standard errors. The scatter in the number of companions is not fully described by the Poisson noise, but includes additional variance related to the clustering of galaxies. Therefore, the empirical standard error of the mean represents a more conservative estimate of the uncertainty.

5.6 Companion galaxies as a function of absolute magnitude and redshift

Starting from the companion catalogs, built for the lens and control samples, it is possible to evaluate the behaviour of companion galaxies as a function of absolute magnitude and redshift. Therefore, the lens sample has been divided into 4 bins, figure 5.16, according to specific intervals in absolute magnitude and redshift.

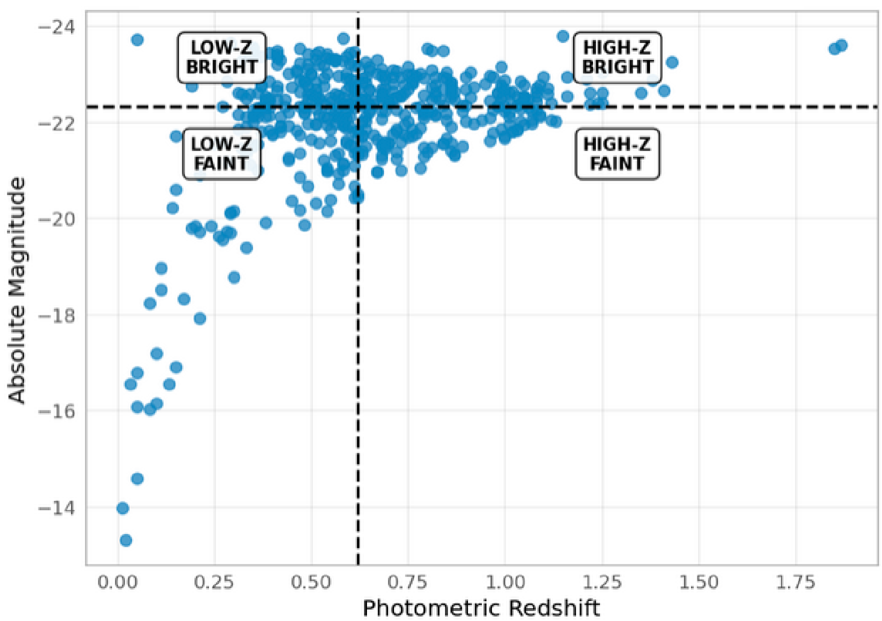

Figure 5.16: Lens sample represented in the absolute magnitude-redshift plane, with the dashed lines defining the 4 bins.

The definition of these bins is related to the lens sample and its median values: $M_{median} = -22.336$ and $z_{median} = 0.620$. The 4 bins, considering the actual occupancy intervals of the lenses, are limited by the following ranges:

- low-z and bright defined by objects with $0.050 \leq z < 0.610$ and $-23.732 \leq M < -22.336$;
- low-z and faint defined by objects with $0.010 \leq z < 0.620$ and $-22.336 \leq M < -13.313$;
- high-z and bright defined by objects with $0.620 \leq z < 1.870$ and $-23.780 \leq M < -22.336$;
- high-z and faint defined by objects with $0.620 \leq z \leq 1.130$ and $-22.336 \leq M \leq -20.432$

These cuts are then applied to the control sample with the purpose of studying, as a function of absolute magnitude and redshift, companion galaxies surrounding lenses and non-lens galaxies. By performing an environmental analysis we get the results reported in table 5.8 and represented in figure 5.17.

	Lenses		**Control galaxies**	
	Objects	**Companions**	**Objects**	**Companions**
low-z and bright	109	11.422 ±0.564	9726	9.766 ±0.063
low-z and faint	144	11.694 ±0.501	13551	9.728 ±0.053
high-z and bright	138	11.848 ±0.510	11555	9.749 ±0.058
high-z and faint	102	11.637 ±0.591	10821	9.766 ±0.060

Table 5.8: Results of the binning, in absolute magnitude and redshift, of the lens and control samples. The errors are computed as the standard deviation of the sample divided by the square root of the sample size.

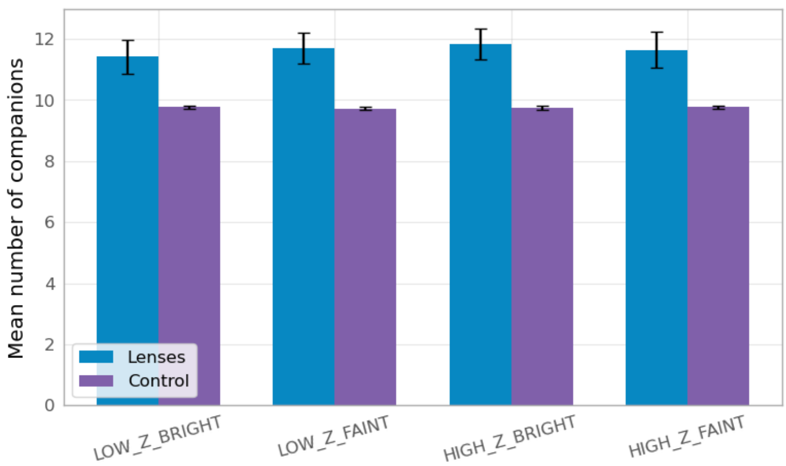

Figure 5.17: Graphical visualisation of the mean number of companions for lenses and control galaxies, in each of the four bins previously defined

It is interesting to study the radial profile, in physical units, of the surface density for each bin. The bins are not directly comparable in terms of absolute surface density, since bins with different redshift ranges correspond to different cosmic epochs. Nevertheless, the cumulative surface density profiles, figure 5.18, indicates that the different bins present similar radial behaviours.

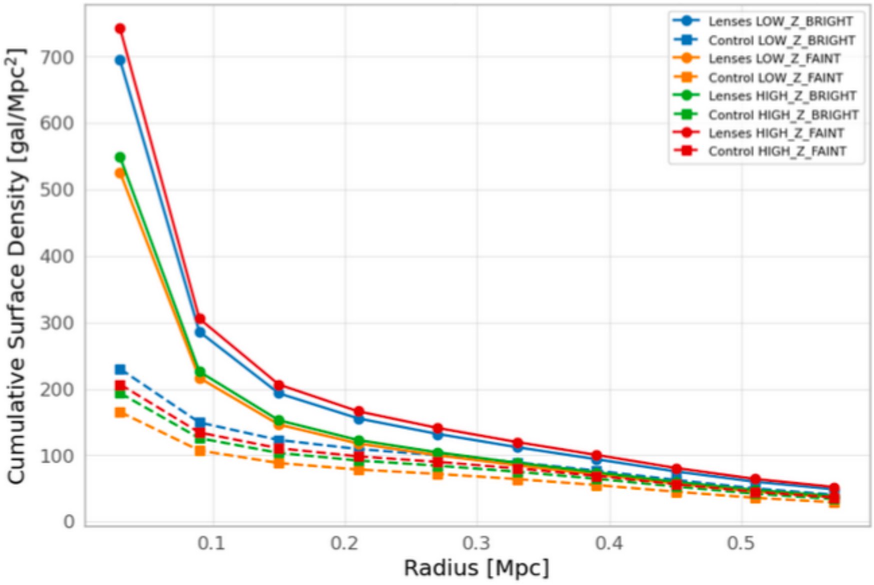

Figure 5.18: Cumulative radial profile, expressed in Mpc, of the surface density of galaxies surrounding lenses and non-lens galaxies. The data points are plotted at the center of each radial bin and each color refers to a different (M, z) bin. The error bars are computed by propagating the Poisson uncertainty $\sigma_{\Sigma(<R)} = \sigma_{N(<R)}/\pi R^2$.

Similarly, from the surface density analysed annulus by annulus, figure 5.19, we notice that the separation between lenses and control galaxies decreases rapidly with the radius: already in the second annulus (0.06-0.12 Mpc) the separation becomes much smaller, but remains significant. This plot highlights that different bins present similar radial behaviours and confirms that the excess of companion galaxies is located within the innermost region around the lenses. In particular, the NFW scale size for an halo with $M_{halo} = 10^{12} M_{\odot}$ is about 25 kpc and 70 kpc with $M_{halo} = 10^{13} M_{\odot}$, as reported in [Dutton and Macciò (2014)]. This is consistent with the excess of companions being located within the dark matter halo of the lens galaxies and not in some larger scale structure.

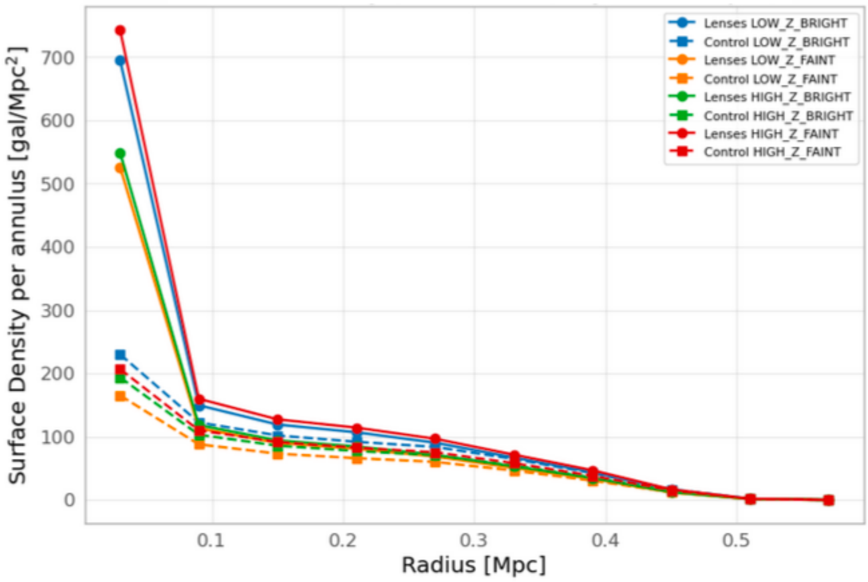

Figure 5.19: Radial profile per annulus, expressed in Mpc, of the surface density of galaxies surrounding the lenses and the non-lens galaxies. The data points are plotted at the center of each radial bin and each color refers to a different (M, z) bin. The error bars are computed by propagating the Poisson uncertainty $\sigma_{\Sigma(R_1<r<R_2)} = \sigma_{N(R_1<r<R_2)}/\pi(R_2 - R_1)^2$.

Now, we want to quantify the relative variation V of companions, between lenses and control galaxies, for each bin. The results of this analysis, reported in table 5.9 and represented in figure 5.20, highlight a slightly larger variation in the low z-faint and high-z bright bins; however this difference is not particularly significant.

Bin	Variation	Error
low-z and bright	0.170	0.058
low-z and faint	0.202	0.052
high-z and bright	0.215	0.053
high-z and faint	0.192	0.061

Table 5.9: Variations in the mean number of companions between lenses and control galaxies. The values are referring to 4 bins defined in the absolute magnitude-redshift plane. The variations are computed using the formula (5.9), while the associated errors are derived applying the standard error propagation.

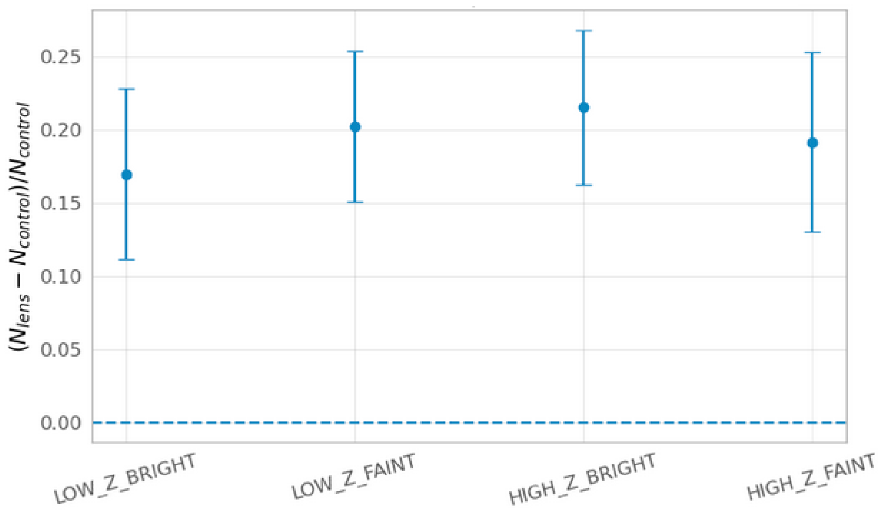

Figure 5.20: Graphical visualisation of the variations, reported in table 5.9, in the mean number of companions between lenses and control galaxies. The values are referring to 4 bins defined in the absolute magnitude-redshift plane. The error bars are derived applying the standard error propagation to the formula (5.9).

The fractional excess is approximately the same in all bins and therefore does not depend on absolute magnitude and redshift.

5.7 Halo mass ratio

The number of companions, surrounding lenses and non-lens galaxies, can be used to study the haloes in which galaxies are located. In fact, the Q1 dataset provides an opportunity to explore the galaxy-halo connection thanks to: high-resolution space-based imaging, multi-band photometry and a large galaxy number density. In this regard, the halo occupation distribution (HOD) framework is useful to describe how galaxies populate dark-matter halos as a function of the halo mass. Galaxy clustering is observable and represents a powerful tool to study the properties of dark-matter haloes. In particular, [Kang et al.(2026)] studied the galaxy-halo connection at $z < 1$, considering its dependence on colour and morphology, using the five-parameter HOD model of [Zheng et al.(2005)]. In this model, a halo of mass M is populated by a mean number of galaxies equal to

$$\langle N_{gal}(M)\rangle = \langle N_{cen}(M)\rangle + \langle N_{sat}(M)\rangle \tag{5.16}$$

where $\langle N_{cen}(M)$ and $\langle N_{sat}(M)\rangle$ represent the mean number of central and satellite galaxies. Considering the companion catalogs, we can treat lenses and control galaxies as central galaxy candidates, and study their companions as satellite galaxies. Therefore, the satellite occupation function, described as a power law with a low-mass cutoff, can be used within the HOD framework to obtain an estimate of the halo mass ratio between lenses and control galaxies.

The satellite galaxy occupation function is expressed as

$$\langle N_{sat}(M)\rangle = \left(\frac{M - M_0}{M_1}\right)^{\alpha} \text{ with } M > M_0 \tag{5.17}$$

where M_0 is the mass below which haloes do not host satellites, M_1 is a normalisation term and α is the power-law slope. To estimate these parameters we consider the results of the HOD fitting reported in [Kang et al.(2026)], where the values are referring to several redshift intervals. We consider the average redshift of lenses and control galaxies to estimate, through linear interpolation, the values of the parameters: $\log_{10}(\frac{M_0}{M_\odot}) = 9.9$, $\log_{10}(\frac{M_1}{M_\odot}) = 13.2$ and $\alpha = 1.1$.

Finally, we compute the halo mass ratio between lenses and non-lens galaxies by inverting equation (5.15) with the halo as a function of the mean number of satellite galaxies

$$\frac{M_{h,lens}}{M_{h,control}} = \frac{M_0 + M_1 N_{sat,lens}^{1/\alpha}}{M_0 + M_1 N_{sat,control}^{1/\alpha}} = 1.23 \tag{5.18}$$

The halo mass ratio is bigger than 1 suggesting that lenses lie in more massive haloes; in particular in haloes that are 23% more massive with respect to non-lens galaxies. To associate an uncertainty to this ratio, we use a Monte Carlo resampling procedure ($N = 50\ 000$), assuming Gaussian uncertainties on the measured mean number of companions for both lens and control galaxies. By repeating the computation of the halo-mass ratio, we obtain an empirical distribution of the ratio. Moreover, we use the median of this distribution as our central value and derive a 95% confidence interval [1.167, 1.287]; since this interval lies entirely above unity, we find evidence that lens galaxies reside in more massive dark matter haloes than the control sample. This analysis assumes that the parameters of the satellite galaxy occupation are fixed; therefore, the uncertainty arises only from the mean number of companions.

Chapter 6

Conclusions

6.1 Current limitations

The results of this thesis are based on a very large sample of lenses, substantially larger than those considered in previous studies; however, they are constrained by several limiting factors.

In fact, the redshift values of Q1 are photometric redshifts and, therefore, present several disadvantages, as described in [Euclid Collaboration(2026)]. Since the observed photometry can be contaminated by multiple objects at different redshifts. Moreover, there is the contamination from lensed source light, known as lens-source blending, and from crowded environments. This situation highlights that reliability depends on the surface brightness ratio between the lens and the source. This limitation is expected to be mitigated with the DR1 release, which will include spectroscopic redshift measurements. These will provide more accurate redshift estimates.

Another problem is represented by the absence of velocity dispersion measurements, since galaxies with the same absolute magnitude can have different velocity dispersions. Furthermore, in the work of [Treu et al.(2009)] the environment distribution for lens galaxies and galaxies, matched by velocity dispersion and redshift, is similar. Therefore, considering also velocity dispersion of lenses and control galaxies could lead to a more complete description of the situation.

These limitations need to be interpreted considering that the Q1 dataset has been released for showing, to the astronomical community, the potential of the Euclid mission. The subsequent data releases, starting with DR1, will enable more precise analyses and provide access to a significantly larger amount of information.

6.2 Summary of the main results

In this work we carried out a comparative study of companion galaxies around strong galaxy-galaxy lenses and non-lens galaxies. The main conclusions are presented below.

- The analysis of companions along the line-of-sights shows no significant difference between the two samples; with LOS galaxies exhibiting statistically similar distributions. This initial test was conducted to quantify possible over- and underdensities along lenses LOS.

- The local environmental comparison reveals that lens galaxies exhibit an excess of approximately 25% in the average number of companions with respect to control galaxies, which were selected to have the same distributions in absolute magnitude and redshift. The following KS test of companion galaxy distributions supports this result.

- Additionally, companion galaxies have been evaluated as a function of absolute magnitude and redshift; with the observed excess of companions not significantly changing between different bins.

- Finally, this excess of companions has been translated, using the HOD framework, into a mass ratio between the dark matter haloes of lenses and non-lens galaxies. In particular, haloes hosting lenses are 23% more massive than haloes hosting non-lens galaxies.

Therefore, lenses lie in richer environments than non-lens galaxies, with the same distribution in absolute magnitude and redshift, and they are characterised by more massive haloes.

Bibliography

[Schneider & Kochanek & Wambsganss (2006)] Schneider, P., Kochanek, C., Wambsganss, J., *Gravitational Lensing: Strong, Weak and Micro*, Springer, 2006, Berlin.

[Meneghetti (2021)] M. Meneghetti, *Introduction to Gravitational Lensing — with Python Examples*, Springer-Verlag, 2021.

[Fox (2015)] S. Fox, *Hubble's Double Take* [WWW Document], NASA, 2015. Available at: http://www.nasa.gov/content/hubbles-double-take

[Bolton (2005)] A. Bolton, *Einstein Ring Gravitational Lens (SDSS J162746.44-005357.5)*, NASA, ESA, A. Bolton (Harvard–Smithsonian CfA) and the SLACS Team, 2005. [WWW Document]. Available at: https://hubblesite.org/contents/media/images/2005/32/1796-Image

[Congdon & Keeton (2018)] A. B. Congdon and C. R. Keeton, *Principles of Gravitational Lensing: Light Deflection as a Probe of Astrophysics and Cosmology*, Springer Praxis Books (Astronomy and Planetary Sciences), Springer Nature Switzerland AG, Cham, 2018.

[Dyson et al. (1920)] Dyson, F. W., Eddington, A. S., & Davidson, C. (1920). *A determination of the deflection of light by the sun's gravitational field, from observations made at the total eclipse of May 29, 1919*. Philosophical Transactions of the Royal Society of London Series A, **220**, 291–333.

[Dodelson (2017)] Dodelson, S. (2017). *Gravitational Lensing*. Cambridge: Cambridge University Press.

[Hurt & The GraL Collaboration (2021)] R. Hurt and The GraL Collaboration, *Quadruply-imaged quasar diagram*, ESA/Gaia, 07 April 2021. Copyright: R. Hurt (IPAC/Caltech)/The GraL Collaboration.

[Euclid (2019)] *Effects of lensing mass on an image*, Euclid Mission. Image credit: NASA, ESA, and Johan Richard (Caltech, USA), September 1 2019.

[Euclid Consortium (2023)] Euclid Consortium, *A space mission to map the Dark Universe*, The Euclid Blog, Mapping the dark Universe with gravitational weak lensing, Francesca Lepori, 6 October 2023. Available online: https://www.euclid-ec.org/blog/mapping-the-dark-universe-with-gravitational-weak-lensing

[Kochanek et al.] C. S. Kochanek, E. E. Falco, C. Impey, J. Lehár, B. McLeod, and H.-W. Rix, *CASTLES Survey: CfA-Arizona Space Telescope LEns Survey of gravitational lenses*, website. Available at: https://www.cfa.harvard.edu/castles/

[Bolton et al. (2006)] Bolton, A. S., Burles, S., Koopmans, L. V. E., Treu, T., & Moustakas, L. A. (2006). *The Sloan Lens ACS Survey. I. A large spectroscopically selected sample of massive early-type lens galaxies.* Astrophysical Journal, 638(2), 703–724. doi:10.1086/498884.

[Lemon et al. (2024)] C. Lemon, F. Courbin, A. More, P. Schechter, R. Cañameras, L. Delchambre, C. Leung, Y. Shu, C. Spiniello, Y. Hezaveh, J. Klüter, and R. McMahon, *Searching for Strong Gravitational Lenses* Space Science Reviews, vol. 220, art. 23, 2024. doi:10.1007/s11214-024-01042-9.

[Zooniverse (2026)] Zooniverse, *Hubble Sequence (Image: 1015_fork-1920)*, ESO Supernova Planetarium & Visitor Centre Exhibition Images, European Southern Observatory (ESO) & Heidelberg Institute for Theoretical Studies (HITS), Garching bei München, Germany, 2026. Available online: https://supernova.eso.org/exhibition/images/1015_fork-1920/.

[Shajib et al. (2024)] A. J. Shajib, G. Vernardos, T. E. Collett, V. Motta, D. Sluse, L. L. R. Williams, P. Saha, S. Birrer, C. Spiniello, e T. Treu, "Strong Lensing by Galaxies," *Space Science Reviews*, vol. 220, art. 87, 2024. doi: 10.1007/s11214-024-01105-x.

[Arbey & Mahmoudi (2021)] A. Arbey and F. Mahmoudi, *Dark matter and the early Universe: a review*, arXiv:2104.11488 [hep-ph] (2021).

[Green (2022)] A. M. Green, *Dark matter in astrophysics/cosmology*, Part of the Dark Matter Session 118 of the Les Houches School (2021), SciPost Phys. Lect. Notes **37** (2022), doi:10.21468/SciPostPhysLectNotes.37.

[Nipoti & Fraternali & Cimatti (2019)] C. Nipoti, F. Fraternali and A. Cimatti, *Introduction to Galaxy Formation and Evolution: From Primordial Gas to Present-Day Galaxies*, Cambridge University Press (2019), ISBN: 9781107134768.

[Wechsler & Tinker (2018)] R. H. Wechsler and J. L. Tinker, “The Connection between Galaxies and their Dark Matter Halos,” *Annual Review of Astronomy and Astrophysics*, vol. 56, pp. 435–487, 2018. doi:10.1146/annurev-astro-081817-051756. arXiv:1804.03097 [astro-ph.GA].

[Rodriguez-Puebla (2024)] A. Rodriguez-Puebla, “The Co-Evolution Between Galaxies and Dark Matter Halos,” arXiv:2404.10801 [astro-ph.GA], 2024. To appear in *Revista Mexicana de Astronomía y Astrofísica (Serie de Conferencias)*, Proceedings of XVII RRLA-LARIM (2023).

[Zheng et al. (2009)] Z. Zheng, I. Zehavi, D. J. Eisenstein, D. H. Weinberg, and Y. P. Jing, “Halo Occupation Distribution Modeling of Clustering of Luminous Red Galaxies,” *The Astrophysical Journal*, vol. 707, no. 1, pp. 554–572, 2009. doi:10.1088/0004-637X/707/1/554

[Peacock & Smith (2000)] J. A. Peacock and R. E. Smith, “Halo occupation numbers and galaxy bias,” Mon. Not. R. Astron. Soc. **318**, 1144–1156 (2000).

[Zheng et al. (2007)] Z. Zheng, A. L. Coil, and I. Zehavi, “Galaxy Evolution from Halo Occupation Distribution Modeling of DEEP2 and SDSS Galaxy Clustering,” *The Astrophysical Journal*, vol. 667, pp. 760–779, Oct. 2007.

[Euclid Collaboration et al.(2025)] Euclid Collaboration, Bergamini P., Meneghetti M., Acebron A., et al., 2025, “Euclid Quick Data Release (Q1): The first catalogue of strong-lensing galaxy clusters”, *Astronomy & Astrophysics*, submitted, ESO manuscript, 20 March 2025.

[Euclid Collaboration (2025)] Euclid Collaboration, Walmsley M., Holloway P., Lines N. E. P., et al., 2025, “Euclid Quick Data Release (Q1): The Strong Lensing Discovery Engine A – System overview and lens catalogue”, *Astronomy & Astrophysics*, submitted, arXiv:2503.15324.

[Walmsley et al. (2025)] M. Walmsley, P. Holloway, N. Lines, K. Rojas, T. Collett, A. Verma, T. Li, J. Nightingale, G. Despali, S. Schuldt, and the Euclid Consortium, *Euclid Quick Data Release (Q1): The Strong Lensing Discovery Engine*, Dataset, Version 0.0.3, Zenodo (19 March 2025). https://doi.org/10.5281/zenodo.15025832

[Euclid Collaboration (2025)] Euclid Collaboration, H. Aussel, I. Tereno, M. Schirmer, et al., *Euclid Quick Data Release (Q1): Data Release Overview*, Astronomy & Astrophysics, submitted (2025). arXiv:2503.15302 [astro-ph.GA]. https://arxiv.org/abs/2503.15302

[Troja et al. (2022)] A. Troja, I. Tutusaus, J. G. Sorce, and the Euclid Consortium, *Euclid in a nutshell*, Proceedings of Science (PoS), ICHEP2022, 094 (2022). https://pos.sissa.it/

[Euclid Collaboration (2025)] Euclid Collaboration, M. Tucci, S. Paltani, W. G. Hartley, et al., *Euclid Quick Data Release (Q1): Photometric redshifts and physical properties of galaxies through the PHZ processing function*, Astronomy & Astrophysics, submitted (2025). arXiv:2503.15306 [astro-ph.GA]. https://arxiv.org/abs/2503.15306

[ESA Datalabs] European Space Agency (ESA), *ESA Datalabs: A Platform for Space Data Analysis*, available at: https://datalabs.esa.int/

[Wong et al. (2018)] Wong, K. C., Sonnenfeld, A., Chan, J. H. H., Rusu, C. E., Tanaka, M., Jaelani, A. T., Lee, C.-H., More, A., Oguri, M., Suyu, S. H., & Komiyama, Y. (2018). *Survey of Gravitationally Lensed Objects in HSC Imaging (SuGOHI). II. Environments and Line-of-Sight Structure of Strong Gravitational Lens Galaxies to* $z \sim 0.8$. The Astrophysical Journal, 867, 107. https://doi.org/10.3847/1538-4357/aae381

[Metcalf (2026)] R. Benton Metcalf, *Notes: Practical Statistics for Physics and Astronomy*, Alma Mater Studiorum – Università di Bologna, May 20, 2026.

[SciPy Community] SciPy Community, *scipy.stats.ks_2samp — SciPy v1.x Manual*, available at: https://docs.scipy.org/doc/scipy/reference/generated/scipy.stats.ks_2samp.html,

[Tonry et al. (2012)] Tonry, J. L., Stubbs, C. W., Lykke, K. R., Doherty, P., Shivvers, I. S., Burgett, W. S., Chambers, K. C., Hodapp, K. W., Kaiser, N., Kudritzki, R.-P., Magnier, E. A., Morgan, J. S., Price, P. A., & Wainscoat, R. J. 2012, "The Pan-STARRS1 Photometric System", *The Astrophysical Journal*, **750**, 99, doi:10.1088/0004-637X/750/2/99.

[Fassnacht et al.(2011)] Fassnacht, C. D., Koopmans, L. V. E., & Wong, K. C. 2011, "Galaxy number counts and implications for strong lensing", *Monthly Notices of the Royal Astronomical Society*, 410, 2167–2179, doi:10.1111/j.1365-2966.2010.17591.x

[Jaroszynski & Kostrzewa-Rutkowska(2014)] Jaroszynski M., Kostrzewa-Rutkowska Z., 2014, "The influence of the matter along the line of sight and in the lens environment on the strong gravitational lensing", *Monthly Notices of the Royal Astronomical Society*, 439, 2432–2441, doi:10.1093/mnras/stu096

[Wong et al.(2011)] Wong K. C., Keeton C. R., Williams K. A., Momcheva I. G., Zabludoff A. I., 2011, "The Effect of Environment on Shear in Strong Gravitational Lenses", *The Astrophysical Journal*, 726, 84, doi:10.1088/0004-637X/726/2/84

[Kang et al.(2026)] Euclid Collaboration: Y. Kang, W. G. Hartley, D. Piras, W. d'Assignies, S. Paltani, A. Viitanen, M. Magliocchetti, J. G. Sorce, M. Tucci, H. J. McCracken, *Euclid Quick Data Release (Q1). The galaxy–halo connection at* $z < 1$ *and its dependence on colour and morphology*, Astronomy & Astrophysics manuscript no. (2026), 7 May 2026.

[Zheng et al.(2005)] Zheng, Z., Berlind, A. A., Weinberg, D. H., Benson, A. J., Baugh, C. M., Cole, S., Davé, R., Frenk, C. S., Katz, N., & Lacey, C. G., *Theoretical Models of the Halo Occupation Distribution: Separating Central and Satellite Galaxies*, arXiv:astro-ph/0408564v2 (2005).

[Keeton & Zabludoff(2004)] Keeton, C. R., & Zabludoff, A. I. 2004, "The Importance of Lens Galaxy Environments," *The Astrophysical Journal*, **612**, 660–678.

[Euclid Collaboration(2026)] Nersesian, A., et al. (Euclid Collaboration) 2026, "Euclid Data Release 1 (DR1): Euclid Lens Identification Pipeline and Scientific Exploration (ECLIPSE) IV: Photometric Redshifts and Physical Properties," *Astronomy & Astrophysics*, manuscript submitted, June 10, 2026.

[Treu et al.(2009)] Treu, T., Gavazzi, R., Gorecki, A., Marshall, P. J., Koopmans, L. V. E., Bolton, A. S., Moustakas, L. A., & Burles, S. 2009, "The SLACS Survey. VIII. The Relation Between Environment and Internal Structure of Early-Type Galaxies," *The Astrophysical Journal*, **690**, 670–682.

[Dutton and Macciò (2014)] Dutton, A. A., & Macciò, A. V. (2014), "Cold dark matter haloes in the Planck era: evolution of structural parameters for Einasto and NFW profiles," *Monthly Notices of the Royal Astronomical Society*, **441**, 3359–3374. doi:10.1093/mnras/stu742.

This research makes use of ESA Datalabs (datalabs.esa.int), an initiative by ESA's Data Science and Archives Division in the Science and Operations Department, Directorate of Science.